REPORT DOCUMENTATION PAGE

Form Approved
OMB No. 0704-0188

The public reporting burden for this collection of information is estimated to average 1 hour per response, including the time for reviewing instructions, searching existing data sources, gathering and maintaining the data needed, and completing and reviewing the collection of information. Send comments regarding this burden estimate or any other aspect of this collection of information, including suggestions for reducing the burden, to the Department of Defense, Executive Services and Communications Directorate (0704-0188). Respondents should be aware that notwithstanding any other provision of law, no person shall be subject to any penalty for failing to comply with a collection of information if it does not display a currently valid OMB control number.
PLEASE DO NOT RETURN YOUR FORM TO THE ABOVE ORGANIZATION.

1. REPORT DATE *(DD-MM-YYYY)*	2. REPORT TYPE	3. DATES COVERED *(From - To)*
13-09-2012	Final Report	01 JUN 2008 - 30 NOV 2011

4. TITLE AND SUBTITLE

Active Control of Unsteady Gasdynamics for Shock Compression and Turbulence Generation

5a. CONTRACT NUMBER

FA9550-08-1-0333

5b. GRANT NUMBER

FA9550-08-1-0333

5c. PROGRAM ELEMENT NUMBER

61102F

6. AUTHOR(S)

Adonios Karpetis

5d. PROJECT NUMBER

5e. TASK NUMBER

5f. WORK UNIT NUMBER

7. PERFORMING ORGANIZATION NAME(S) AND ADDRESS(ES)

Aerospace Engineering
Texas A&M University
College Station, TX

8. PERFORMING ORGANIZATION REPORT NUMBER

9. SPONSORING/MONITORING AGENCY NAME(S) AND ADDRESS(ES)

Air Force Office of Scientific Research
875 N Randolph St
Ste 325, Rm 3112
Arlington, VA 22203

10. SPONSOR/MONITOR'S ACRONYM(S)

AFOSR

11. SPONSOR/MONITOR'S REPORT NUMBER(S)

AFRL-OSR-VA-TR-2012-1082

12. DISTRIBUTION/AVAILABILITY STATEMENT

Distribution A: Approved for Public Release. Unclassified, unrestricted.

13. SUPPLEMENTARY NOTES

14. ABSTRACT

An important research area in propulsion science today involves transient processes. Steady state combustion has long been studied and used in engines, but transient processes are now being examined to determine their abilities in propulsion systems. One of the main ideas for transient propulsion involve pulsed detonations, and are referred to as pulsed detonation engines (PDE). Although the theory behind their use is sound, the implementation can be quite dangerous due to the high pressures involved with their operation. A safer approach to creating the transient pressure waves may be found using pulsed supersonic flames. The present work will examine the creation of a pulsed supersonic flame through actuation of the incoming oxidizer.

15. SUBJECT TERMS

16. SECURITY CLASSIFICATION OF:			17. LIMITATION OF ABSTRACT	18. NUMBER OF PAGES	19a. NAME OF RESPONSIBLE PERSON
a. REPORT	b. ABSTRACT	c. THIS PAGE	U	99	Adonios Karpetis
U	U	U			19b. TELEPHONE NUMBER *(Include area code)* 979-458-4301

Reset

Standard Form 298 (Rev. 8/98)
Prescribed by ANSI Std. Z39.18

Final Performance Report

FA9550-08-1-0333

Active Control of Unsteady Gasdynamics for Shock Compression and Turbulence Generation

Principal Investigators:

Dr. Adonios Karpetis

Dr. Rodney Bowersox

Dr. Tamas Kalmar-Nagy

Dr. Helen Reed

Institution:

Aerospace Engineering

Texas A&M University

College Station, TX

1. INTRODUCTION

Propulsion science is always expanding into new areas of research. From new areas like electromagnetic propulsion, to the more common combustion based engines, every area is advancing. Supersonic combustion and propulsion are gathering momentum as researchers strive to go faster, higher, and farther, pushing the limits of our current knowledge of aerospace propulsion.

A more common method utilized in aerospace propulsion is the ramjet [1]. By travelling at supersonic speeds, a shock wave forms at the inlet which works to compress the incoming fluid. The increased pressures and temperatures obtained in post shock conditions help to prepare a flow for downstream combustion [2]. However, the main requirement for the ramjet, supersonic speed ($M \geq 1$), can also be the most difficult to obtain. Multiple stages are often required to achieve the supersonic condition, at which point the ram effect continues the acceleration into higher Mach number regimes, as made famous by the Pratt and Whitney J58 engine used on the SR-71 Blackbird [3].

There is a possible method for mitigating the use of multiple staged engines using one robust engine solution with transient pulsed pressure waves, as seen in Figure 1.1. The shock wave needed for combustion in a ramjet engine may be synthesized through pulsed pressure waves. The interaction of weak pressure waves applied at a nozzle inlet could potentially interact to form a strong shock within the duct. This strong shock can be formed at subsonic speeds, and would prepare a flow for combustion. This would greatly reduce the speeds needed to operate a ramjet engine ($M < 1$). Other major advantages to such an engine include safety, and the lack of moving parts which will drastically lower overall operating costs. The motivation behind the present work is to examine the possibility of using a pulsed supersonic flame as a generator of these weak pressure waves.

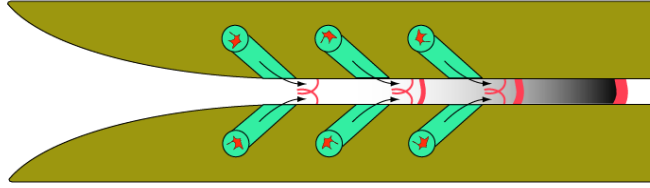This thesis follows the style of *Journal of Propulsion and Power*.

Fig. 1.1. Proposed solution for construction and operation of a low speed ramjet engine. Pulsed pressure waves interact and coalesce to form a normal shock within the duct, preparing a flow for combustion.

An important research area in propulsion science today involves transient processes. Steady state combustion has long been studied and used in engines, but transient processes are now being examined to determine their abilities in propulsion systems. One of the main ideas for transient propulsion involve pulsed detonations, and are referred to as pulsed detonation engines (PDE) [4, 5]. Although the theory behind their use is sound, the implementation can be quite dangerous due to the high pressures involved with their operation. Pulsed jets have also been studied, mainly for use in supersonic combustion ramjets (scramjets) [6–8]. These pulsed supersonic jets are typically used for flow control, or for fuel injection into scramjet engines. However, the principles used in the pulsed jets are generally related to detonation tubes.

A safer approach to creating the transient pressure waves may be found using pulsed supersonic flames. The present work will examine the creation of a pulsed supersonic flame through actuation of the incoming oxidizer. The pulsed actuation is achieved using an electromagnetic solenoid which controls the flow of air into the combustor. With correct timing the system will ignite, providing a high pressure, supersonic flame at the combustor exit. Other methods for pulsed air systems have been explored, but the electromagnetic solenoid was chosen for its cost and ease of implementation [9, 10].

The combustor used in the experiment is constructed using jet engine principles, and uses a flame holder to promote turbulence and stabilize a flame. The effects of flame holders has been well researched since the 1950s for use in jet engine configurations [11–13]. Additionally, a de Laval nozzle is used to accelerate the flame to supersonic speeds. Converging-diverging nozzles have also been well documented for use in rockets and jet engines [2, 14, 15].

Information on flames is often gathered optically. Two optical methods used in this experiment are an Intensified CCD (ICCD) and a schlieren system. Both of these methods have been used extensively for combustion research. The ICCD is often used in conjunction with laser based solutions for induced fluorescence, providing measurements of molecular constituents in the flame [16, 17]. However, the present work is more concerned with gathering photons created through chemiluminescence, the natural emission of light from a flame. Chemiluminescence has also been detected using ICCD systems, typically with different sets of filters applied to better resolve the concentrations of certain species in a flame [18, 19]. The present work focuses primarily on the qualitative aspects of the transient flame, although optical filters can be applied to the ICCD in the future. The schlieren setup is also used extensively in laboratories [20, 21]. A schlieren setup is appealing to combustion processes due to the ability of the system to detect density gradients produced by both high speed flows, and combusting gases [22, 23].

The flow pattern of a supersonic jet has been observed since the early 1900s, but is still important today. The structure of the supersonic jet can be an indication of the performance of a nozzle, but can also be observed to understand combustible areas within the flow [24]. The shockwave interactions for under and overexpanded jets are well defined in literature [2, 14].

This thesis is divided into sections. Section 2 details the experimental setup used to produce the transient supersonic flame, and the numerical model that mimics the experimental system. Included in this section is the description of gas regulation for

the experimental system, as well as the design of the combustor. Additionally, the computational model of the experimental system is described. Section 3 discusses the design and creation of the two optical systems used to image the transient supersonic flame. Section 4 concludes this thesis by presenting and discussing the results obtained both visually and computationally.

2. TRANSIENT SUPERSONIC FLAME APPARATUS AND SIMULATION

In what follows, the design, construction, and simulation of the transient supersonic flame apparatus is discussed. The combustion chamber was based on previous work in creating miniaturized combustors for afterburner flames [25]. The present system is a transient extension of the existing steady state device. The transient nature was discovered when unburnt flow through the nozzle was blocked using a thin walled obstruction [26]. The stagnation would allow a flammable mixture to form, creating a transient flame which would burst through the obstruction. The new device is operated transiently through the use of an electromagnetic solenoid valve. The valve actuation is designed to mimic the blocking effect of the obstruction. Chemilluminescence is desired because it is natural light emitted from the flame, allowing for observation without laser assistance. In terms of light emitted, supersonic flames are not very robust. Transient flames compound this problem, due to the small timescales in the experiment. The apparatus is simulated using Cantera, an open source software package, providing detailed chemistry and thermodynamic information. The program will be used to understand the behavior of thermochemistry within the combustion chamber throughout the transient event.

2.1 Supersonic Flame Apparatus

Due to the high pressures and temperatures that occur within the combustion chamber, materials that were able to withstand flame conditions were required. For this reason, brass and stainless steel components were used. These components were selected for their ease of use, availabilty, and machineability. The thermal coefficients of expansion between the two materials are similar, mitigating any problems inherent in heating dissimilar metals. In addition, high temperature thread locking material is applied to prevent any gas leaks during the combustion process.

The combustion chamber features three distinct sections. The outer chamber, the flame tube, and the nozzle, as shown in Figure 2.1. Methane is injected directly into the central flame tube. The tube contains a bluff body stabilizer (flame holder) combined with a spark plug in the recirculation region to initiate combustion [27]. The 90° vee-shaped bluff body occupies approximately half the area in the flame tube and is placed directly at the center of the flow. Assuming a maximum velocity of 10 m/s through the flame tube, and for an incompressible flow, the bluff body obstruction woud create a pressure drop of less than 100 Pa. Therefore, the pressure drop across the blockage is neglected due to the low velocities within the combustion chamber. The recirculation region can be estimated as a wedge-shaped body, with a characterized length as a parameter of bluff body height and flow velocity [13]. This region will be discussed in Section 4.2.

The initial construction of the combustor was based on designs for vitiated-air jet engines. Air is injected into the outer chamber via a solenoid valve, and is allowed to
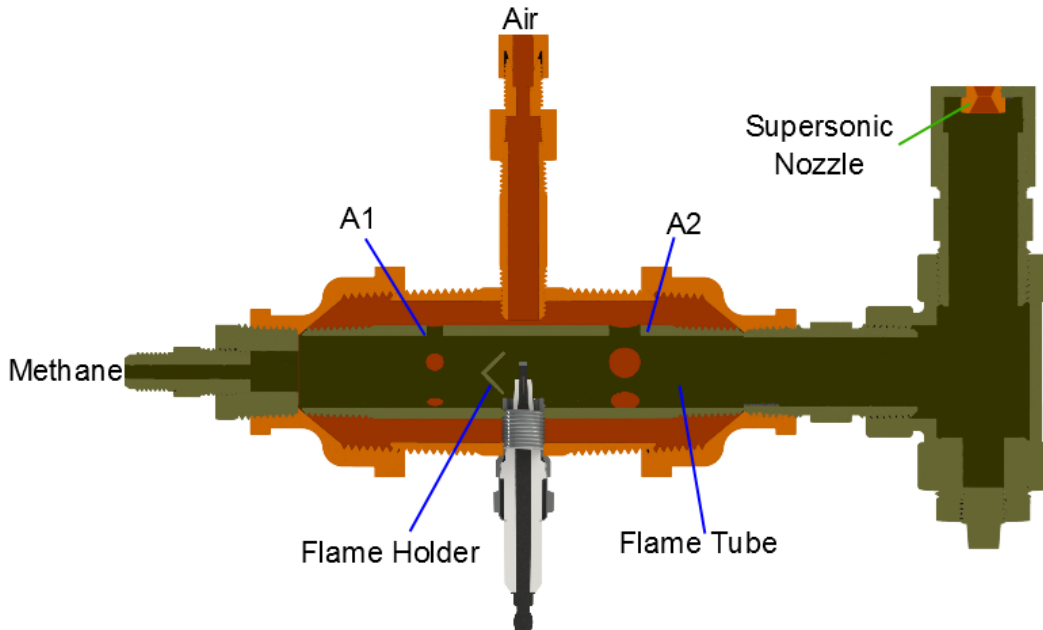

Fig. 2.1. Section view of computer generated combustor assembly.

mix with the methane through two entry areas (A1 and A2). The electromagnetic solenoid has an opening/closing time in the order of 25 ms. This relatively fast actuation will provide the appropriate air transient for combustion. The primary and secondary regions are a circular pattern of holes, with a secondary/primary area ratio of 3.3, as seen in Figure 2.1. Although the air inlets were initially designed to mimic air inlets on a jet engine, the actual operation is much different, and will be discussed in later sections.

Mass flow rates are metered by choked orifice plates at the methane and air supply tanks. The combination of orifices would result in a steady state equivalence ratio of $\phi = 1.4$, less than the upper flammability limit of 1.7 for methane [28]. However, the transient nature of the system yields an equivalence ratio that is continually changing throughout the actuation process. As the solenoid begins to open ($t \simeq 0$ ms), the area restriction at the solenoid produces a choked flow. As time progresses ($t > 0$ ms), pressure will build within the chamber, allowing for mixing of reactant gases. At this point, the air recirculates within the volume created by the flame holder, mixing with the methane and allowing combustion to occur.

After ignition, the products of combustion are then accelerated downstream through a de Laval nozzle. The de Laval nozzle expands the flow past $M = 1$, producing supersonic flow at the nozzle exit. The throat diameter is the smallest area in the combustion chamber to ensure choking after the air and fuel have been mixed. After undergoing a slight area expansion, the reacting gases are exhausted to the atmosphere. The ratio of exit area to throat area (ϵ expansion ratio in rocket science) is 1.25. Using the following 1-D isentropic expansion equation, the Mach number at the exit can be found.

$$(\frac{A_{exit}}{A_{throat}})^2 = \frac{1}{M^2}[\frac{2}{\gamma+1}(1 + \frac{\gamma-1}{2}M^2)]^{\frac{\gamma+1}{\gamma-1}} \qquad (2.1)$$

where M is Mach number, A_{exit} and A_{throat} are the exit areas and nozzle throat areas, and γ is the ratio of specific heats for the fluid [2]. The resulting Mach number at the nozzle exit is $M = 1.6$.

The nozzle is constructed from superfine isomolded graphite. The properties of graphite make it ideal for use in rocket nozzles [14]. Graphite experiences minimal shape change when heated, making it optimall for use in the transient combustion environment where the nozzle is constantly being quickly heated/cooled. Additionally, this property ensures that heat based fracturing will not occur, mitigating the constant replacement of nozzles. Temperatures required for the ablation and sublimation of graphite are in excess of 3800 K [29]. This is much higher than the temperatures reached within the combustion chamber, as will be shown in later sections. The temperature never exceeds 2700 K, and that is observed only during short durations throughout the transient burn. The small timescales of the transient flame mitigate the effects of erosive burning on the nozzle area ratio (Equation 2.1). Therefore, erosive burning of the nozzle surface is neglected due to the transient nature of the experiment.

The spark plug used to ignite the system is driven by an ignition coil which is charged by a 13.8V 15 Amp power supply. The key element to creating a high voltage spark is the rapid change of current through the ignition coil. This is achieved using a 2N3055 NPN transistor. Unlike a mechanical relay, the transistor allows for fast changes in current flow, creating voltages in the ignition coil upwards of 15 kV, ensuring a very energetic spark.

The various timescales of the experiment require accurate time coordination. The system timing can be controlled using two different methods, a) through the use of an in-house built timing circuit, or b) by using a Berkeley Nucleonics 565 pulse generator. The first method requires a set of circuits designed around the LM555 timer integrated circuit (IC) operating in cascading monostable mode. The second method uses a pulse generator which has an array of individually controlled channels
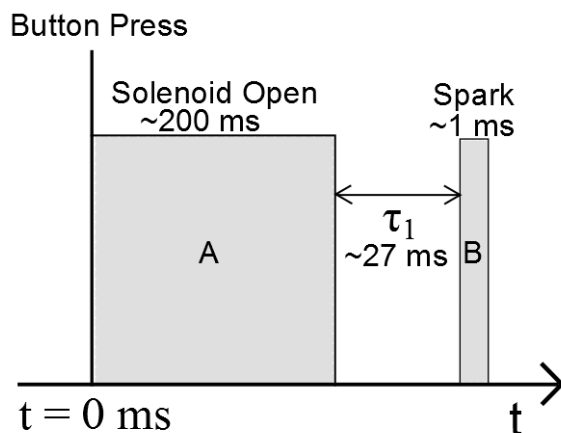
Fig. 2.2. Relative timescales used in the experiment. (A) represents the open solenoid time ($\sim$200 ms), and (B) is the ignition spark ($\sim$1 ms). The experiment is initiated by a button press. The delay (τ_1) determines the ignition point, and is required for allowing the reactants to mix before combustion.

through which 5 V Transistor-Transistor-Logic (TTL) signals can be generated. The goal is to control the timescales used in the experiment. The timing revolves around a master signal, in this case the solenoid valve. The length of the master signal indicates the amount of time the solenoid is open for, as seen in Figure 2.2. A second pulse is used to trigger the ignition spark. The delay time between the solenoid closing and the spark must also be tuned to ensure combustion occurs, as will be discussed in Section 4.1. A third trigger is needed for the image intensifier and is described in Section 3.1.

The methane and air flows are provided by regulated tanks far upstream of the combustor. Orifice plates are used to control the mass flow rates of the methane and air just downstream of the pressure regulators. The orifices ensure a flammable mixture during the ignition process. Total pressure at the regulator can be varied between 60–120 psig for the experiment. These bounds are predetermined by experimental conditions; the solenoid valve cannot withstand upstream tank pressures

above 120 psig, and the combustor nozzle will not choke at a tank pressure below 60 psig, according to the result described in Equation 2.3.

By monitoring the pressure upstream and downstream of the orifices, the appropriate flow regime can be determined as either sonic or subsonic. The flow rates differ greatly depending on the flow regime. The sonic mass flow rates through the orifice are calculated using the 1-D isentropic compressible flow equation:

$$\dot{m} = \frac{AP_t}{\sqrt{T_t}}\sqrt{\frac{\gamma}{R}}\left(\frac{\gamma+1}{2}\right)^{-\frac{\gamma+1}{2(\gamma-1)}} \tag{2.2}$$

where A is the area of the orifice, p_t is the total pressure upstream of the orifice, T_t is the total pressure, γ is the ratio of specific heats, and R is the specific gas constant [14]. A flow is choked when the Mach number of a system reaches unity. In the absence of heat transer and friction, this point will almost always occur at the minimum area of the system. The flow will become choked when the pressure located at the minimum area (throat pressure) reaches a critical value dictated by isentropic relations. The critical pressure required for choked flow is described by the following 1-D isentropic relation:

$$\frac{P^*}{P_t} = \left(\frac{2}{\gamma+1}\right)^{\left(\frac{\gamma}{\gamma-1}\right)} \tag{2.3}$$

which for air at $\gamma = 1.4$, is 0.528 [30]. If the throat pressure reaches the critical pressure, P^*, choked flow at the metering orifice can be assumed [2]. In the case of the methane, air, and solenoid orifices, the throat pressure while subsonic can be assumed to be the same as the downstream pressure, simplifying the equation.

The overall reacting gas delivery system is depicted in Figure 2.3. It is important to note that when pressurized, the solenoid valve will act as an orifice. Therefore, the pressure distributions throughout the system become increasingly complex with actuation of the solenoid valve. The presence of the solenoid valve in the air supply line does not ensure that the upstream orifice is choked. In the air supply line, the
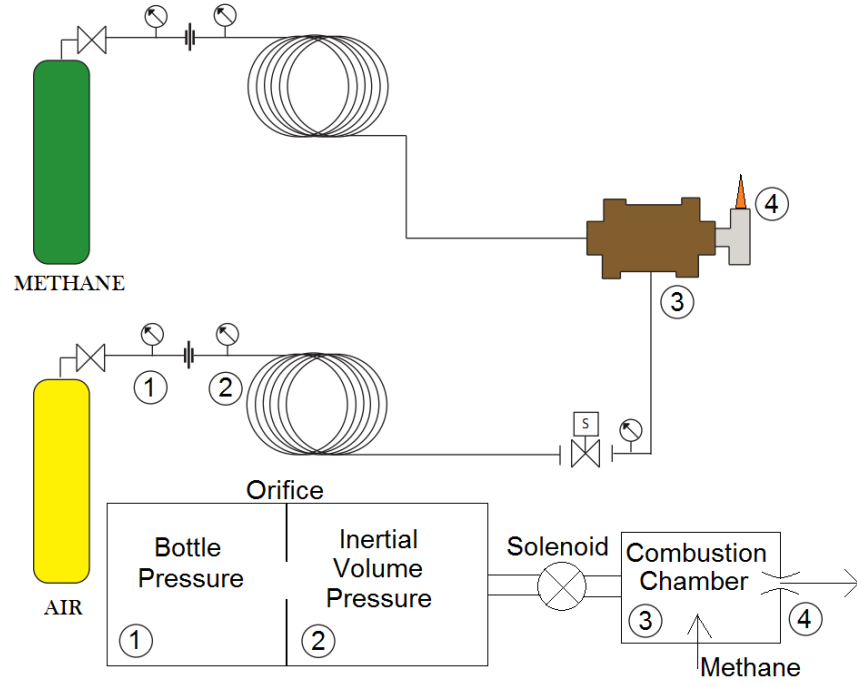
Fig. 2.3. Diagram of reacting gas delivery system and depiction of general volumes encountered in the air supply line.

flow can only choke at one area in steady state configurations, either the orifice or the solenoid. The choke point will vary in time as the system pressures and the area of the solenoid in the air line change. As the pressure builds in the air supply line the orifice will cease choking. When flow through an orifice is subsonic, a mass flow rate can be described using an inviscid approach.

$$P_1 - P_2 = \frac{1}{2}\rho V^2 \tag{2.4}$$

where P_1 and P_2 correspond to upstream and downstream pressure, V is the velocity, and ρ is the density. Because the flow is subsonic, it can be assumed the the flow is
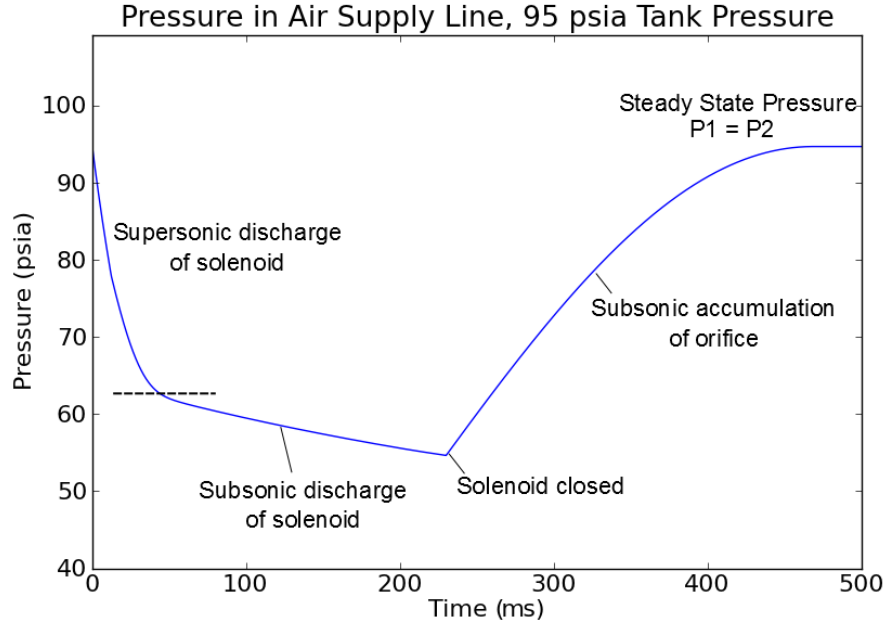
Fig. 2.4. Graph representing an example of pressure within the inertial volume during solenoid actuation. Note the separate regions of subsonic/supersonic flow.

incompressible. Therefore, density in this case can be considered constant. Solving for velocity, the mass flow rate can be found using the definition of mass flow rate:

$$\dot{m} = \rho V A = \sqrt{2\rho(P_1 - P_2)}A \qquad (2.5)$$

where A is the area of the orifice.

The presence of a solenoid valve at the combustion chamber, which acts to quickly start and stop the supply of air, will cause the volume between the supply tank and solenoid valve to become pressurized. This pressurized system has an inertia that must be taken into account when simulating the combustion process, as it will greatly affect the combustion system pressure, as shown Figure 2.4.

Although there will be a temperature loss due to the expansion of gases through their respective orifices, the surface area of the supply lines will ensure that enough

heat transfer will occur to keep the gas at ambient temperatures. The exception to this is the mass flow rate through the nozzle, as the temperature of the combustion chamber can not be assumed ambient at all times. The thermodynamic properties of the combustor are calculated by the software package described in Section 2.2 to calculate the nozzle mass flow rate.

Figure 2.4 shows the pressure distribution within the inertial volume for one of the operating conditions of the experiment (corresponding to a tank pressure of 95 psia). The solenoid opens at time $t = 0$ s, causing the supersonic discharge of air due to the relatively large choked area of the solenoid. Because the combustion chamber has a nozzle with a small throat diameter, there will be an accumulation of pressure in the combustion chamber. As the pressure in the chamber rises the solenoid orifice will stop choking, causing subsonic discharge through the solenoid orifice. The lowered pressure in the inertial volume will cause the air orifice upstream of the solenoid to begin flowing, attempting to replenish the volume created in the air supply line. Due to the large area of the solenoid orifice, steady state conditions would result in choked flow through the air orifice, and subsonic flow through the solenoid. When the solenoid begins to close at approximately $t = 200$ ms, the inertial air supply volume will fill as it did before $t = 0$ ms, eventually reaching a steady state pressure corresponding to the back pressure of the system, as shown in Figure 2.4.

2.2   Combustor Simulation

The combustor is simulated as a zero-dimensional well-stirred reactor (WSR) using Cantera [31]. Cantera is a suite of object-oriented software tools used for chemically reacting flow problems involving chemical kinetics, thermodynamics, and transport processes [32]. The present work uses the Gas Research Institute Mechanism 3.0 (GRI-Mech 3.0), which is an optimized detailed kinetic mechanism based on experimental measurements designed to model methane-air combustion [33]. It utilizes 325 mostly reversible reactions and 53 gas species. This work is performed
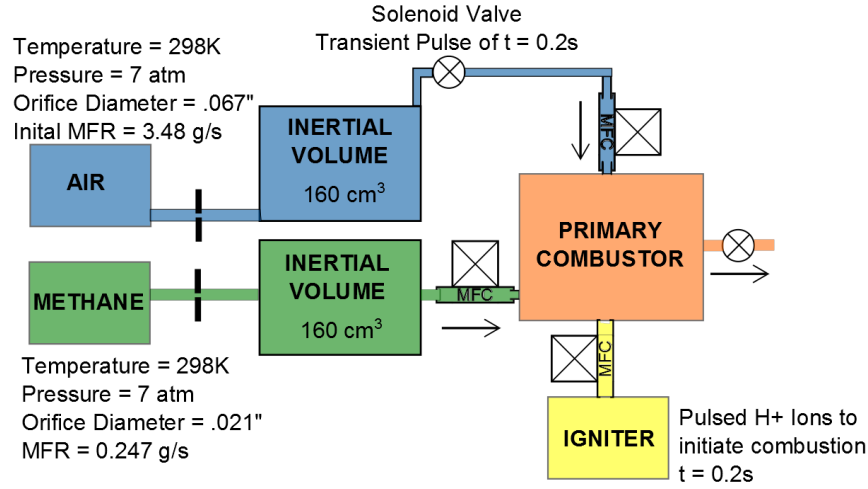
Fig. 2.5. Basic diagram of combustor simulation within Cantera.

using Python 2.6, an object oriented programming language with various scientific and mathematic library packages available [34]. Comparisons of simulated reactor based combustion experiments with Cantera have been performed, but the literature on the topic is scarce [35]. However, the code has been validated in certain geometries against experimental data [35]. The present study will use the results only in a qualitative sense, in order to explain the observations in the experiment. Therefore, questions of computational accuracy do not arise.

The zero dimensional model assumes that gases are instantaneously mixed, regardless of the vessel size or the pressure differences and velocities across the reactor. This introduces several discrepancies in the comparison of the experiment to the simulation. Assumptions must be made to ensure congruency between the physical device and the simulation. The volume of the combustor is estimated to be 120 cm^3. The overall system is modeled in Cantera as shown in Figure 2.5. The ignition event is mimicked by injecting hydrogen atoms into the flow. The extreme reactivity of these atoms initiates combustion. The hydrogen atoms have a profound effect on a transient system. The mass flow rate profile for hydrogen is in the shape of a Gaussian pulse, as a function of time. Due to the transient nature of the system, the
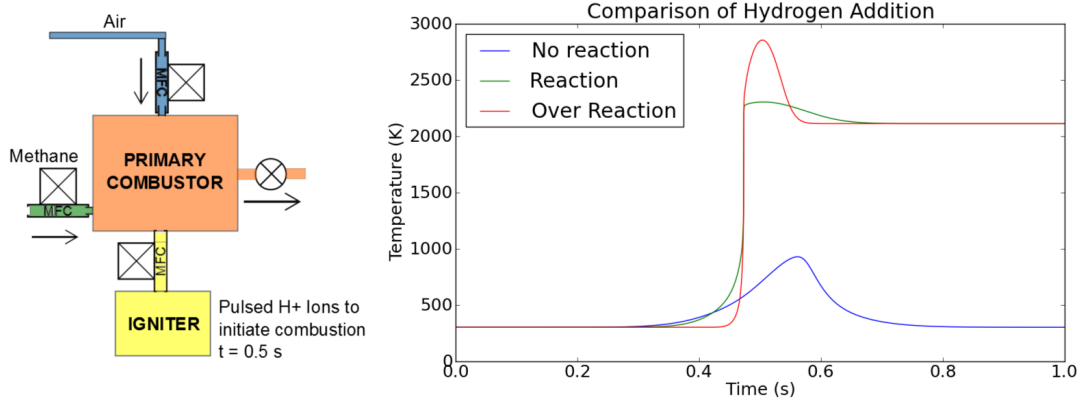
Fig. 2.6. Effect of hydrogen atom injection on a simulated steady state system. Case A) Not enough hydrogen atoms added, no reaction occurs. Case C) Too many hydrogen atoms are added, resulting in an inaccurate temperature spike with reaction. Case B) The correct amount of hydrogen atoms are added, resulting in a reaction with a small transient temperature spike. Time in this case is not related to the times used in the rest of the figures.

characteristics of the pulse had to be carefully selected because of how it affects the simulation, as seen in Figure 2.6. Atoms are literally added to the flow, and begin affecting the chemistry and thermodynamic properties of the gas as soon as they are injected.

As shown in Figure 2.1, there are two injection regions for air into the system (A1, A2), which necessitate the use of two different combustor volumes for the simulation. However, the complexities that the two area ratios of the combustor pose led to the adaptation of the single volume model shown in Figure 2.5. Although Eularian simulations have been performed using bluff body stabilized flames, the transient nature of the calculation will assume a Lagrangian moving flame volume, and will be discussed in Section 4.2 [36]. The final combustion products are exhausted to an infinite reservoir, mimicking atmospheric conditions. The supply tanks are located 40 feet away from the experiment, necessitating the inclusion of large inert volumes for which the air and methane can occupy before flowing into the combustor. The
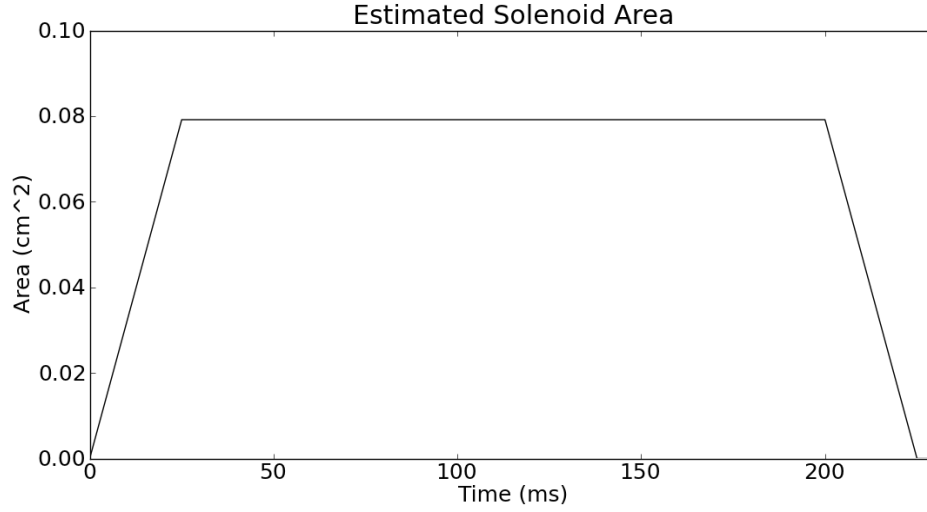
Fig. 2.7. Representation of the solenoid orifice area as a function of time. The 25 ms opening and closing timescale is depicted linearly for the opening and closing actuation.

role of the inertial volume is important, as pressure effects heavily influence the experiment, and therefore must be accounted for within the simulation. Although there is an inertial volume in the methane supply line, the effects of this volume are neglected. The relative orifice area of the methane is small enough to ensure that it will always be choked, and will therefore be providing a constant mass flow rate. For this reason, the inertial volume in the methane supply line is neglected.

Because the solenoid is a mechanical system, there is a physical timescale associated with opening and closing the device. This timescale is approximated to be 25 ms. During this period, the solenoid orifice area is changing, greatly affecting the mass flow rate ($\dot{m}_{sol}$) through the device. In an ideal case, the solenoid would open instantaneously, allowing air to move through it at a rate proportional to the upstream pressure, as shown in Figure 2.4. In reality, the 25 ms opening time will create a "pulse" discussed in later sections. This pulse is the result of the high pressure air in the inertial air supply volume being discharged into the combustion chamber. The solenoid connecting the high pressure inertial volume to the combus-

tor will be choked until the pressure in the inertial supply volume drops below the critical value for choking, described by Equation 2.3. When the solenoid is no longer choked, the mass flow rate ($\dot{m}_{sol}$) will be equivalent to the choked value of the air orifice ($\dot{m}_{Air}$). The area change of the solenoid is modeled in time, as shown in Figure 2.7. The opening and closing times are described as linear slopes for simplification of the problem. The area described is used in Equations 2.2 and 2.5 to calculate the mass flow rate of the solenoid ($\dot{m}_{sol}$).

3. EXPERIMENTAL TECHNIQUES

Imaging the transient flame phenomenon poses many difficulties due to the small timescales present in the experiment, and the generally low light conditions in the flame. Unlike laser-induced methods which generate photons, the present work relied on chemiluminescence, i.e. the emission of light as a result of chemical reactions. These complications were dealt with via two different methods which were applied to the transient flame.

3.1 The Image Intensifier

The main benefit of the image intensifier the ability to amplify the number of photons emanating from an experiment. This experiment used a 3rd generation (Gen III) ITT Night Vision image intensifier (FS9910C). An image intensifier has three primary components within its housing: the photocathode, the photoanode, and the microchannel plate (MCP) [37]. In this particular intensifier, gallium arsenide is used as the photoelectric material in the photocathode, and a P43 phosphor was used for the photoanode [38].

The quantum efficiency (QE) of an image intensifier is based on the photoelectric materials utilized, and is defined as:

$$QE = \frac{\#Photoelectrons}{\#Photons} \tag{3.1}$$

Gen III image intensifiers are known for their high QE, which can be in excess of 50% depending on the observed wavelength and the properties of the photoelectric material used [37]. The spectral response curve of the gallium arsenide photocathode is nearly flat for wavelengths of 450 nm–850 nm, ideal for imaging any flame in the visible spectrum.
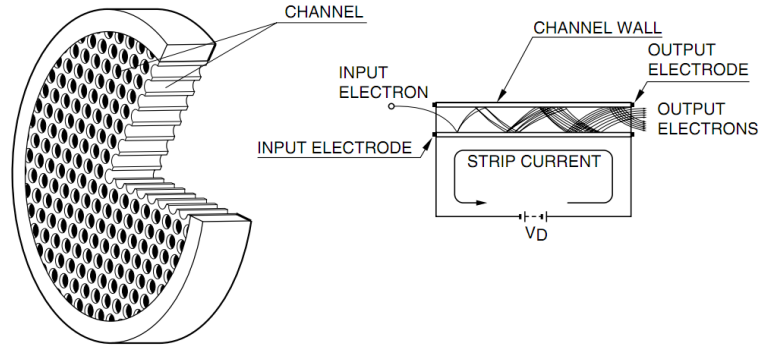
Fig. 3.1. Diagram of a Microchannel Plate (MCP), reproduced with permission from Hamamatsu Photonics [37].

The MCP is constructed using a glass wafer, which contains thousands of small glass tubes or slots, as shown in Figures 3.1 and 3.2 [37]. As the electrons enter the electrically charged MCP and ricochet through the channels, they are multiplied by making contact with the sidewalls of the tube [37]. The number of electrons generated is proportional to the voltage differential across the MCP. The outgoing electrons then strike the photoanode which emits photons to be captured either by eye or photodetector. The gain of the system is adjustable by altering the voltage differentials of either the photocathode, or the MCP.
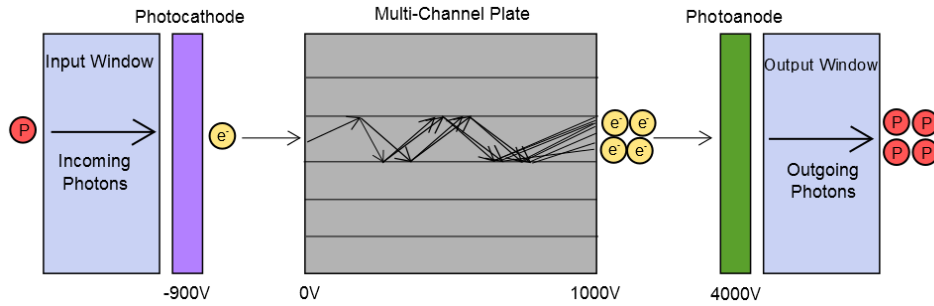

Fig. 3.2. Diagram of the operation of an image intensifier.

The photocathode is the most important component in regards to the transient supersonic flame. Timing is brought into the system by the methods mentioned in Section 2.1. The photocathode must be quickly pulsed to achieve optimal results. If it is not pulsed quickly enough, a "smearing" effect will appear in the photos taken. However, pulsing too fast could limit the amount of entering light, causing dim or noisy photos. There is a balance that must be found experimentally. The optimal gating value was found to be between 1–3 ms. Other experiments typically utilize laser induced methods for increasing light levels, providing intensifier gates as low as 2 ns [16]. Although the image intensifier was capable of gates as low as 20 ns, the low light from the experiment required the larger gate to capture the event with minimal noise.

High voltages are provided by an in-house built power supply, which utilizes a high voltage pulser for the photocathode, and a steady state high voltage power supply for the differential voltages across the MCP and photoanode, as shown in Figure 3.3. A 24V DC power supply provides energy for both the steady state high voltage power supply and the high voltage pulser. The high voltage pulser can be tuned between -500 V and -900 V, providing an extra gain control on the photocathode if desired. It is triggered by a TTL signal provided by either of the signal generators listed in Section 2.1, allowing precisely timed gating of the image intensifier. The steady state power supply provides an 8 kV potential, which was split using a voltage divider network, providing separate voltages for the MCP and photoanode. Low current needed to be ensured to keep from burning out the power supply, so resistance values in the $M\Omega$ range were chosen for use in the divider network. The fractions in Figure 3.3 show relative values that were used.

3.2   Charge-Coupled Device

CCDs operate using electronic shift registers to move an electrical charge out of the CCD pixels and into an A/D converter for digitizing the signal obtained [39].
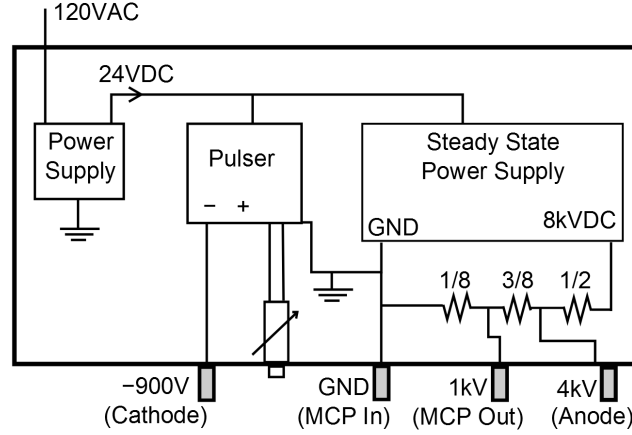
Fig. 3.3. Schematic of image intensifier power supply unit. The pulser has a variable resistor that provides voltage tuning of the negatively charged pulse. The voltage divider resistor network utilizes $M\Omega$ valued resistors, depicted as fractions to convey relative resistor values. The provided voltages apply to the intensifier depicted in Figure 3.2.

CCDs are often used for scientific purposes in large part due to their typically high quality photo-imaging abilities, pixel binning options, and cooling capabilities. Most CCDs present a high quantum efficiency of 60% or more (90% for state of the art CCD systems), with uniform and reproducible images, making them ideal for the laboratory environment.

A Santa Barbara Instruments Group (SBIG) Pixcel 255 (ST-5) astronomical detector was used to obtain intensified images of the emerging flame fronts. The images were gathered through CCDOps, a proprietary imaging software created by SBIG [40]. The ST-5 has a resolution of 320x240 pixels, with a pixel size of 10x10 μm [41]. The ST-5 was chosen because of its thermoelectric cooling abilities, mounting style, software support, and picture quality, all of which is related to the original purpose of astronomical imaging. Additionally, astronomical CCDs typically offer high signal to noise ratios (SNR = S/N), comparable to scientific CCDs.

The noise $\dot{N}$ of any shot-limited signal can be related to the actual signal, represented as photon counts $\dot{P}$ by the formula $N \sim P^{1/2}$. The SNR for such a simple system then follows as $SNR \sim P^{1/2}$, stating that an increase in signal levels will create a small increase in SNR [38]. However, physical systems contain more sources of noise which can be accounted for in the following equation:

$$SNR = \frac{\dot{P}Q\tau}{[(\dot{P} + \dot{B})Q\tau + \dot{D}\tau + N_{A/D}^2]^{1/2}} \qquad (3.2)$$

where $\dot{P}$ is the rate of arriving photons (s^{-1}), $\dot{B}$ is the arrival rate of background photons (s^{-1}), $\dot{D}$ is the electron generation rate from thermal effects on the CCD (dark current, in s^{-1}), $N_{A/D}$ is the read-out noise that is generated during the Analog-to-Digital conversion process (unitless), Q is the quantum efficiency of the detector (unitless), and τ is the exposure time of the image [38]. An image intensifier increases the output gain of incoming photons, which can be represented in the SNR as G:

$$SNR = \frac{G\dot{P}Q\tau}{[(\dot{P} + \dot{B})GQ\tau + \dot{D}\tau + N_{A/D}^2]^{1/2}} \qquad (3.3)$$

Minimizing the noise sources is essential to improving the quality of the images obtained. At least two of the noise sources can be attenuated. The background photons are eliminated in three ways, by operating within a light-tight area (reducing $\dot{B}$), by using short exposure times on the CCD (reducing τ), and by gating the image intensifier (also reducing τ). Dark current noise can be minimized using thermoelectric cooling, which is pre-installed on the ST-5 (reducing $\dot{D}$). The camera can cool the CCD to a steady state value of -17°C, drastically increasing the SNR of the camera. Pixel-binning is not supported by the ST-5, therefore the read-out noise cannot be eliminated.
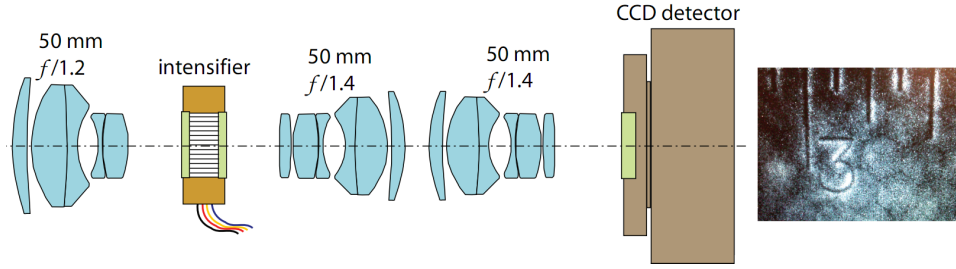
Fig. 3.4. Two dimensional representation of the coupling of the image intensifier to the CCD. Note the honeycomb shapes in the output image. These cells are unique to Gen III intensifiers. A protective film is placed on the photocathode to prevent electrons from flowing back into the photocathode. The honeycomb shapes are from the metal grid that supports the protective film.

3.3 Optical Relay

Typically, an image intensifier is fitted to an imaging system by a fiber optic plate. In this work, an optical relay consisting of multiple lenses was used instead. Despite the higher efficiencies obtained through fiber optic coupling, the optical relay was chosen due to its cost savings, versatility in the lab environment, and the inherent difficulty of applying a fiber optic plate to the intensifier output window. However, several problems arise when attempting to couple the intensifier to a CCD.

Lenses typically mount to a CCD using specifically designed connectors that vary between manufacturers. For this reason, Nikon lenses were exclusively used to ensure congruency when mounting components. Every lens has a specified register, which is the distance from the mounting ring to the focal point of the lens. This value is extremely precise and must be respected, as any errors will greatly influence the focusing of the optical system. Nikon lenses have a register of 46.5 mm with an F style optical mount [42].

The image intensifier provides an input/output window for observation, necessitating careful coupling of the Nikon lenses. A schematic of the system is shown in Figures 3.4 and 3.5. The f number of a lens is defined as f/D , where f is the
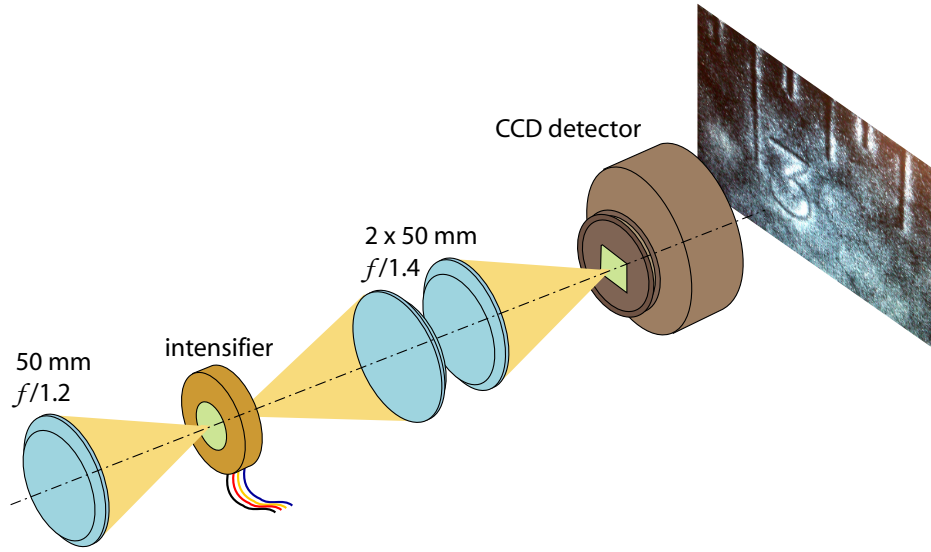
Fig. 3.5. Three dimensional representation of the optical relay system.

focal length of the lens, and D is its diameter. More light can be captured using a lower f number, because of the larger solid angle of collection. The amount of light transmitted through a lens will decrease with the square of the f number [43]. A Nikon prime f/1.2 is used as a collecting lens on the front of the system, as it will capture the most light for the intensifier. The f/1.2 must be placed exactly 46.5 mm away from the input window of the intensifier to ensure proper focus of the system.

The image from the output window of the intensifier is relayed to the CCD through two f/1.4 lenses placed front-to-front, as seen in Figures 3.4 and 3.5. The front-to-front method helps to cancel the geometric abberations introduced when working with spherical lenses. When planar light enters a spherical lens, the wavefronts at the exit become spherical [44]. Naturally, running the spherical wavefronts backwards through the same lens reverses the process, producing a planar image once more. The planar image is focused onto the focal plane array (FPA), completing the relay. The f/1.4 lenses are focused at infinity, allowing for 1:1 image conjugation from the intensifier to the CCD.
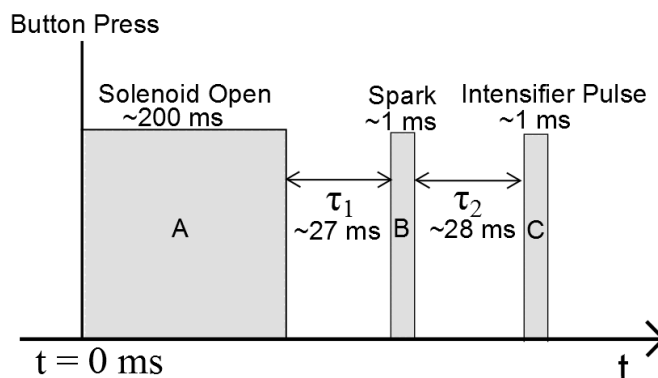
Fig. 3.6. Relative timescales used in the experiment. (A) represents the open solenoid time ($\sim$200 ms), (B) is the ignition spark ($\sim$1 ms), and (C) is the activation duration of the image intensifier ($\sim$1 ms). The experiment is initiated by a button press. The delay (τ_1) determines the ignition point, and is required for allowing the reactants to mix before combustion. The second delay (τ_2) determines which phase of the flame is captured. $\tau_2 = 28$ ms corresponds to the flame emergence from the nozzle.

3.4 Intensifier Timescale

The assembly of the intensifier system adds complexity to the timing system described in Section 2.1. The intensifier will require a gated signal in order to trigger the device, as discussed in Section 3.1. Figure 2.2 must now be updated to reflect the addition of the ICCD. The optimal trigger value for the photocathode pulser was experimentally determined to be between 1–3 ms. In order to capture the chemiluminescence from the emerging flame, a delay time is needed for the intensifier. The flame will take a certain amount of time to travel through the combustor and finally arrive at the nozzle, and will be discussed in Section 4.2. When it arrives at the nozzle, the ICCD can then capture the light. The flame travel time, or intensifier delay, was experimentally determined to be ≈ 28 ms. This new delay time can now be added to the timing system, expressed in Figure 3.6.
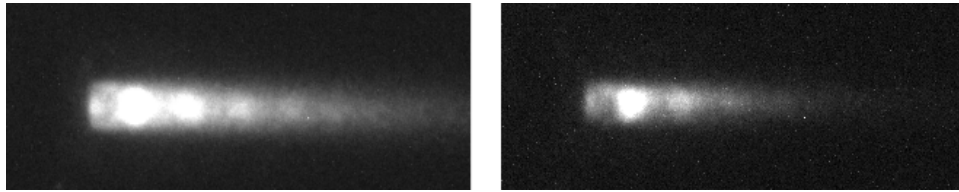
3.5 Intensified Image Data

Fig. 3.7. Singular flame imaging results in separate phases of flow observed at same delay times. Initial conditions inside combustor changes overall flame timescales, posing difficulties in time matching intensified images.

Intensified imaging was an overall success, but there were several problems encountered when using the system. Due to the limitations of the ST-5 CCD, the picture frame rate is much greater than 1 second. This means that unlike the schlieren data, multiple phases of a single transient flame cannot be captured. Instead, single images can be taken of separate flames, and then stitched together to create an overall progression of the flame. However, the experiment is sensitive to initial conditions, and therefore the flame does not perform exactly the same way with each trial. For example, two pictures of separate flames obtained with the same delay time after ignition are shown in Figure 3.7. Although taken at the same delay time, they do not correspond exactly due to the minute flow differences within the experiment (i.e. solenoid timescales, turbulent interactions from A1 and A2, etc.). Therefore, intensified flame progressions are not considered. Instead, the examination will be limited to singular images of singular flames.

Lastly, varying the CCD exposure time and intensifier pulse time can give very different results. The methods for minimizing noise in the system, stated in Section 3.2, are demonstrated in Figure 3.8. The picture on the right is the result of a long exposure of the CCD coupled with a short pulse from the intensifier. The chemilluminescence of the flame is visible, but there is increased noise in the photo. Referring to Equation 3.3, a long exposure of the CCD will result in an increase
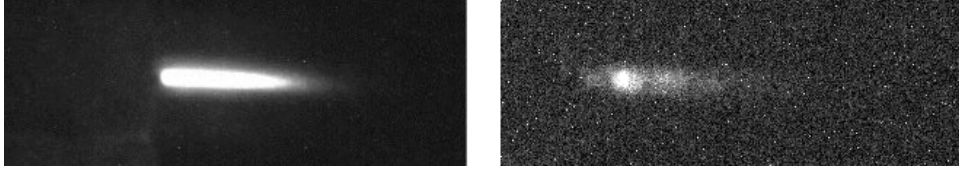
Fig. 3.8. Imaging difficulties using image intensifer. The left figure is an example of providing a large gate to the intensifier, resulting in a smeared photo with overexposed regions. The right figure the result of long exposure times of the CCD, causing increased noise in the image obtained.

of τ, $\dot{B}$, and $\dot{D}$, while keeping $\dot{P}$ the same. What results is an increase in noise, lowering the overall SNR of the system. The left picture is the result of increasing the gate width provided to the image intensifier. By doing so, a smearing effect is produced on the flame. All data regarding the supersonic jet structure is lost due to the increased gain of the photons emitted during combustion.

3.6   Schlieren Imaging

Light, when moving through a volume of air, will be refracted depending on the inhomogeneity in the density gradients and the resulting index of refraction [23]. Schlieren is a property of any transparent medium, including solids, liquids, and gases, which result from temperature changes, high speed flows, or the mixing of dissimilar fluids, amongst many other possible causes [23]. Essentially, density variations of some order (ρ, $\nabla\rho$, $\nabla^2\rho$) will produce visible streaks in a schlieren system [23]. Schlieren can provide an observer with a qualitative understanding of the complexities present in a flow. In the present work, the supersonic structure of the transient flame is observed using a schlieren setup, and is captured using a high speed camera.

The high speed cameras used in the schlieren portion of the results are the Casio EX-FH25 and the Fujifilm HS10, both of which render video at 1000 frames per
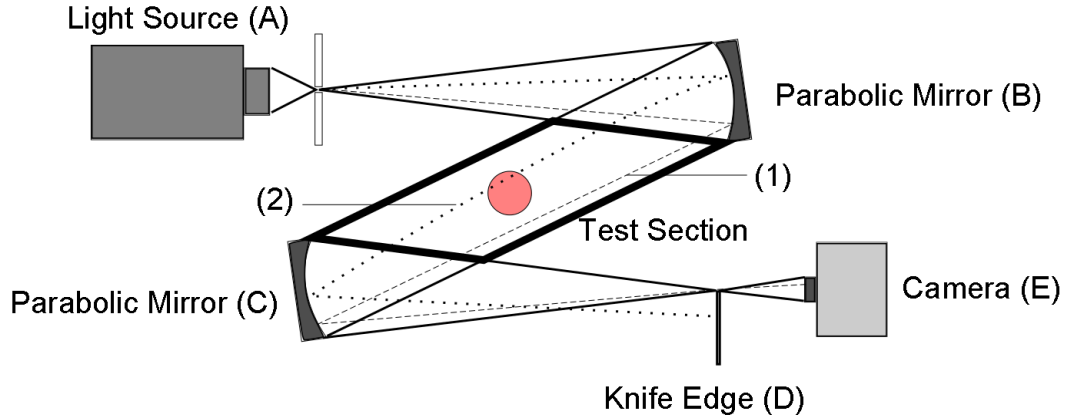
Fig. 3.9. Depiction of a Z-type schlieren setup. Light generated at (A) is focused onto the parabolic mirror (B). (B) collimates the light through the test section, arriving at the second parabolic mirror (C). (C) focuses the incoming light to a point at (D). The knife edge acts to block light rays that were refracted through the test section. Light ray (1) did not encounter an obstruction, and so passes through to the camera (E). Light ray (2) is refracted by the obstruction, and is consequently blocked by the knife edge at point (D).

second with a resolution of 224x64 pixels. This equates to one frame per millisecond, providing detailed views of the supersonic flow structure emanating from the combustor. Both cameras utilize a new complementary metal–oxide–semiconductor (CMOS) FPA. This new technology offers high speed imaging at a low cost.

There are several ways to construct a schlieren system, but the Z-type system was chosen due to its simplicity, as seen in Figure 3.9 [45]. The Z-type system utilizes two concave mirrors to collimate/decollimate the light rays. The system operates by first condensing light through a pinhole, which is then focused onto the first parabolic mirror (B). The mirror is located exactly 17.5 in away from the pinhole, causing the reflected light to be collimated. The collimated light is then focused by a second mirror (C) into a single point (D). At the focal point of the second mirror, a knife edge is used to cut off any light that is refracted due to gradients in the flow, as represented in Figure 3.9 by (2). The position of the knife edge is important, as it

controls which gradient directions will be amplified. In this experiment, due to the fast exposure times of the high speed cameras, a great deal of light was required to observe the transient flame. The light source utilized was a 150W fiber-optic haloid lamp condensed through a microscope lens.

The mirrors are angled at 8°, providing an incoming and outgoing beam angle of 16°. The Z-type schlieren system will always have some error in the focused beam due to astigmatism [23]. Astigmatism is the failure to focus a beam to a point, and results from symmetry breaking [23]. It should be noted that with the mirrors used in the Z-type system, any angle of the reflected light will produce astigmatic error. The problem cannot be rectified, by definition of the optical geometry. However, the abberations due to astigmatism are small and are not overtly visible in the gathered data.

4. RESULTS AND SUMMARY

In this chapter, results will be presented from the zero dimensional computation, schlieren imaging, and the ICCD. A relationship is made between the computational model and the schlieren high speed images. This is done by analysis of timescales within both systems. Additionally, flame properties are tracked through time and space using a Lagrangian reference frame. This allows flame properties to be analyzed just prior to the nozzle entrance. Flow properties through the nozzle are calculated using one dimensional isentropic flow relations. The calculation of thermodynamic properties downstream of the nozzle allow a comparison to be made between the schlieren images and the combustor model.
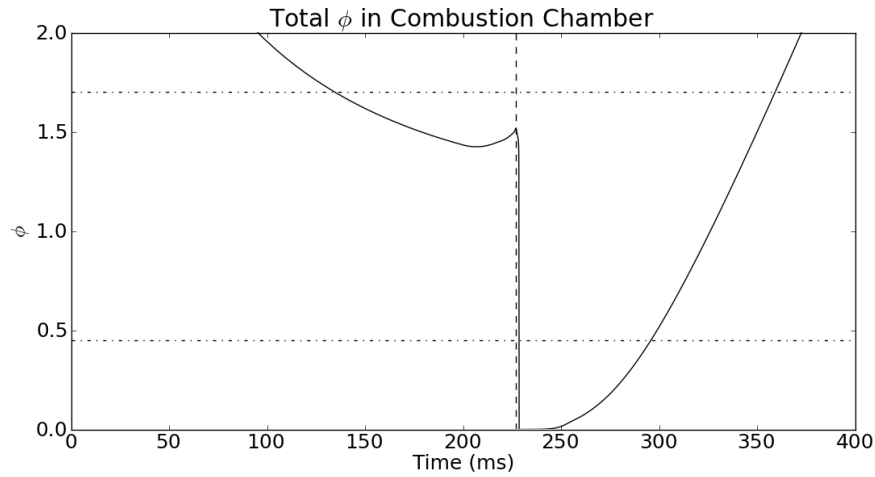

Fig. 4.1. Transient equivalence ratio in the combustor, computed using the zero-dimensional model. Horizontal dashed lines denote the upper and lower limits of flammability for methane in air [28]. The ignition point is at $t = 227$ ms, corresponding to a ϕ of approximately 1.5. The ignition delay is representative of experimental values, resulting in a small rise in equivalence ratio just prior to combustion.

4.1 Transient Zero-Dimensional Thermochemistry in the Combustor

Several timescales are important during the operation of the transient flame system. The process is initiated at $t = 0$ ms by opening the solenoid. The length of time that the solenoid is open is crucial in creating a flammable mixture for the system, as seen in Figure 4.1. The equivalence ratio ϕ is determined by the overall mass ratio of fuel and oxidizer in the combustor as it relates to the stoichiometric mass ratio. The fuel-air mass ratio in the chamber is dynamic, and is computed using the mass fractions reported by Cantera for each time step. When the experiment begins, the chamber is initially filled with methane, corresponding to an unbounded (infinite) equivalence ratio. Gradually, as air enters the chamber, the equivalence ratio will decrease until $t = 200$ ms. The equivalence ratio at $t = 200$ ms is based on the choked orifice values listed in Section 2.1 and corresponds to a local minimum of a transient case. If the calculation continued indefinitely, a steady state value of $\phi = 1.4$ would be reached.

At $t = 200$ ms, the solenoid begins to close. Ignition occurs at $t = 227$ ms. The lack of incoming air will result in ϕ increasing slightly, just prior to combustion. The 27 ms delay in ignition is needed in the experiment for gas mixing, but the WSR used by Cantera does not need this delay time. It is included in the simulation for ensuring as much possible continuity in the comparison between the experimental and simulated timescales. During combustion, the methane and oxygen are being consumed, causing the equivalence ratio to drop to zero. Because the methane continues flowing into the combustor and the solenoid is closed, the the lack of air in the system will create a second unbounded equivalence ratio at time $t \gg 250 ms$.

When a flame is present, the fuel and oxidizer will be depleted, leading momentarily to $\phi = 0$. This duration between $t \approx 230$ ms and $t \approx 255$ ms, shown in Figure 4.1, shows the extent of the flame. Experimentally, the ignition point is determined by inspection of the flame, and audible cues. Ignition at a ϕ closest to one will result
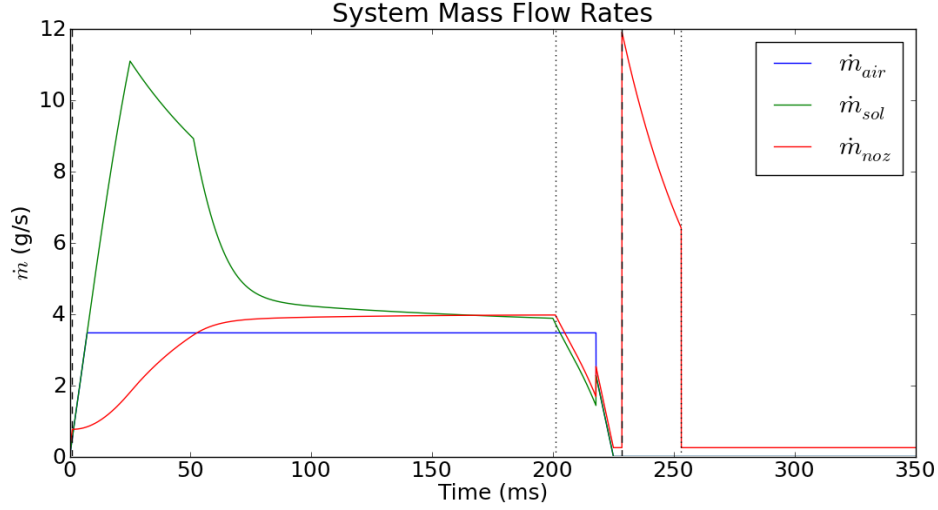
Fig. 4.2. The relative mass flow rates in the pressure system are calculated from Equations 2.2 and 2.4. They are based on several factors, including relative pressures, orifice areas, and choke conditions. Dashed lines represent the choked conditions for the nozzle. Dotted lines represent the transition from sonic to subsonic flow (unchoked) at the nozzle.

in the most vigorous combustion. Deviation from the optimal ignition point can still result in combustion, but it will result in a less intense flame.

The equivalence ratio in the system is based on the mass flow rates provided into and out of the WSR. As shown in Figure 4.2, the mass flow rates are computed at each time step using Equations 2.2 and 2.4 for the mass flow controllers that link each of the four pressure volumes, denoted as (1)-(4) in Figure 2.3. Initially, the mass flow rate through the nozzle ($\dot{m}_{noz}$) will be equal to the mass flow rate of methane ($\dot{m}_{fuel}$) because the nozzle is large enough to exhaust the small amount of incoming fuel, and because the solenoid is closed. When the solenoid opens, it will have a large area and mass flow rate ($\dot{m}_{sol}$) that is exhausting into the combustor, choking the nozzle. The pressure in the inertial volume will exhaust into the combustor transiently, until the pressure in the inertial volume is almost the same as the pressure in the combustion
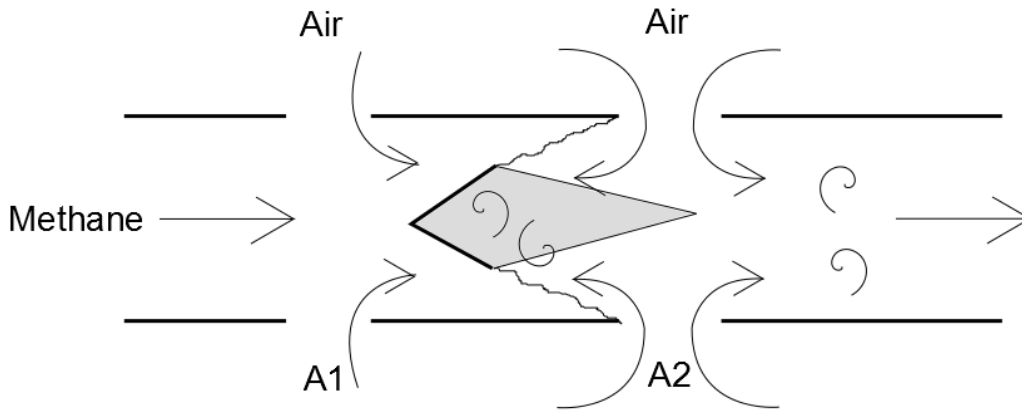
Fig. 4.3. Depiction of the possible mixing solution, allowing for a flammable mixture to be present at time of ignition.

chamber. When the inertial volume pressure lowers, the air orifice will become choked ($\dot{m}_{air}$), providing a constant mass flow rate until such time that the solenoid closes.

The interplay between all of the mass flow rates and volumes is performed by Cantera, where the choke conditions and mass flow rates are checked at each step, and updated for the next step. This allows a qualitative model to be produced based on simple assumptions, such as inviscid flow when subsonic, and isentropic flow when supersonic. The criterion for whether or not the nozzle chokes is based on the incoming mass flow rates for the system. If the incoming mass is lower than the outgoing mass, then the nozzle will not be choked. Additionally, if a large pressure and temperature increase occurs due to combustion, then the nozzle will choke. The two choke points are indicated in Figure 4.2 by dashed lines. In the same figure, the subsonic flow points are denoted by dotted lines.

One of the problems faced when implementing a zero-dimensional model is the assumption of perfectly mixed gases. The zero-dimensional model cannot capture gradients in space and mixing. When two gases are inserted into the reactor, the calculation considers them instantly and perfectly mixed. In a steady state calculation, this may not pose a problem. However, the transient behavior of the experiment is

heavily dependent on mixing time, implying that a mixing characteristic time must be accounted for. This mixing time was experimentally found to be approximately 27 ms. This means that in the experiment, the ignition is delayed after the solenoid is closed by approximately 27 ms. This is reflected in the simulation as well, although there are repercussions for delaying the ignition, as shown in Figure 4.1.

When the experiment is initiated, gas flows into the combustion chamber and is allowed to mix with the methane in the flame tube through areas A1 and A2, as shown in Figure 2.1. If the flow were to be acting in steady state, then the mixture would never ignite, due to the ratio of A1 and A2 and the metering orifice areas described. The equivalence ratio near the spark plug would exceed the limits of combustion, causing a failed ignition. However, the transient system ignites. This phenomenon can be explained due to the large turbulence effects generated by the flame holder boundary layer, and the sharp corners the flow encounters moving through A1 and A2. Figure 4.3 illustrates the turbulent mixing occurring near the flame holder. The flame holder provides a recirculation region in which the methane and air can mix, allowing for a flammable mixture to be created. Additionally, the swift movement of incoming air will result in an impinging jet through A1 and A2, causing more air to enter the recirculation region. For a brief moment, the mixture becomes flammable, but only in a transient configuration.

The graph in Figure 4.4 details temperature within the combustor as a function of time. The temperature remains relatively constant within the system until the ignition point at $t = 227$ ms. There is a minor temperature rise at $t \approx 40$ ms due to the sudden accumulation of mass in the combustion chamber. At ignition, the combustor temperature experiences a sharp increase due to chemical energy release. Because the air supply begins to decrease at $t = 200$ ms, the high temperature provided by reactions cannot be sustained with the diminishing oxygen levels. Therefore, the temperature within the combustor undergoes a decrease as the reactions cease to take place. What results is a gradual return to steady state, ambient levels ($t \gg 250$
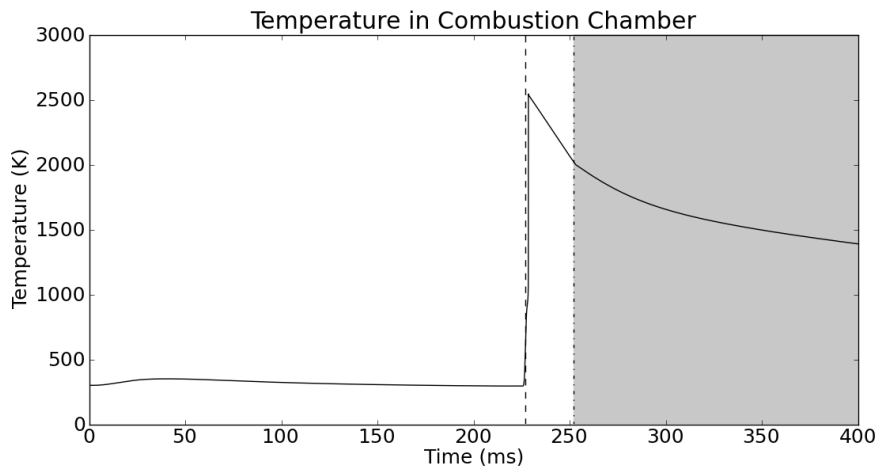
Fig. 4.4. Time evolution of the temperature profile within the combustor. The grayed-out portion relates to the time at which the flame parcel reaches the nozzle, exhausting out of the combustor.

ms) with no incoming air flow. Given enough time, the system would return to the exact state observed at $t = 0$ ms.

The chemistry of the flame can be quantified by analyzing the molecular makeup of the combustor gases as they change through time and space. Only major gas species are shown, although there are 53 different species used by the GRI-3.0 reaction mechanism. As discussed in Section 2.2, hydrogen atoms are used to ignite the flow, and are therefore extremely important in determining the state of combustion. The initial hydrogen addition is provided by a Gaussian pulse. This pulse reaches its maximum amplitude at $t = 227$ ms, attempting to mimick the ignition used in the experiment. The actual ignition time between the experiment and simulation will vary slightly, due to the methods in which they are each ignited. The experiment is ignited using a spark plug, which operates very quickly. However, igniting a flow in Cantera is done through hydrogen atoms, which will need time to react with the flow before providing combustion. This small reaction delay can be seen in Figure 4.5. The reaction delay in the simulation is approximately 1 ms.
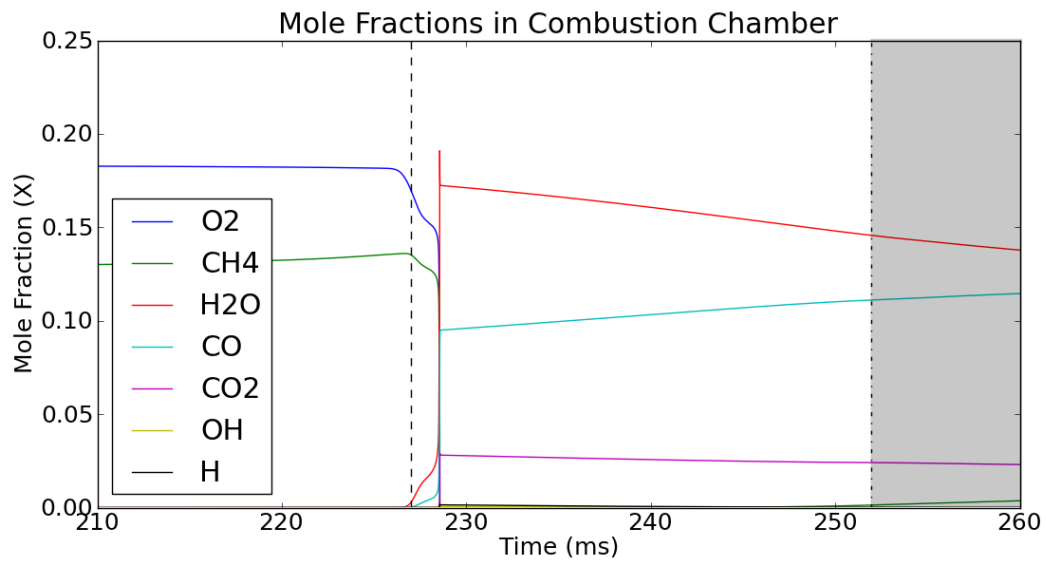
Fig. 4.5. Depiction of major mole fractions within the combustion chamber as a function of time. The rich flame ($\phi \approx 1.5$) will result in incomplete combustion, producing excess levels of CO. The dashed line indicates the maximum mass flow rate of pulsed hydrogen atoms ($\dot{m}_H$). Full reaction is observed approximately 1 ms after the maximum of the provided pulse. The grayed-out portion relates to the time at which the flame reaches the nozzle, exhausting out of the combustor.
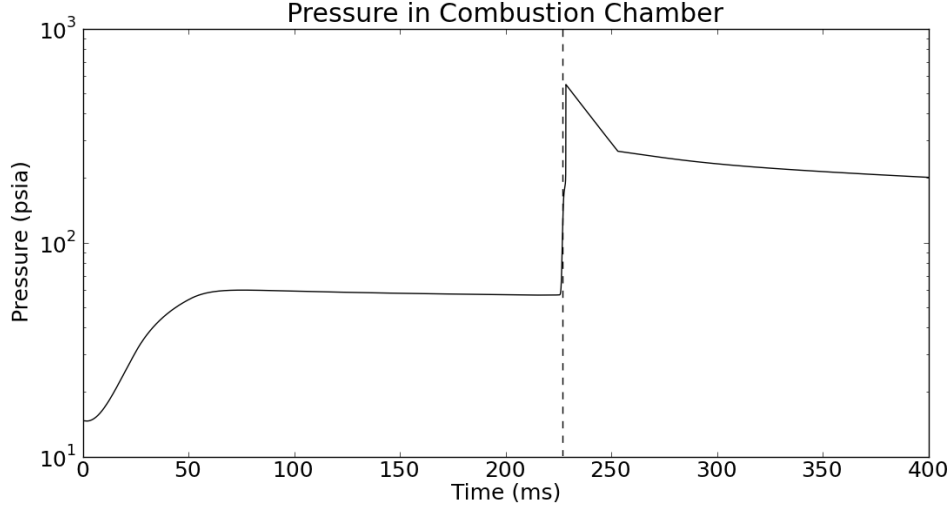
Fig. 4.6. Pressure within the combustion chamber. The sudden influx of air from the opening solenoid ($\dot{m}_{sol}$) at $t = 0$ ms will cause the pressure to rise in the combustion chamber. When combustion occurs, the pressure is drastically increased due to the energy release from the reaction.

The pressure profile within the combustion chamber in Figure 4.6 is tied very closely to the mass flow rates in Figure 4.2. When the solenoid begins to open at $t = 0$ ms, there is a large back pressure behind it. The nozzle in the combustion chamber is not initially choked, so the pressure within the chamber is atmospheric. The pressure difference across the solenoid will initially choke the solenoid orifice. Because the area of the solenoid is increasing when $t < 25$ ms, the mass flow rate ($\dot{m}_{sol}$) is also going to increase sharply. This sudden influx of air will choke the nozzle, resulting in accumulated pressure within the chamber. As the pressure in the inertial volume and the combustion chamber equalize, the upstream air orifice will choke, providing a constant mass flow rate ($\dot{m}_{Air}$) into the system, until the solenoid is closed. Soon after the solenoid closes, ignition occurs, creating a large pressure spike within the combustion chamber. The high pressure within the combustor will eventually be depleted through the nozzle ($\dot{m}_{noz}$).

4.2   Lagrangian Flame Progress

In order to link the transient zero dimensional model to experiment conditions, it is essential to account for the time the flame spends in the combustor before exiting the nozzle. If the time at which the flame exits the nozzle can be defined, then a direct comparison can be made between the simulation and the experiment regarding the temperature and flame composition downstream of the nozzle.

A convective timescale can be estimated by modeling the velocity of the flow within the combustor, and assuming a Lagrangian reference frame, as shown in Figure 4.7. The flow velocity will be a function of the system mass flow rate $(\dot{m})$, area of the flame tube A, and the density ρ of the system using a one dimensional model. The instantaneous flow velocity can be calculated at each time step using the following equation:

$$u(t') = \frac{\dot{m}(t')}{\rho(t')A} \tag{4.1}$$

where t' is a time variable, and u is the velocity in the chamber. The density of the flame parcel will be assumed constant as it moves through the combustor. This assumption will be examined at the end of this section, by comparing the relevant
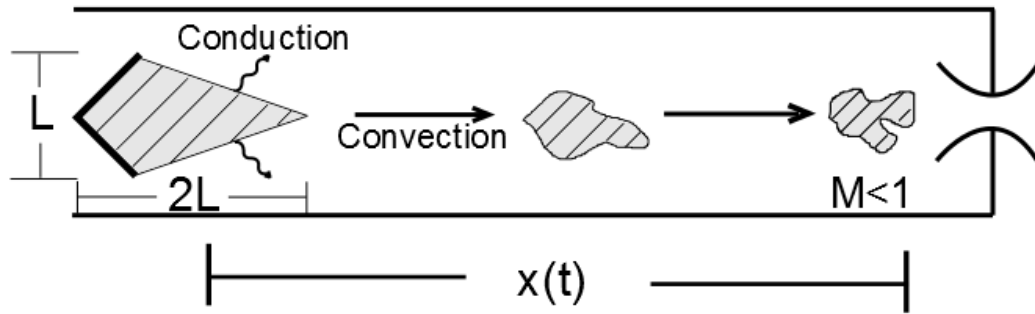

Fig. 4.7. Tracking of the flame parcel as it moves towards the nozzle. The heat loss from conduction is negligible compared to convective losses, allowing for estimation of values downstream of the nozzle.

timescales. By integrating the velocity equation with time, the distance that the fluid parcel moves can be computed:

$$x(t) = \int_0^t u(t')dt = \int_0^t \frac{\dot{m}(t')}{\rho(t')A}dt' \tag{4.2}$$

where $x(t)$ is the distance traveled by the fluid parcel. The distance d_{flame} required for the fluid parcel to travel from the ignition spark to the nozzle entrance is known from the geometry of the combustor. Therefore, by monitoring the value of $x(t)$ and t at each time step during the integration of Equation 4.2 and halting the calculation when $x(t) = d_{flame}$, the convective timescale of the model is found. The convective timescale for the simulation is calculated to be $t = \tau_2 \approx 25$ ms. This value agrees well with observed experimental values, as will be discussed in Section 4.4.

During the progression of the flame, it will be susceptible to heat loss from conduction through the combustor. The losses would complicate the model, as added heat loss effects are not currently considered in the simulation. Therefore, it is prudent to estimate whether the losses from conduction are prominent. If the flame can be convected to the nozzle faster than heat can be lost due to conduction, then the flame computed by the model can be directly linked to the experiment. The relative timescale of conduction can be approximated using dimensional analysis of thermal diffusivity (α). The units of α are m^2/s, indicating a need for a relative length scale (l) and a characteristic timescale (τ_c), and can be related as:

$$\alpha = \frac{l^2}{\tau_c} \tag{4.3}$$

The length scale can be determined using the geometry of the fluid volume (V) created by the flame holder, as shown in Figure 4.7. For the relatively low velocities within the combustor, this fluid parcel volume (V) can be estimated as a function of the flame holder geometry, in this case being obstruction height (L in Figure 4.7) [13]. This recirculation volume is based on experimental data compiled from Edelman,

and is estimated to extend approximately two obstruction heights downstream (2L in Figure 4.7) [13]. Therefore, the size of the fluid parcel volume is known. The length scale l for the thermal diffusivity can then be defined as $l \approx V^{1/3}$.

The Sutherland model can be used to approximate the thermal diffusivity of the fluid parcel as it undergoes combustion:

$$\frac{\alpha_{burn}}{\alpha_o} = (\frac{T}{T_o})^{1.7} \tag{4.4}$$

where α_o is the thermal diffusivity of the unburned gas, α is the high temperature diffusivity, T_o is the unburned temperature, and T is the temperature of the burning gas [46]. The thermal diffusivity of a gas α_o can be related to the kinematic viscosity ν_o as $\alpha_o \sim \nu_o$. Therefore, the Sutherland model can be used to estimate a thermal diffusivity for the high temperature fluid parcel. Using Equation 4.3 in conjunction with newly defined length scales l and the high temperature thermal diffusivity α_{burn}, the timescale τ can be estimated as:

$$\tau = \frac{V^{2/3}}{\alpha_{burn}} \tag{4.5}$$

Equation 4.5 provides an approximation of the characteristic diffusion (conduction) time through the fluid volume shown in Figure 4.7. The characteristic conduction time is calculated to be $\tau_c \approx 100$ ms.

The difference between the conductive timescale ($\tau_c \approx 100$ ms) and convective timescales ($t = \tau_2 \approx 30ms$) is very large ($\tau_c > \tau_2$). This means that the losses due to conduction will be negligible compared to the speed at which the flame is convected downstream to the nozzle. Therefore, conductive losses to the system may be disregarded and the density may be considered constant.

Equation 4.2 connects time from the WSR model to distance traveled from the ignition source in the experiment. With this relation, one may substitute distance for time in the simulation and obtain the results based on distance traveled, rather
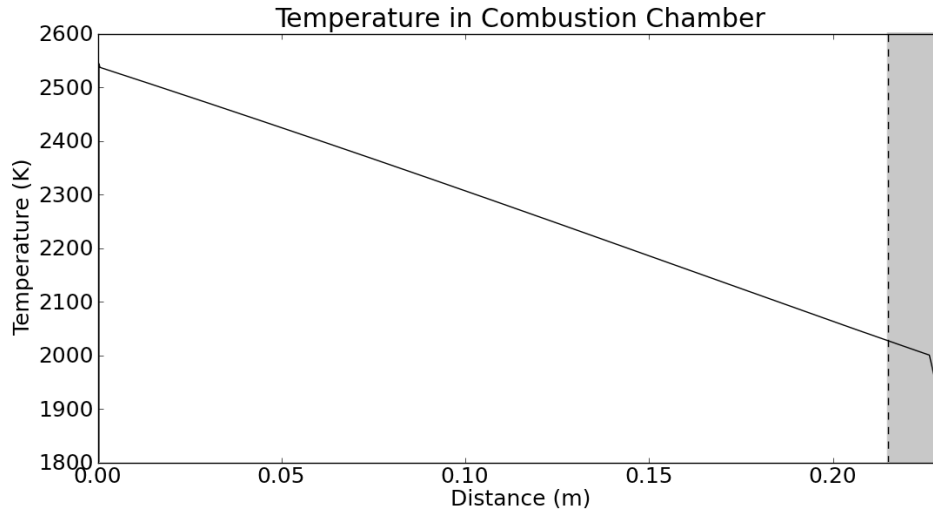
Fig. 4.8. Distance evolution of the temperature profile within the combustor. Zero distance corresponds to ignition at the flame holder. The grayed-out portion relates to the where the nozzle is located. This is the distance at which the flame reaches the nozzle, exhausting out of the combustor.

than time. Figure 4.8 details an example of this substitution, showing temperature change with distance as the flame parcel moves through the combustor towards the nozzle. The grayed-out areas indicate the point at which the flame parcel reaches the nozzle, both temporally and spatially, and should be considered as the point at which the flame exits the combustor. Therefore the data past this point should not be considered. The downward slope of the temperature indicates that the flame is cooling down before it gets to the nozzle. This is caused by several reasons. The pressure in the combustor is dropping drastically at this point, which will lower the other parameters inside the combustor, based on the ideal gas law. Additionally, the flame is reacting while moving towards the nozzle. The reaction began very rich, so it will not be able to sustain reaction. Therefore, the flame will not be able to provide enough energy to keep the temperature up. This can be seen in Figure 4.9. The chemical composition of the flame is also changing through space. The rich flame is
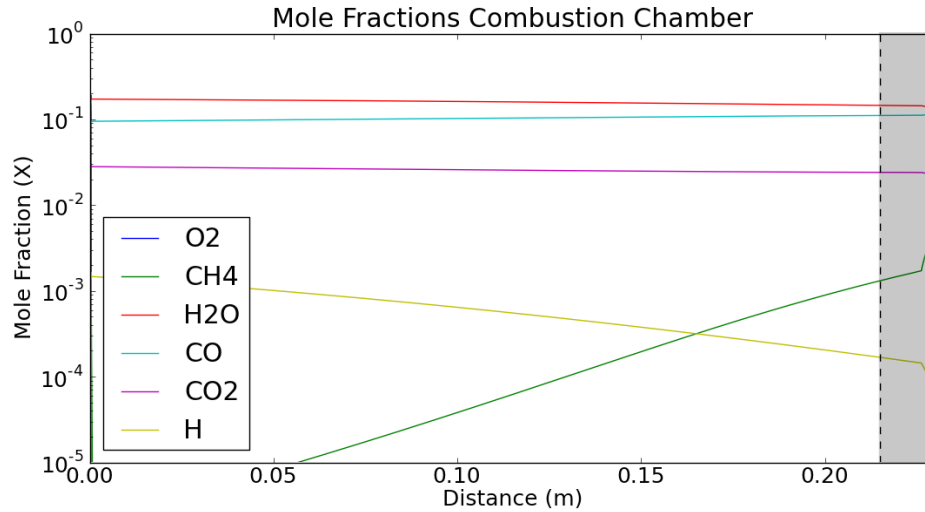
Fig. 4.9. Depiction of the mole fractions throughout combustion as distance traveled by the flame. Zero distance corresponds to ignition. The grayed-out portion relates to the where the nozzle is located. This is the distance at which the flame reaches the nozzle, exhausting out of the combustor.

starting to extinguish when it reaches the nozzle, shown by the increase in methane. If the reaction were still taking place, the methane would be in the process of being consumed. Because it is rising, the reaction must be slowing down.

One shortcoming of using the Lagrangian approach within a WSR lies in the idea of the flame parcel being an "open system". If the fluid parcel were truly moving in the combustor with speed equal to the surrounding flow, outside gases would not be entering the parcel, as is indicated in Figure 4.9. However, if considered for qualitative purposes it is applicable to the experiment. The ability to connect the timescales of the experiment to the WSR is valuable information, as it can be applied to many other simulations. Transforming a zero-dimensional model into a one-dimensional model is especially useful for transient problems, as it can help to describe the properties of a system as it evolves through space, and not just time.
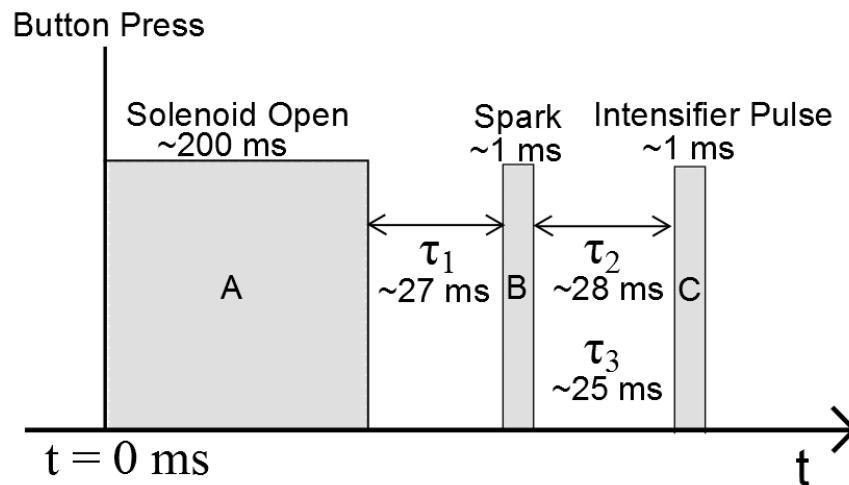
Fig. 4.10. Relative timescales used in the experiment. (A) represents the open solenoid time ($\sim$200 ms), (B) is the ignition spark ($\sim$1 ms), and (C) is the duration of activation of the image intensifier ($\sim$1 ms). τ_0 is the initiation of the experiment, signified by a button press. The first delay (τ_1) determines the ignition point, and the second delay (τ_2) determines which phase of the flame is captured. τ_3 is from the Lagrangian approximation and corresponds to τ_2.

Finally, Figures 2.2 and 3.6 can be updated to include the newly calculated travel time of the simulated flame, as shown in Figure 4.10. This value corresponds directly to the delay set by the ICCD. Experimentally, the flame travel time is found to be 28 ms, as indicated in Figure 4.10 by τ_2. The Lagrangian approximation calculates the flame travel time to be 25 ms (τ_3), providing good correlation between the simulation and the experiment.
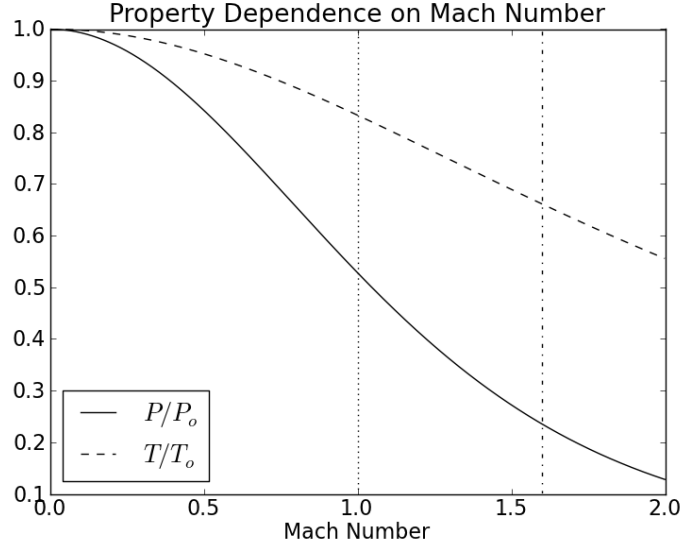
4.3   One Dimensional Nozzle Expansion

Fig. 4.11. The flow properties depend directly on the Mach number of the flow. Critical points are dictated by the values at $M = 1$. If the pressure ratio at the critical point is exceeded, the flow will become supersonic ($M > 1$) downstream of the nozzle throat. Nozzle geometry dictates an exit Mach number of 1.6, giving known values for temperature and pressure at the nozzle exit.

The regime for nozzle flow can be determined using Equation 2.3. If the ratio of downstream (atmospheric) pressure to upstream (combustor) pressure does not reach the critical value described by Equation 2.3 at the nozzle throat, then flow downstream of the nozzle throat will remain subsonic. Conversely, if the critical pressure is reached, then the Mach number at the nozzle throat will be $M = 1$, resulting in a maximum nozzle mass flow rate ($\dot{m}_{nozzle}$). Figure 4.11 details the downstream (nozzle exit) to upstream (combustor) pressure and temperature ratios at specified Mach numbers for a constant specific heat ratio γ relating to air. The critical pressure ratio is described by the ratio at $M = 1$. If the ratio of atmospheric pressure to combustor pressure is less than the critical pressure ratio, then the flow
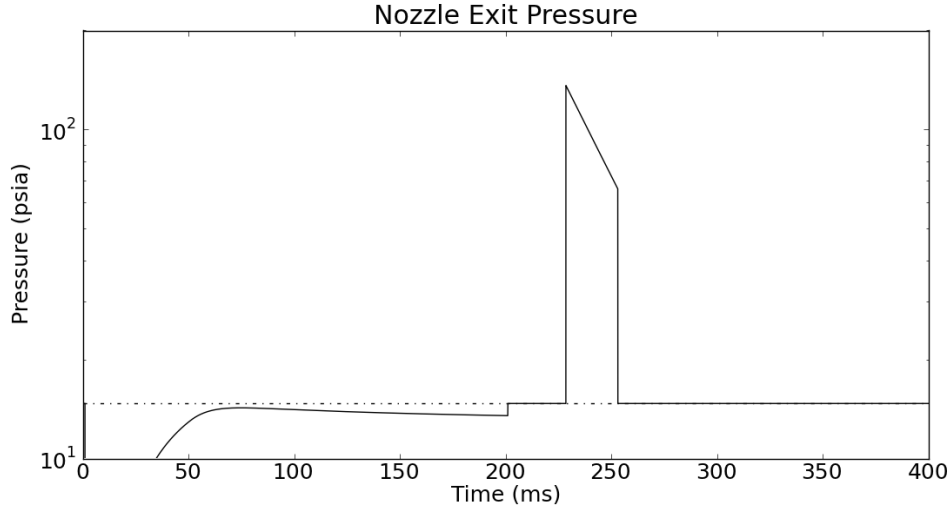
Fig. 4.12. Computed pressure at the nozzle exit during transient flame simulation. The discontinuity at $t \approx 230$ ms and $t \approx 255$ ms is the result of switching between subsonic and supersonic flow regimes. The initial choked behavior ($t < 200$ ms) corresponds to an overexpanded jet. The pressure rise from combustion creates an underexpanded jet at nozzle exit. A brief region of subsonic flow is observed between 200 ms $< t <$ 230 ms. The dashed line represents atmospheric pressure.

will reach supersonic speeds past the nozzle throat. It is assumed that due to the small size of the nozzle used in the experiment there will be no shock waves present in the nozzle. Additionally, isentropic flow can be assumed if the expansion process is both adiabatic and reversible [2]. Therefore, once the supersonic regime is obtained downstream of the nozzle throat the pressure and temperature at the nozzle exit will be dependent entirely on the combustor conditions. In the case of subsonic flow, it is assumed the exit pressure and temperatures are approximately equal to the ambient conditions downstream of the nozzle.

The expansion of a flow through a choked nozzle can be assumed isentropic (ds = 0) in the absence of strong waves or reaction. It is assumed, based on the size and contour of the nozzle, that there will be no separation within the nozzle, and

therefore no shock waves. For this model, it is also assumed that the chemistry of reaction is frozen through the nozzle [14]. This approximation ensures there is no entropy change due to reaction within the flow. These assumptions allow one dimensional isentropic equations to be used to predict the values for temperature and pressure at the nozzle exit. The pressure at the nozzle exit is shown in Figure 4.12. Pressure and temperature are determined using the one dimensional isentropic nozzle equations:

$$\frac{P}{P_o} = (1 + \frac{\gamma - 1}{2}M^2)^{\frac{-\gamma}{\gamma - 1}} \tag{4.6}$$

$$\frac{T}{T_o} = (1 + \frac{\gamma - 1}{2}M^2)^{-1} \tag{4.7}$$

where P_0 is the chamber pressure, P is the nozzle exit pressure, T_o is the temperature in the combustor, which is assumed at stagnation conditions, and T is the nozzle exit temperature [2]. The exit Mach number is known from Section 2.1, and γ is computed at each time step by Cantera. The initial choked condition from Figure 4.2 results in a combustor pressure that is slightly less than 4 atmospheres. When isentropically expanded using Equation 4.6, the pressure at the nozzle exit will be slightly lower than atmospheric. This is characteristic of an overexpanded jet. Ideally, a nozzle is most efficient when $P_{exit} = P_{atmospheric}$. When $P_{exit} < P_{atmospheric}$, the jet is overexpanded by the nozzle. Conversely, if $P_{exit} > P_{atmospheric}$, the jet is not expanded enough, or underexpanded.

Figure 4.12 details the exit pressures calculated in the simulation. As discussed, the nozzle will choke very early in the simulation. What results is an overexpanded jet during the first choked region, until $t \approx 200$ ms. When the solenoid begins to close, the incoming mass flow rates to the combustor ($\dot{m}_{sol}$ and $\dot{m}_{fuel}$) cannot sustain the choked condition, and so the nozzle will become subsonic. This is indicated in the figure from $t = 200$ ms to $t \approx 230$ ms. Since the flow is ignited at $t = 227$ ms, the pressure and temperature in the combustion chamber will rise dramatically, as calculated by Cantera in Figures 4.4 and 4.6. The conditions experienced by
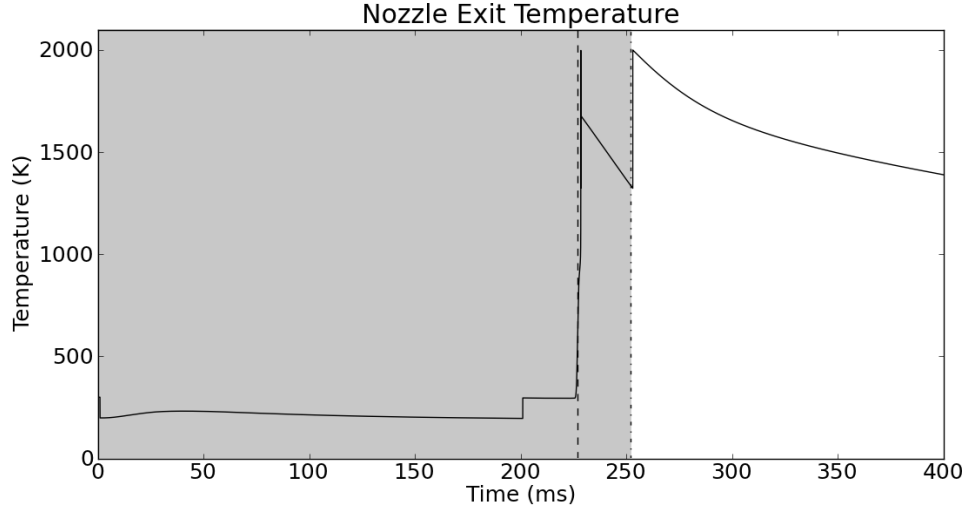
Fig. 4.13. Computed temperature at the nozzle exit during transient flame simulation. The greyed-out region pertains to temperatures not observed at the nozzle due to the convective timescales within the combustor. The discontinuity at $t = 255$ ms is the result of switching from a supersonic regime to a subsonic regime, as described by Equation 4.7.

the combustor during reaction will choke the nozzle a second time, resulting in an underexpanded jet, calculated from the isentropic flow relations. As the temperature and pressure of the system is quickly exhausted through the nozzle, the nozzle will no longer be choked, resulting in atmospheric exit pressures ($t > 255$ ms). The discontinuity in the pressure profile is from the sudden transformation of a subsonic flow to a supersonic flow. Although in reality this transition would be a smoother curve as the flow would need time to accelerate, it would still be a relatively fast transition. Therefore, it is a good approximation of the transformation from subsonic to supersonic flow.

The same assumptions used in calculating the nozzle exit pressure also apply to calculating temperature. The temperature at the nozzle exit can therefore be computed using Equation 4.7. The grayed-out portion of the nozzle exit temperature profile in Figure 4.13 is data not observed in the experiment, because the flame

parcel has not yet reached the nozzle. Therefore the temperatures calculated before this time will not be observed experimentally. The temperature computed at the exit is based directly on the combustor temperature. As discussed already, the zero dimensional model that is used to compute the reactor is transformed using Lagrangian particle tracking. In this work, the assumption is made that the flame parcel exiting the combustor will have properties very close to the one predicted by the program.

Figure 4.13 depicts is the simulated temperature profile at the nozzle exit based solely on the combustor temperature, and the choked condition. The discontinuities at $t = 228$ ms and $t = 255$ ms are from the instantaneous switching of a subsonic to supersonic regime, and from a supersonic to subsonic regime, respectively. When the nozzle is not choked, the nozzle exit temperature is approximated as the combustor temperature. When the flow is choked, the exit temperature is calculated using Equation 4.7.

It is also important to note that pressure will act quickly within the combustor, and temperature will have the effect of a delay based on the timescale found in Section 4.2. Pressure is distributed through the combustor using pressure waves which travel at the speed of sound. Temperature, however, is communicated through diffusion, conduction, convection, etc. The temperature "flowing" through the combustor will be mainly dictated by the convection, or fluid velocity, within the combustion chamber. The pressure, however, can be assumed within the model to be acting on the nozzle immediately.

4.4   Supersonic Flame Behavior

A supersonic flow downstream of a nozzle will have a defined structure at the nozzle exit based on gas dynamics, and can be seen in Figures 4.14 and 4.15. An overexpanded jet is observed when the pressure at the nozzle exit is less than the surrounding atmospheric pressure [2]. What results is a series of diamond patterns
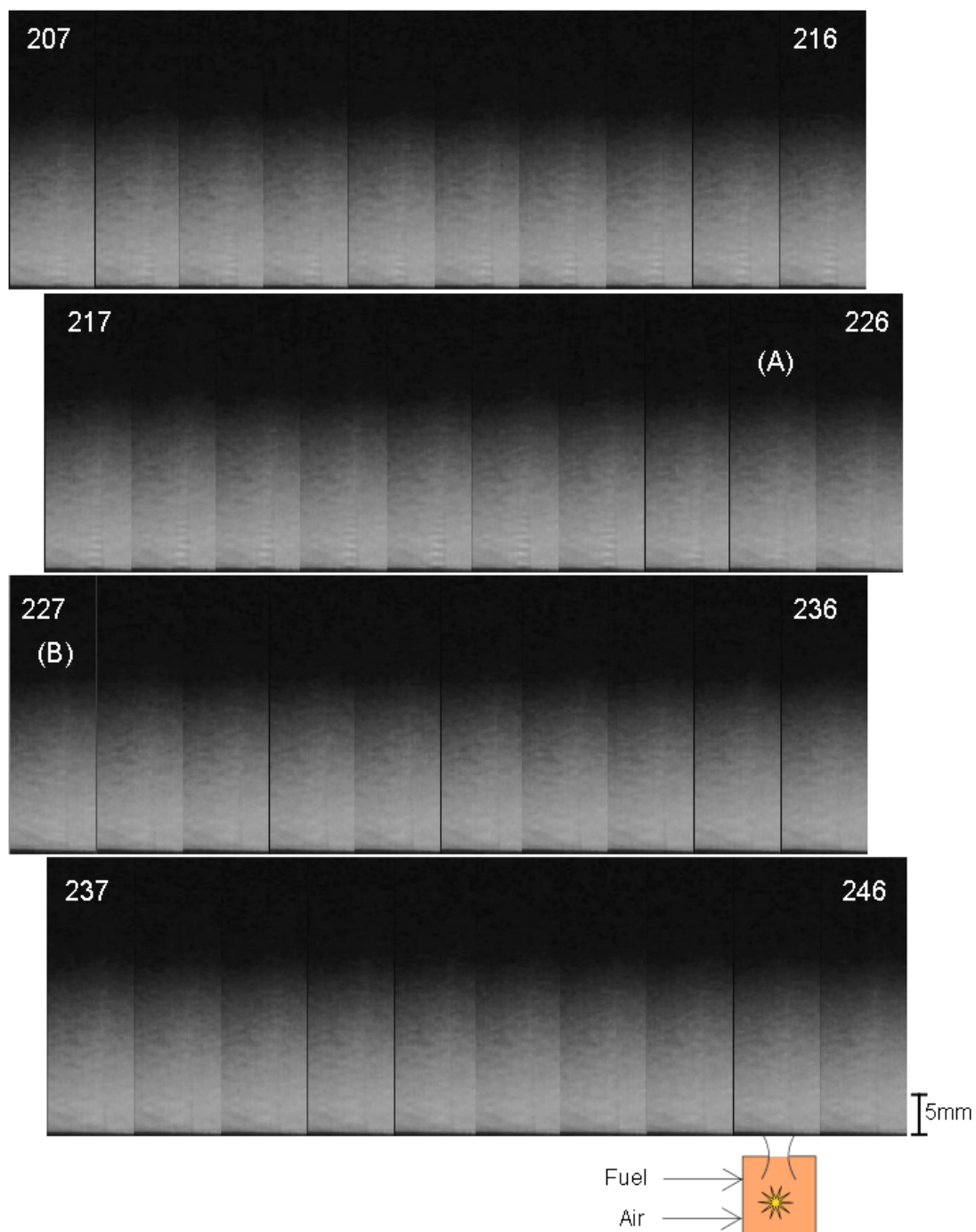
Fig. 4.14. Transient flame experiment captured by a high speed camera in conjunction with a schlieren system. (A) - Solenoid fully closed. (B) - Ignition.
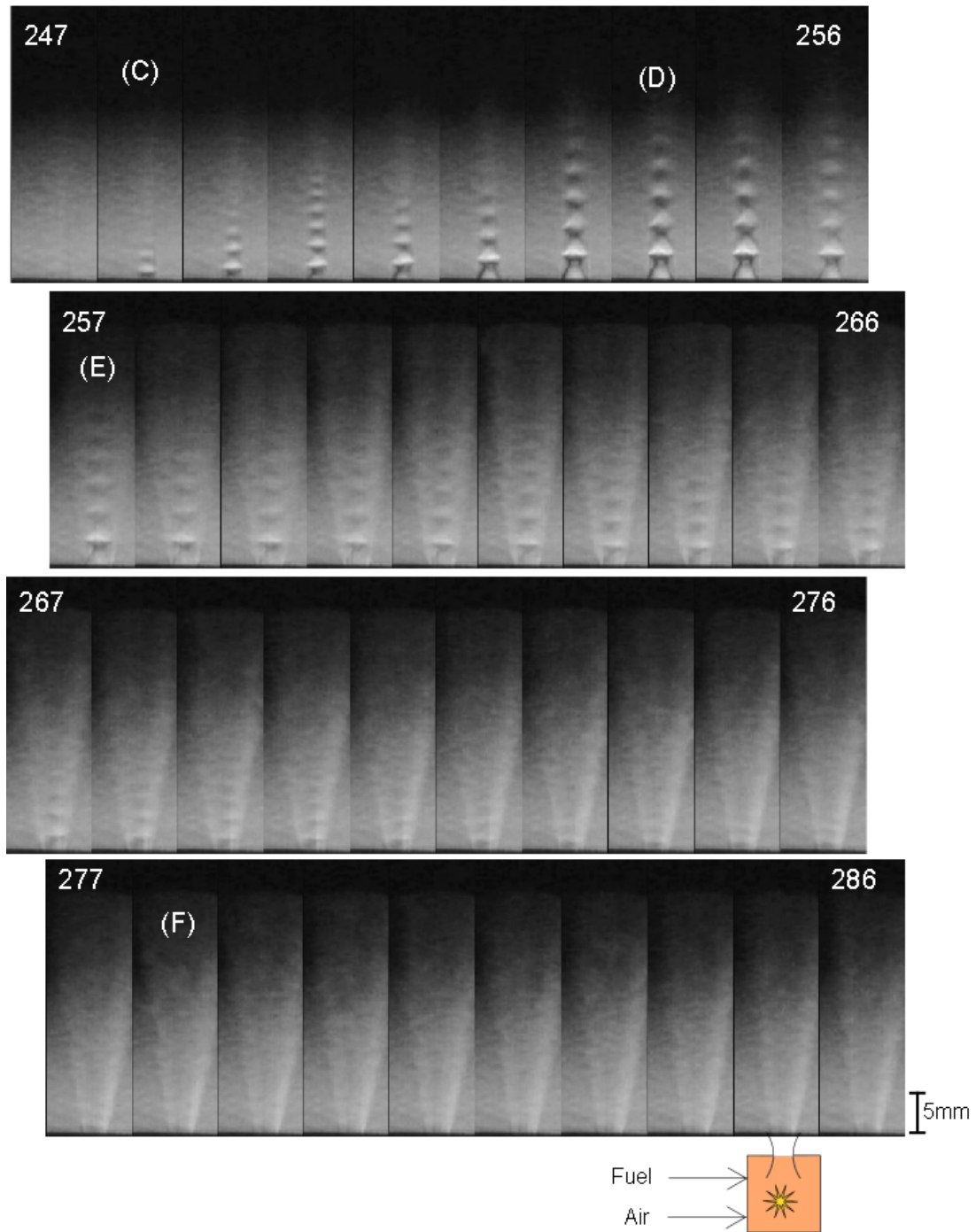
Fig. 4.15. Continued schlieren system imaging. (C) - Flame begins to emerge from nozzle. (D) - Most vigorous flame. (E) - Entrainment begins. (F) - Jet becomes subsonic.

caused by shock wave interactions in the flow. The shock waves form when the supersonic flow meets the free boundary of a quiescent flow. Because pressure across the boundary must be conserved, an oblique shock wave will form at the exit. These oblique shocks emanate from all points of the nozzle circumference, eventually meeting at the centerline of the flow. At this point they will reflect, hitting the free boundary. The new reflection will consist of expansion fans, which will behave in a similar fashion, continuing the diamond pattern until coalescing into oblique shocks once more. This pattern will continue until enough energy is lost and the flow becomes subsonic at all points [2]. An underexpanded jet will have a similar shockwave structure, only the process will begin with expansion fans, which will reflect into oblique shock waves. For this experiment, an inviscid, isentropic flow model is assumed.

Figures 4.14 and 4.15 detail the results of the schlieren experiment using the high speed CMOS camera. As discussed in Section 2.1, the CMOS camera frame rate is 1000 Hz, providing one frame per millisecond. The camera used does not possess the ability to be triggered. This complicates the analysis of the transient flame because there is no set starting point to the data. Therefore, the task of analyzing the data falls entirely on the interpretations of the experimenter. Through examination of the images, the following events were found. Prior to (A) in Figure 4.14, the flow is overexpanded, resulting in very small shockwave interactions. At (A), the solenoid is fully closed, allowing the nozzle to stop choking. Ignition occurs at (B), beginning the convection of the flame through the combustor. As described in Section 4.2, the flame will require a convective time to reach the nozzle. The flow remains subsonic through the nozzle until (C) in Figure 4.15. At (C) the flame is beginning to emerge from the combustor, and the nozzle is choked. (D) shows the most vigorous point of the flame, manifested as an underexpanded jet. At (E), the high speed, high temperature flow begins to entrain surrounding fluid, causing a "sheathing" effect

around the supersonic jet. Finally, at (F) the nozzle stops being choked, and resumes subsonic flow once more.

Points (A)-(F) are identified through the use of the ICCD, which is the only piece of equipment available for the experiment that can provide a link between the schlieren images and the timescales described in Figure 4.10. Because the ICCD is precisely timed, the delay time between ignition and flame emergence is known. This information can allow for a "time stamp" to be made on the schlieren images. It is known that the ignition point of the system occured 27 ms before the emergence of the flame. Therefore, the ignition point should be located in Figure 4.14, around point (B). It is also known that the solenoid, assuming a 25 ms closing time, should be closed around point (A).

The results computed through Cantera can also aid in correlating the schlieren image data. The frames of the schlieren images are numbered to represent the link between the simulation and the experiment, i.e. the simulated system is ignited a $t = 227$ ms reflected in the schlieren images at (B), frame 227. The modeled combustion system indicates that the flow will be choked until the solenoid is closed. Careful analysis of the schlieren frames reveal a shock wave pattern occurring at a much smaller scale prior to (A). This is clearly the result of a choked nozzle. This must correspond to the first region of choked flow from the solenoid orifice, as shown in Figure 4.6. Frames between (A) and (C) do not show any evidence of choking. This is because the solenoid valve has closed, and it is assumed fully closed by (A), as it is in the model. This gives very good agreement between the empirical data gathered by the schlieren system, and the qualitative simulation. The simulation predicts that the second choked region should last for approximately 25 ms. Examining Figure 4.15, the strong underexpanded jet and shock pattern can be observed from (C)-(F). This means the experimental choked region lasted for approximately 30 ms, whereas the simulation estimates a choked region of 25 ms. Qualitatively, the Cantera model of the transient pressure system applies well to the experiment.

The "sheathing" flow structure developed at (E) is the shear layer due to the entrainment of the surrounding flow. The transient jet beginning at (C) is occurring so fast that the entrainment of the surrounding flow cannot match the speed of the jet. When the jet is initially observed, there is little to no entrainment of surrounding fluid. However, when the high pressure jet emerges from the nozzle, there is an approximate 9 ms delay before the surrounding fluid becomes entrained. Past work, for example [47–49], indicates that transient, pulsed jets exhibit stronger entrainment than their steady state counterparts. Future work will examine this premise by eliminating ignition, and comparing the resulting shear layer development. The schlieren photographic evidence seems to suggest a suppression of entrainment from the ambient. In fact, reduced entrainment is an effect of compressibility in supersonic shear layers [50–52]. The compressibility and the associated strong waves lead to lower growth rates [52], which in turn signify lower entrainment.

Even more important than the compressibility effect is the presence of combustion for lowering entrainment. Turbulent jet flames exhibit a decrease in entrainment that has been well documented in numerous studies (e.g. [53,54]). For example, the study in reference [53] measured a reduction of up to 30% in the rate of entrainment due to the presence of burning. When compressibility and reaction are combined, as is the case in supersonic flames, the entrainment is expected to be further reduced, and the growth rate of the shear layer is severely impeded [55–57]. The present flame includes all three effects, and the synergy between them is difficult to predict.

Figure 4.16 demonstrates the best photo gathered by the newly constructed ICCD, with a comparison to one of the observed schlieren frames. The chemiluminescence of the flame is captured, and is amplified for ease of viewing. Several important facts can be taken from this image. The chemiluminescence of the flame is clearly visible, indicating a chemically reacting flow present downstream of the nozzle. Combustion occurs in the regions of subsonic flow within the jet. These areas are identified by their high photon generation rate. Additionally, the structure
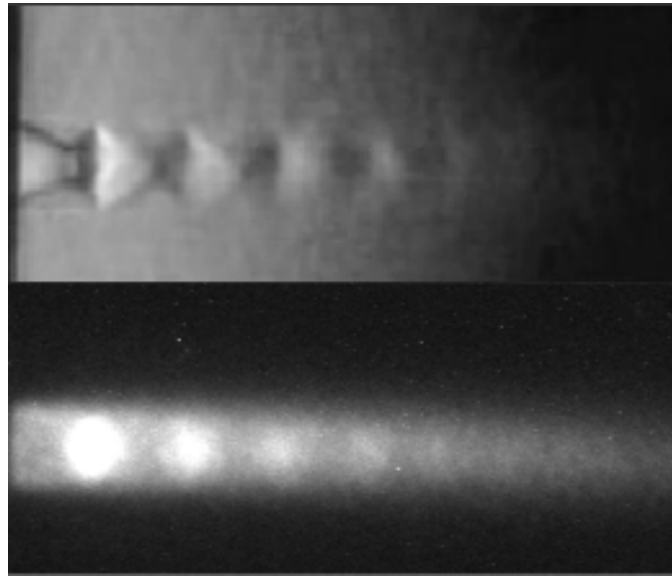
Fig. 4.16. Ideal intensified image of transient flame. Background noises are minimized, causing flow structure and chemiluminescence to be more easily observed. A direct comparison can be made between the length scales of the schlieren and intensified images.

of the jet is comparable to the gathered schlieren images. Although solid boundaries cannot be seen, the bright areas are comparable to the diamond patterns in Figure 4.15.

The ICCD was capable of determining the flame emergence from the nozzle. While the schlieren setup would only give information regarding the overall density gradients of the flow, chemiluminescence of the flame can be observed with the ICCD. This means that even if there is a supersonic shock wave structure, it may not necessarily be a flame. Because the ICCD is a triggered (gated) system, it can be used to identify the flame emergence, and track its progress in space. This was useful in comparing the model results to the experiment, as relations between distance and time in Section 4.2 were made based on the timescales observed in the experiment. The transient flame itself suffers from reproducibility based on the initial conditions in the combustor, and the timing variations of the mechanical components used in

the experiment. However, averaged data from multiple photos can be used to specify the timing of the flame.

4.5   Summary

In this thesis, an experiment was designed and constructed to produce a transient, supersonic methane/air flame. The transient effect was produced using an electromagnetic solenoid to pulse air into the combustor. Various experimental timescales were discussed. To image the emerging flame front, a newly designed ICCD was constructed. The creation of the ICCD necessitated the construction of a high voltage power supply, and an optical relay system to couple the image intensifier to a CCD. Additionally, a z-type schlieren system was constructed to gather high speed video information of the transient flame. The thermodynamic properties of the system were quantified computationally using Cantera. Pressure, temperature, and chemical composition were discussed as they evolved with time through the combustor. The results showed good agreement between observed experimental data and the computational model. A comparison was made between the schlieren data from the experiment and the computational model. Finally, ICCD imaging was used to observe the chemiluminescence of the flame, and to help tie the timescales of the experiment to the simulated model.

4.6   Future Work

Immediate work will focus on analyzing changes to the combustion process through variance of initial conditions. Further research on modifying the timescales of the experiment will be completed by adjusting the open solenoid time and ignition point of the system. The results obtained from this will increase the understanding of how the equivalence ratio in the combustion chamber is affected by different timescales. Furthermore, there is insufficient data to fully explain the significance of the area

ratios A1 and A2 from Figure 2.1. Multiple tests can be constructed to explain this problem. Two immediate experiments will focus on changing the area ratio, and changing the distance between A2 and the ignition point. By changing the position of A2, understanding the limits of recirculation in the chamber can be achieved. Experiments using an underexpanded nozzle will also be performed. By changing the nozzle dimensions, an underexpanded jet can be created, changing the pressure and temperature profiles. Additionally, the flow structure will change significantly. The simulated model can also be improved through the addition of heat loss effects. By adding heat loss to the system, a more complete and accurate description of the transient flame event can be considered. Lastly, immediate work will include joining the high speed CMOS camera to the image intensifier relay. As of now, the CCD may prove insufficient for analyzing the time dependent properties of the flow. By increasing the overall system gain with the image intensifier, higher quality schlieren videos can be obtained.

Long term future work will include laser diagnostics, and building multiple combustor units for jet interaction. Planar laser induced fluorescence (PLIF) can provide quantifiable measurements of the flame constituents. As of now, relying on the computed chemistry data alone is insufficient for truly understanding the transient flame. PLIF can provide the detailed flame chemistry, allowing for further comparison of the experiment to the simulation. Additionally, the ultimate goal is to produce a system which forces the interaction of the supersonic jets. This will require the construction of several transient combustors for use in synchronization. The overall assembly of the experiment will require accurate timing, further complicating system parameters.

REFERENCES

[1] Fry, R., "A Century of Ramjet Propulsion Technology Evolution," *Journal of Propulsion and Power*, Vol. 20, No. 1, 2004, pp. 27–58.

[2] Anderson, J., *Modern Compressible Flow*, 3rd ed., McGraw-Hill, 1982, pp. 120–145.

[3] Kloesel, K. J., Ratnayake, N. A., and Clark, C. M., "A Technology Pathway for Airbreathing, Combined-Cycle, Horizontal Space Launch Through SR-71 Based Trajectory Modeling," 17th AIAA International Space Planes and Hypersonic Systems and Technologies Conference, San Francisco, CA, AIAA Paper 2011-2229, Apr. 2011.

[4] Roy, G., Frolov, S., Borisov, A., and Netzer, D., "Pulse Detonation Propulsion: Challenges, Current Status, and Future Perspective," *Progress in Energy and Combustion Science*, Vol. 30, May 2004, pp. 545–672.

[5] Yan, Y., Fan, W., Wang, K., Zhu, X., and Mu, Y., "Experimental Investigations on Pulse Detonation Rocket Engine with Various Injectors and Nozzles," *Acta Astronautica*, Vol. 69, 2011, pp. 39–47.

[6] Milton, B. and Pianthong, K., "Pulsed, Supersonic Fuel Jets – A Review of Their Characteristics and Potential for Fuel Injection," *International Journal of Heat and Fluid Flow*, Vol. 26, 2005, pp. 656–671.

[7] Zakrzewski, S., Milton, B., Pianthong, K., and Behnia, M., "Supersonic Liquid Fuel Jets Injected into Quiescent Air," *International Journal of Heat and Fluid Flow*, Vol. 25, 2004, pp. 833–840.

[8] Cutler, A., "High-Frequency Pulsed Combustion Actuator Experiments," *AIAA Journal*, Vol. 49, No. 9, Sept. 2011.

[9] Giuliani, F., Lang, A., Gradl, K., Siebenhofer, P., and Fritzer, J., "Air Flow Modulation for Refined Control of the Combustion Dynamics Using a Novel Actuator," *Journal of Engineering for Gas Turbines and Power*, Vol. 134, Feb. 2012.

[10] Gilarranz, J., Traub, L., and Rediniotis, O., "A New Class of Synthetic Jet Actuators – Part I: Design, Fabrication and Bench Top Characterization," *Journal of Fluids Engineering*, Vol. 127, Mar. 2005, pp. 367–376.

[11] Lefebvre, A., Ibrahim, A., and Benson, N., "Factors Affecting Fresh Mixture Entrainment in Bluff-Body Stabilized Flames," *Combustion and Flame*, Vol. 10, 1966, pp. 231–239.

[12] Longwell, J., Frost, E., and Weiss, M., "Flame Stability in Bluff Body Recirculation Zones," *Industrial & Engineering Chemistry*, Vol. 45, No. 8, 1953, pp. 1629–1633.

[13] Edelman, R. and Harsha, P., "Laminar and Turbulent Gas Dynamics in Combustors - Current Status," *Progress in Energy and Combustion Science*, Vol. 4, 1978, pp. 1–62.

[14] Sutton, G. and Biblarz, O., *Rocket Propulsion Elements*, 8th ed., John Wiley & Sons, New Jersey, 2010, pp. 57–63.

[15] Hill, P. and Peterson, C., *Mechanics and Thermodynamics of Propulsion*, 2nd ed., Addison-Wesley Publishing Company, 1992.

[16] Ehn, A., Johansson, O., Bood, J., Arvidsson, A., Li, B., and Alden, M., "Fluorescence Lifetime Imaging in a Flame," *Proceedings of the Combustion Institute*, Vol. 33, 2011, pp. 807–813.

[17] Dam, N., Rodenburg, M., Tolboom, R., Stoffels, G., Huisman-Kleinherenbrink, P., and ter Meulen, J., "Imaging of an Underexpanded Nozzle Flow by UV Laser Rayleigh Scattering," *Experiments in Fluids*, Vol. 24, 1998, pp. 93–101.

[18] Docquier, N., Belhalfaoui, S., Lacas, F., and Darabiha, N., "Experimental and Numerical Study of Chemiluminescence in Methane/Air High-Pressure Flames for Active Control Applications," *Proceedings of the Combustion Institute*, Vol. 28, 2000, pp. 1765–1774.

[19] Ikeda, Y., Kojima, J., and Hashimoto, H., "Local Chemiluminescence Spectra Measurements in a High-Pressure Laminar Methane/Air Premixed Flame," *Proceedings of the Combustion Institute*, Vol. 29, 2002, pp. 1495–1501.

[20] Katanoda, H., Miyazato, Y., Masuda, M., and Matsuo, K., "Pitot Pressures of Correctly-Expanded and Underexpanded Free Jets from Axisymmetric Supersonic Nozzles," *Shock Waves*, Vol. 10, 2000, pp. 95–101.

[21] Tabei, K., Shirai, H., and Takakusagi, F., "Density Measurements of Underexpanded Free Jets of Air from Circular and Square Nozzles by Means of Moiré-Schlieren Method," *JSME International Journal*, Vol. 35, No. 2, 1992.

[22] Tkacik, P., Keanini, R., Srivastava, N., and Tkacik, M., "Color Schlieren Imaging of High-Pressure Overexpanded Planar Nozzle Flow Using a Simple, Low-Cost Test Apparatus," *Journal of Visualization*, Vol. 14, No. 1, 2011, pp. 11–14.

[23] Settles, G., *Schlieren and Shadowgraph Techniques*, Springer-Verlag, New York, 2001.

[24] Nasuti, F. and Onofri, M., "Shock Structure in Separated Nozzle Flows," *Shock Waves*, Vol. 19, 2009, pp. 229–237.

[25] Bayeh, A. and Karpetis, A., "Miniaturized Combustor for Methane-Air Afterburner," *Journal of Propulsion and Power*, Feb. 2012, Submitted.

[26] Texas A&M University, Aerospace Engineering, "Transient Flames," August 2010, [http://www.youtube.com/watch?v=chxdYtRqTOM. Accessed 08/25/10.]

[27] Glassman, I., *Combustion*, 4th ed., Academic Press, 2008, pp. 240–250.

[28] Van den Schoor, F., Hermanns, R., van Oijen, J., Verplaetsen, F., and de Goey, L., "Comparison and Evaluation of Methods for the Determination of Flammability Limits, Applied to Methane/Hydrogen/Air Mixtures," *Journal of Hazardous Materials*, Vol. 150, 2008, pp. 573–581.

[29] Favaloro, M., "Ablative Materials," *Kirk-Othmer Encyclopedia of Chemical Technology*, 2000.

[30] Mishra, C. and Yoav, P., "Incompressible and Compressible Flows Through Rectangular Microorifices Entrenched in Silicon Microchannels," *Journal of Microelectromechanical Systems*, Vol. 14, No. 5, Oct. 2005, pp. 1000–1012.

[31] Kee, R., *Chemically Reacting Flow: Thoery and Practice*, 1st ed., John Wiley & Sons, 2003, pp. 649–683.

[32] Goodwin, D., "An Open-Source, Extensible Software Suite for CVD Process Simulation," *Proceedings of CVD XVI*, 2003, pp. 155–162, [http://code.google.com/p/cantera/. Accessed 01/15/11.].

[33] Smith, G., Golden, D., Frenklach, M., Moriarty, N., Eiteneer, B., Goldenberg, C., Bowman, T., Hanson, R., Song, S., Gardiner, W., Lissianski, V., and Qin, Z., "GRI-Mech Source," [http://www.me.berkeley.edu/gri_mech/. Accessed 01/15/11.]

[34] van Rossum, G., "Python Programming Language - Official Website," [http://www.python.org/. Accessed 01/15/11.]

[35] Bergthorson, J. and Dimotakis, P., "Premixed Laminar C1-C2 Stagnation Flames: Experiments and Simulations with Detailed Thermochemistry Models," *Proceedings of the Combustion Institute*, Vol. 31, 2007, pp. 1139–1147.

[36] Odedra, A. and Malalasekera, W., "Eularian Particle Flamelet Modeling of a Bluff-Body CH4/H2 Flame," *Combustion and Flame*, Vol. 151, Aug. 2007, pp. 512–531.

[37] Hamamatsu Photonics, Iwata City, Japan, *Image Intensifiers*, Sept. 2009.

[38] Eckbreth, A., *Laser Diagnostics for Combustion Temperature and Species*, 2nd ed., Gordon and Breach Publishers, 1996.

[39] Navon, D., *Semiconductor Microdevices and Materials*, CBS College Publishing, 1986, pp. 387–397.

[40] Longmire, M., "SBIG Software - CCDOPS," [http://www.sbig.com/Software.html. Accessed 10/15/11.]

[41] Santa Barbara Instruments Group, Santa Barbara, California, *CCD Camera Operating Manual for the Model ST-4x, ST-5, and ST-6*, Jan. 1996, Revision 2A.

[42] Markerink, W., "Camera Mounts & Registers," [http://www.markerink.org/WJM/HTML/mounts.htm. Accessed 11/15/11.]

[43] Hiller, B., Paul, P., and Hanson, R., "Image-Intensified Photodiaode Array as a Fluorescence Detector in CW-Laser Experiments," *Review of Scientific Instruments*, Vol. 61, No. 7, July 1990, pp. 1808–1815.

[44] Welford, W., *Useful Optics*, 1st ed., The University of Chicago Press, 1991.

[45] Zare-Behtash, H., Kontis, K., Gongora-Orozco, N., and Takayama, K., "Compressible Vortex Loops: Effect of Nozzle Geometry," *International Journal of Heat and Fluid Flow*, Vol. 30, 2009, pp. 561–576.

[46] White, F., *Viscous Fluid Flow*, 3rd ed., McGraw-Hill, 2006.

[47] Platzer, M., Simmons, J., and Bremhorst, K., "Entrainment Characteristics of Unsteady Subsonic Jets," *AIAA Journal*, Vol. 16, No. 3, 1977, pp. 282–284.

[48] Bremhorst, K. and Harch, W., "The Mechanism of Jet Entrainment," *AIAA Journal*, Vol. 16, No. 10, 1978, pp. 1104–1106.

[49] Vermeulen, P., Ramesh, V., and Yu, W., "Measurements of Entrainment by Acoustically Pulsed Axisymmetric Air Jets," *ASME Journal*, Vol. 108, July 1986, pp. 479–484.

[50] Papamoschou, D. and Roshko, A., "The Compressible Turbulent Shear Layer: An Experimental Study," *Journal of Fluid Mechanics*, Vol. 197, 1988, pp. 453–477.

[51] Samimy, M., Reeder, M., and Elliott, G., "Compressibility Effects on Large Structures in Free Shear Flows," *Physics of Fluids*, Vol. 4, No. 6, 1992, pp. 1251–1258.

[52] Elliot, G. and Samimy, M., "Compressibility Effects in Free Shear Layers," *Physics of Fluids*, Vol. 2, No. 7, July 1990, pp. 1231–1240.

[53] Ricou, F. and Spalding, D., "Measurements of Entrainment by Axisymmetrical Turbulent Jets," *Journal of Fluid Mechanics*, Vol. 11, 1961, pp. 21–32.

[54] Tacina, K. and Dahm, W., "Effects of Heat Release on Turbulent Shear Flows. Part 1. A General Equivalence Principle for Non-Buoyant Flows and its Application to Turbulent Jet Flames," *Journal of Fluid Mechanics*, Vol. 415, 2000, pp. 23–44.

[55] Huh, H. and Driscoll, J., "Shock-Wave-Enhancement of the Mixing and the Stability Limits of Supersonic Hydrogen-Air Jet Flames," *Twenty-Sixth Symposium (International) on Combustion*, 1996, pp. 2933–2939.

[56] Driscoll, J., Huh, H., Yoon, Y., and Donbar, J., "Measured Lengths of Supersonic Hydrogen-Air Jet Flames – Compared to Subsonic Flame Lengths – and Analysis," *Combustion and Flame*, Vol. 107, 1996, pp. 176–186.

[57] Miller, M., Bowman, C., and Mungal, M., "An Experimental Investigation of the Effects of Compressibility on a Turbulent Reacting Mixing Layer," *Journal of Fluid Mechanics*, Vol. 356, 1998, pp. 25–64.

A Theoretical and Numerical Study on a Shock Wave Interacting with a 2-D Discontinuous Area Enlargement

Nomenclature

a	=	speed of sound, $\sqrt{\gamma RT}$
A	=	duct area (duct height times unit depth)
A_2/A_1	=	ratio of large duct height to small duct height, degree of area change
c_P	=	specific heat at constant pressure
D	=	function of Mach Number only, defined by Eq. (5)
h	=	sensible enthalpy, $c_P T$
M	=	flow Mach Number, u/a
M_S	=	incident shock strength
M_{SS}	=	secondary shock strength
M_{TS}	=	transmitted shock strength
P	=	pressure
P_R, Q_R	=	right and left Riemann invariants, respectively
R	=	gas constant for air
T	=	temperature
u	=	velocity (1D)
γ	=	specific heat ratio (air)
ρ	=	density

I. Introduction

SCRAMJETS have been extensively studied since the 1950's due to the to highly complex nature of the flows, short flow residency times, difficulties in mixing fuel and oxidizer in the combustion chamber, airframe integration issues, and high heat transfer rates. One major drawback of scramjet engines is the need to accelerate the vehicle to supersonic velocities to provide the scramjet inlet with a sufficient amount of high-kinetic energy air. To overcome this difficulty, two major approaches have been developed, with many more still under research. Usually, a second engine is employed to accelerate the vehicle: if this is done with a rocket, it is called a Rocket-Based Combined Cycle (RBCC) system; if done with a turbine engine, a Turbine-Based Combined Cycle (TBCC) system. However, carrying two entire propulsion systems onboard for the entire flight results in increases in the vehicle size and weight, increases in the complexity and number of failure points, a reduction of the payload capacity, and ultimately increases in the vehicle cost.

One approach to accelerating the scramjet is the transient inlet concept (TIC) shown in Fig. 1. In this method, a scramjet inlet is outfitted with small injector ducts that inject either shock or detonation waves into the main engine flowpath. Executed in a rapidly pulsing manner similar to that of a Pulsed Detonation Engine (PDE), these waves serve to accelerate the flow behind them, potentially inducing flow into the engine inlet. However, there are many scientific and technical challenges associated with assessing the feasibility of this concept, such as unsteady shock wave motion in ducts, shock-shock interactions, shock-induced free shear layers, mixing enhancement, and many
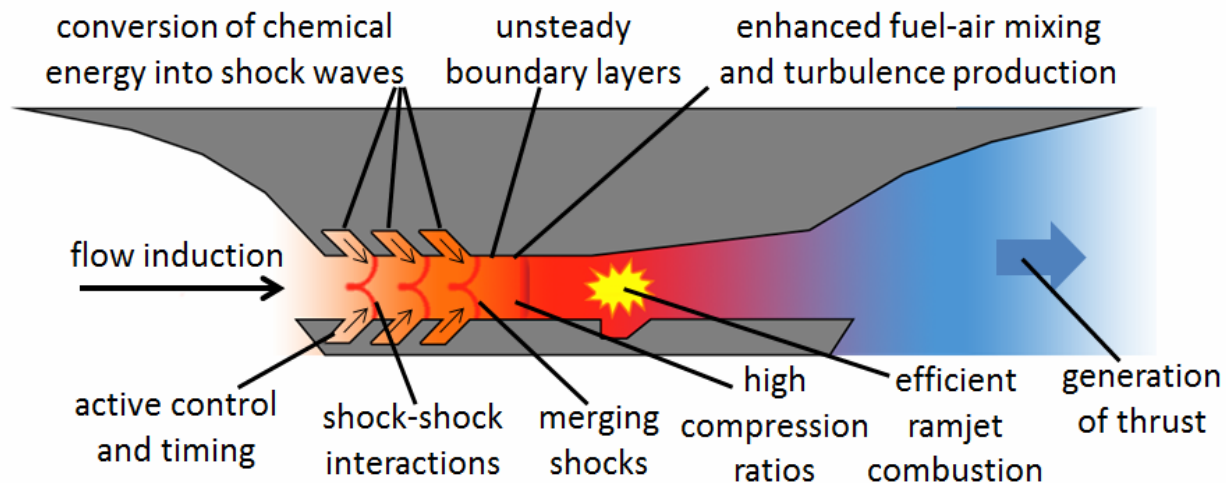

Figure 1. Motivation concept. *Transient Inlet Concept was conceived by R. Bowersox and R. Jeffries (AFOSR)*

more (see Fig. 1). This study will address the first: unsteady shock wave motion in ducts.

II. Background

Unsteady shock wave motion through ducts has been extensively studied due to the wide variety of potential applications, such as hazardous explosions in underground tunnels, gas transmission pipes, exhaust systems of internal combustion engines and blast shelter design. These complicated flow fields are rich in a large variety of fundamental fluid dynamic phenomena, i.e. shock wave reflections, shock-shock interactions, shock-vortex interactions, etc. Combined with the relatively simple geometries, these flows are excellent testbeds for improving our understanding of fluid dynamics.

Historically, these studies fall into several categories: shock waves in turning ducts[1-6], shock waves turning corners[7-11], shock waves in branching ducts[12-17], shock waves in ducts with baffles/obstacles[18-26], shock wave focusing[27-34], and shock waves in ducts of varying cross-sections (the present paper will only consider changes in geometry). An excellent comprehensive review of these topics can be found in Ref. 35. Since the original works done by Chester[36,37], Chisnell[38], and Whitham[39-41], shock wave motion through ducts of varying cross-sectional area has been treated by numerous researchers. A few studies[42-48] treat a wide variety of geometry changes both mathematically and experimentally, including curved and straight ducts, "stairways", and even airfoils. Some[49,50] specialize in area changes that converge then diverge, akin to nozzle flows. These geometries can be classified according to two features: continuous (smooth, gradual) or discontinuous (sudden, abrupt), and an area enlargement or area reduction.

Much of the past work has focused on continuous area changes, since there are several theoretical methods (Chester-Chisnell-Whitham theory[36-41], Skews theory[8], shock dynamics {ray-shock theory}[51], Rudinger's theory[52], Method of Characteristics) available to analyze them and several quasi-1D numerical methods (Second-order Hydrodynamic Automatic Mesh Refinement Code[53], Generalized Riemann Problem codes[54], Random Choice Method codes[55]) available to solve them. These geometries usually involve a gradual area change manifested by an area change *segment* characterized by its length to height ratio. Generally speaking, the smaller the divergence angle and the longer the area change segment, the closer the experimental and numerical results are to the theoretical results. Several studies have examined unsteady shock waves interacting with both continuous area enlargements and reductions[55,56], only area enlargements[57,58], and only area reductions[59-62]. In particular, pseudo-steady and unsteady shock wave reflections from a smoothly converging (inclined) wall have received much attention. For a recent comprehensive report of the work done on these flows, see Ref. 63.

This report focuses on discontinuous area changes because these are the types of interactions seen in the transient inlet concept. The past work in this subfield covers both discontinuous area enlargements and reductions[64,65], only area reductions[66-69], and area enlargements. In the case of discontinuous area reductions, there exists a bifurcation in the potential flow patterns, where one of three possibilities exists. Thus, the studies in this area focus on analyzing this peculiarity. However, this does not exist for discontinuous area enlargements, where the flow pattern is deterministic. These flows can be further sorted according to the number of degrees of freedom of the geometry: axisymmetric (cylindrical) and rectangular. There are a few studies that consider both axisymmetric and rectangular discontinuous area enlargements[70-73]. Axisymmetric geometries are prevalent in the literature[74-79], since the easiest case is the shock wave exiting the open end of a shock tube[80-84]. These flows usually have a spherically expanding shock wave followed by a vortex ring. Since scramjet ducts are often rectangular, this study considers an asymmetric rectangular geometry (backwards-facing step). As such, the most relevant works are those regarding discontinuous rectangular area enlargements, such as those found in Ref. 85-98. These include geometries ranging from true backwards-facing steps to expansion chambers, open square-shaped and diamond-shaped ends of shock
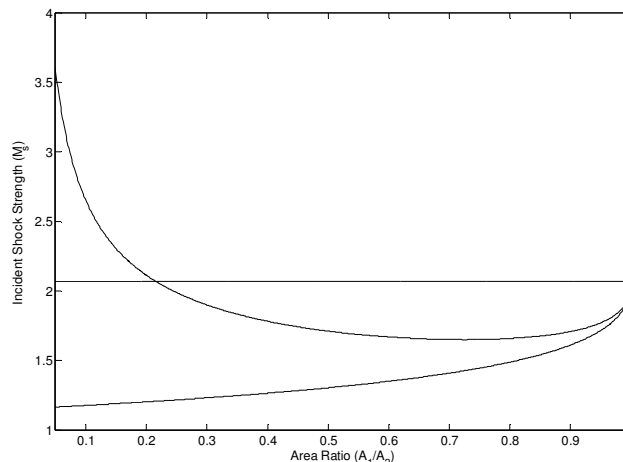

Figure 2. Existing body of work shown in parameter space.

tubes, and adjoining square cavities. These works qualitatively and quantitatively comment on the diffracting shock shape, corner vortex location, shock-vortex interactions, and secondary shock structures. [WILL ELABORATE MORE HERE] However, the majority of these studies are numerical and experimental, with very limited theoretical treatment of these flows. Second, additional flow features are illuminated in this work that were not covered previously. Third, the cases studied thus far are sporadic and spot the parameter space; whereas this is the first true parametric study of these flows. This paper will compare theoretical and numerical results, and identify the time-accurate primary and secondary flow structures present in these flows.

III. Methodology

All of the simulations and calculations performed herein assume inviscid compressible flows in air. The range of incident shock strengths studied was *1 < M$_S$ < 3* over area ratios *1.1 ≤ A$_2$/A$_1$ ≤ 2.0*. Limiting the incident shock strength to these values covers all possible wave diagrams for these flows while simplifying the gas dynamics. At the upper limit ($M_S = 3$), the temperature behind the incident shock (~800K) is not sufficient to cause noticeable real gas effects, such as ioization, dissociation, or chemical reactions. Thus, for these studies the thermally perfect equation of state will be used (as well as the calorically perfect equation of state). In addition, since the appropriate time scales (~1ms) are too short for a significant amount of heat transfer, the flows are reasonably assumed to be adiabatic and non-conducting. The range of area ratios was chosen to provide scenarios that would range from only a small perturbation from theory up to a matching of channel heights between the main engine duct and the shock injector duct.

A. Theoretical

In addition to the above assumptions, the theoretical treatment of the problem also assumes a "steady state". Though the primary difficulty of this problem is its transient nature, if one were to wait a sufficiently long enough time such that all transient phenomena due to the area change interaction were to subside and all major wave strengths were no longer being modified, then the wave system could be said to have approached a "steady state". This also means that the primary waves (shocks, expansions) travel with a constant velocity in an inviscid flow and uniform flow regions separate the primary waves. Furthermore, the theory will assume quasi-1D flow, which is consistent with modern approaches to these problems. Following the algorithm presented in Rudinger 1955[52], these assumptions simplify the Euler equations to:

Conservation of Mass (COM):

$$\rho_L u_L A_L = \rho_R u_R A_R \tag{1}$$

Conservation of Energy (COE):

$$h_1 + \frac{u_1^2}{2} = h_2 + \frac{u_2^2}{2} = h_0 \tag{2}$$

Both conservation laws hold across the area change, assuming the flow expands isentropically through the area change (i.e. no flow separation or standing shocks). Subscripts *L* and *R* denote the left and right sides of the area change respectively. By substituting the isentropic definition of the stagnation enthalpy combined with COE (Eq. (2))

$$\frac{\rho_0}{\rho_L} = (1 + \frac{\gamma-1}{2} M_L^2)^{1/(\gamma-1)} \tag{3}$$

Into Eq. (1) for both ρ_L and ρ_R (and similarly for T_L and T_R), and using the definitions of the Mach Number and sound speed, one obtains an isentropic statement of COM as a function only of *M*, that is $A_2/A_1 = f(M_L, M_R)$

$$\frac{A_2}{A_1} = \frac{M_1 \left(1 + \frac{\gamma-1}{2} M_2^2\right)^{\frac{\gamma+1}{2(\gamma-1)}}}{M_2 \left(1 + \frac{\gamma-1}{2} M_1^2\right)^{\frac{\gamma+1}{2(\gamma-1)}}} \tag{4}$$

Which can be rewritten as $A_L D_L = A_R D_R$, where

$$D = \frac{M}{\left(1 + \frac{\gamma-1}{2} M^2\right)^{\frac{\gamma+1}{2(\gamma-1)}}} \tag{5}$$

This function of Mach Number only has two branches: a subsonic branch where D increases with increasing M up to a maximum, and a supersonic branch where D decreases with increasing M. Now manipulate COE (Eq. (2)) by substituting in the definitions of c_P and a, which yields

$$\frac{a_1^2}{\gamma-1} + \frac{u_1^2}{2} = \frac{a_2^2}{\gamma-1} + \frac{u_2^2}{2} \tag{6}$$

Or

$$a_1^2 \left(1 + \frac{\gamma-1}{2} M_1^2\right) = a_2^2 \left(1 + \frac{\gamma-1}{2} M_2^2\right) \tag{7}$$

Eqs. (6) and (7) along with Eq. (4) are the forms of the conservation laws that will be used in this algorithm. Finally, since centered expansion waves are present, the opposite Riemann invariants hold across them:
For left-running (Q) waves

$$P_R = \frac{2a}{\gamma-1} + u = const \tag{8}$$

For right-running (P) waves

$$Q_R = \frac{2a}{\gamma-1} - u = const \tag{9}$$

Now that a useful form of the conservation laws has been obtained, one can apply these governing equations to the problem at hand. Rudinger 1955[52] presents five possible wave patterns that could be seen in the given parameter space (M_S, A_2/A_1), illustrated in Fig. 3 below (cases 1-5). It was later discovered that a sixth possible case exists, shown in Fig. 3. From this analysis, three primary waves appear: the transmitted shock that propagates into the large duct, an expansion reflected upstream into the small duct, and a secondary left-facing shock wave somewhere in the large duct.

Cases 1, 2, 3, and 6 all have a left-running centered expansion reflected back into the small duct because the flow behind the incident shock wave was subsonic, i.e. $M_S < 2.068$ (the value of the incident shock strength in air that produces a sonic piston velocity behind it). Cases 4 and 5 exist for $M_S < 2.068$. Looking at Fig. 4a), the area underneath curve a) represents flows with case 1 pattern. This pattern has a reflected expansion, but the flow remains subsonic everywhere. The expansion serves to accelerate the flow as if through a converging nozzle.
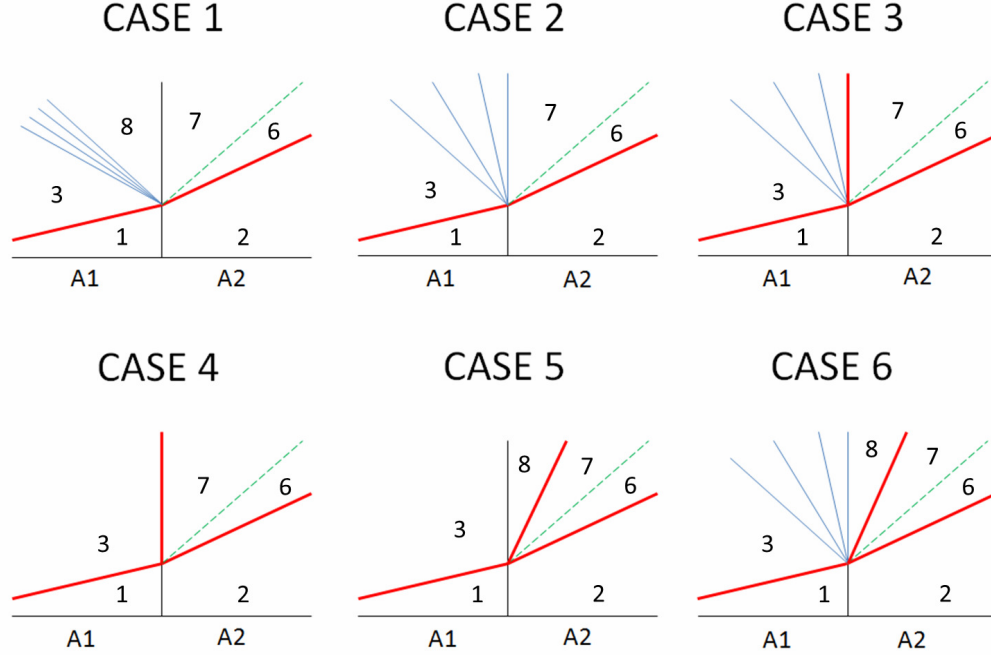
Figure 3. Wave (x-t) diagrams of six possible flow patterns. *The vertical line denotes the discontinuous area change dividing the small duct (on its left) from the large duct (on its right). Shock waves are in red, expansions in blue, and contact surfaces in green.*

Case 1 exhibits a strong asymptotic behavior as it approaches case 2. This creates substantial numerical difficulty in modeling incident shock strengths close to this value. Increasingly smaller increments of M_S are needed to resolve points in the case 1 region close to the case 2 line, as the flow exiting the small duct asymptotically reaches a sonic velocity. Case 2 is the solution for which the flow is expanded to a sonic ($M_8 \to 1$) velocity at the "throat" (area change) but still expands subsonically (isentropically) through the area change. The curve a) in Fig. 4a) represents all flows with a case 2 wave pattern. The tail of the reflected expansion stands at the area change. Note that curve a) asymptotes on the left to Ms ~ 1.154.

The area between curves a) and b) represents case 3. The tail of the reflected expansion has reached sonic velocity, but the pressure ratio across the "nozzle" is such that the flow can no longer decelerate isentropically. Thus a secondary standing shock is formed at the area discontinuity. If one were to assume a continuous area change, then the shock would be standing somewhere in the diverging section. This shock is facing left, against the expanding flow entering the area change from the left, raising the pressure to that behind the transmitted shock. Case 4 solutions are to the left and beneath curve b), but above the $M_S < 2.068$ line. This indicates that there is no reflected expansion, because waves cannot travel upstream in supersonic flow. This flow pattern is identical to that of case 3, but without the reflected expansion.

The region above curve b) but below the $M_S < 2.068$ line is case 6. This is the case not mentioned in Rudinger 1955[52], but is discussed in Salas 1991[65]. The reflected expansion is present, but the velocity of the expanding flow is sufficient to overwhelm the secondary standing shock and push it to the right. Thus, there are two shocks moving to the right in this case – the transmitted shock propagating right and the backward-facing secondary shock being pushed right by the flow. The open region above both curve b) and the $M_S < 2.068$ line is case 5. The incident shock is strong enough to both produce supersonic flow behind it as well as push the secondary shock out of the area change and downstream.

Knowing the conservation laws and the wave patterns, a computer code was developed to solve these flow fields. All algorithms involved guessing on a flow variable, proceeding with calculations over the entire flow field, and matching both the pressure and velocity across the transmitted shock (which must always exist). If the two do not yield the same strength of the transmitted shock, the guess is updated via a simple bisection method until the solution converges (usually to a tolerance of 0.001 on velocity). The solution usually converged in 12 iterations or less. Some useful notes on the algorithms used:

- For each case, the flow variable iterated on was: case 1 – the sound speed following the reflected expansion (a_8), case 2 – the incident shock strength (M_S), cases 3-6 – the transmitted shock strength (M_{TS}).
- When using COM (Eq. (4)) across the area change, one must always go from the smaller duct to the larger duct. Otherwise, the value for D (see Eq. (5)) will exceed its maximum value, and the solution will not be found.
- Use moving normal shock jump conditions across both the incident and transmitted shocks.
- Total enthalpy is not conserved (across all moving waves), except across the area change (when a standing shock is not present).
- When jumping across a rarefaction wave, use the isentropic relations to find the pressures, *not* COE.
- The algorithm for the cases with a stationary shock (3 and 4) is taken from <u>Modern Compressible Flow</u>[99] (example 5.7). Note that this portion does *not* use Eq. (4).
- The secondary moving shock in cases 5 and 6 is a *left-facing* shock wave, but it is pushed right by the expanded flow (due to the area change). The calculations find the velocity with which the shock is moving to the left using a temporary change in reference frame.

The theoretical algorithm is not physically limited to this parameter space; however, the foundational theory breaks down above $M_S \sim 4$, producing inaccurate results. The algorithm also works for any area ratio ($A_2/A_1 > 1$), but rather the scope of this report is the limiting factor.

B. Theoretical Verification

In order to deem the theoretical results produced by this solution algorithm as reliable, the code must be verified against the literature. Salas 1991[65] analyzed discontinuous area enlargements and area contractions, focusing on a bifurcation in the latter. They used a similar inviscid "steady state" algorithm and provided selected results for each case, as well as a detailed mapping of the cases to the parameter space.

The comparison between their results and the current results for the Mach Number in various flow regions for the selected cases are tabulated below:

Table 1. Comparison between Salas 1991[65] And Current Results for Selected Cases.

Case	A_2/A_1	M_s	M_3	M_8	M_7	M_6
1	0.5 (2)	1.1	0.154	0.222	0.109	0.109
			0.15416	0.22205	0.10857	0.10858
2	0.5 (2)	1.303	0.409	-	0.306	0.307
			0.40851	-	0.3059	0.30645
3	0.5 (2)	1.5	0.609	-	0.427	0.447
			0.60429	-	0.42656	0.44688
6	0.5 (2)	1.85	0.871	2.197	0.65	0.698
			0.87117	2.1972	0.6502	0.69861
5	0.5 (2)	2.5	1.197	2.23	0.994	1.058
			1.197	2.23	0.99379	1.0579

For each case, the top row is their results and the second row is the results produced here. They did not show results for case 4. The majority of the error is due to the rounding to the third decimal place in Salas 1991[65], therefore it can be stated that our results match to three decimal places. None of the errors exceed 1%.

An important result is the mapping of each possible wave diagram (flow pattern) to each region in the parameter space. This improves our understanding of the transitions between the cases and enables prediction of the flow field for a given (M_S, A_2/A_1) pair. A comparison of this map between Salas 1991[65] and the results produced by the current work is given below in Fig. 4. Recall, the horizontal line in Fig. 4a) and 4b) is the incident shock strength for which the piston velocity behind it is sonic (for air, $M_S = 2.068$). Notice that the curve b in Fig. 4a) asymptotes to infinity as the area ratio $A_2/A_1 \rightarrow \infty$.

a)   b)
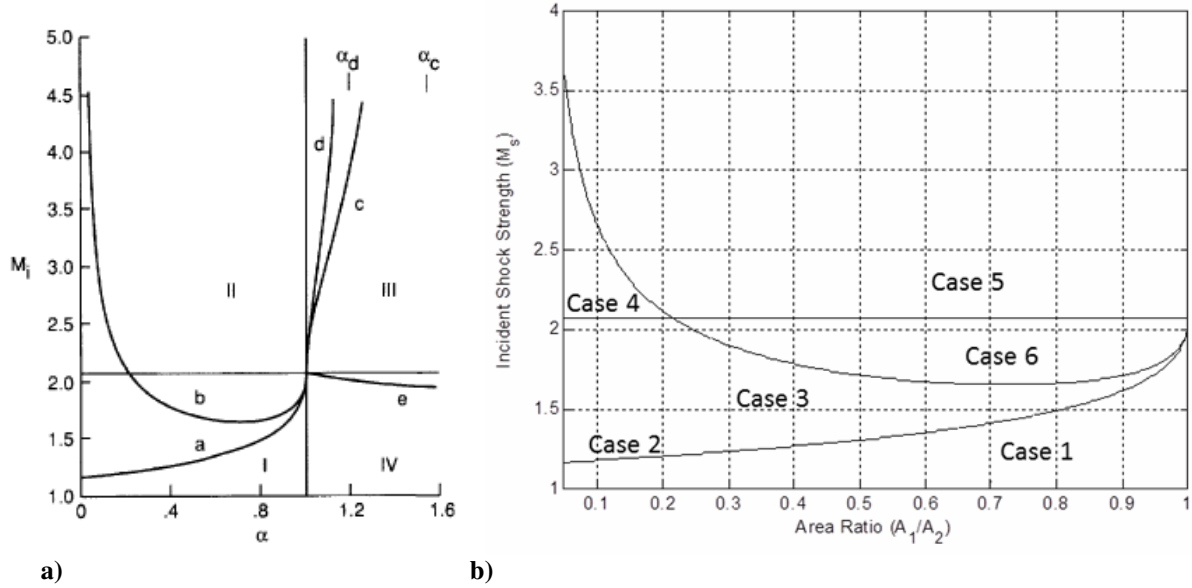
Figure 4. Map of the six possible wave diagrams to the parameter space (M_S, A_2/A_1). *a) Taken from Salas 1991[65] . $M_i = M_s$, $\alpha = A_1/A_2$. Only left portion is relevant here. b) Current results.*

From a physical standpoint, these flows are quite similar to convergent-divergent (De Laval) nozzle flows. The reflected expansion propagating into the smaller duct functions similar to the convergent portion of a nozzle in that it accelerates the flow to sonic velocities. To extend the analogy, the large duct is like the divergent portion of the nozzle. Case 1, where the reflected expansion is not yet strong enough to accelerate the flow to sonic velocity, is akin to the "unchoked nozzle" in which the flow simply expands subsonically through the convergent-divergent nozzle. Cases 3 and 6, where the tail of the expansion is caught at the discontinuous area change (yielding a sonic velocity there), can be thought of as "choked nozzle flow". The flow then expands supersonically through the area change into the large duct, even forming a nozzle-like contour. Cases 4 and 5, where the flow at the "throat" (area change) is already travelling supersonically, are special cases of "choked" nozzle flow in which it is possible to have greater than sonic velocity at the "throat", where an isentropic sonic throat can be defined. The transition from case 3 to 4 and from 6 to 5 is similar to the transient starting process of a nozzle in a supersonic wind tunnel: a stationary shock forms just downstream of the throat (the stationary secondary shock present in the wave diagrams for these cases) and is subsequently pushed downstream (the secondary moving shock present in the wave diagrams for these cases) and out of the nozzle.

It is quite clear from both of these presentations that the current algorithm produces accurate and reliable results. Thus, the remainder of this report will focus on comparing these quasi-1D results with 2-D numerical results.

C. Numerical

A total of 16 simulations were run using the General Aerodynamic Simulation Program (GASP)[100]. GASP is a 3D CFD flow solver that was used to compute these unsteady flows on a local cluster. Pointwise was used as the grid generator[101]. All grids used a uniform (square) grid spacing of 0.0003 m (0.0002 m for the grid convergence studies), resulting in 2D rectangular structured domains. All simulations were run implicitly using a second-order dual-time stepping method to avoid numerical stability issues. The Roe scheme with the Harten entropy correction was used in conjunction with the Modified ENO limiter around the shocks. The choice of scheme was proven to have a negligible effect on the solution (when compared with van Leer), and the chosen limiter provided the smallest amplitude numerical overshoot around the shocks. A third-order upwind-biased scheme in space was used.

The simulations were chosen to study three area ratios at four incident shock strengths each. The incident shock strength determined the case (discussed above). After these initial twelve simulations were run for 2500 time steps each, more information was desired from those with the more complicated flow fields. Hence four cases were run for double the amount of time (5000 time steps each) and with a larger domain (0.7 m in length). Thus, 16 simulations were run and discussed. The domains for all three geometries are shown below (see Fig. 5), and a summary of the remaining numerical settings can be found in the Appendix.

The first 0.05m of the small duct (to the left of the dashed line) was initialized to the post-shock conditions appropriate for the case, and the remaining 0.05m of the small duct and the entire large duct were initialized to the reference conditions. All boundaries were walls except for the leftmost (inflow) and rightmost (outflow) boundaries, and the area ratio was changed via moving the top wall of the large duct.

D. Grid Covergence Studies

To ensure that the result were independent of the chosen grid, grid convergence studies were performed for all 16 simulations. These simulations were run using a uniform square grid spacing of 0.0002m, and the same time step and total run time as the previous simulations. At each time step, the difference in pressures between the two grids was calculated at each grid point along a single i-line in the domain. The average difference (error) between the two grids was calculated for each time step, and these values were subsequently averaged for each simulation. For the initial 12 cases, the average error was < 1%, and for the four long cases, < 4%. It was noticed that the largest errors tended to be differences in amplitudes (numerical overshoots) at shock locations, but both grids placed the shocks in the same locations. To quantify this, the difference in the transmitted shock location was compared for the two grids, averaged over the total simulation time for each case. This matched to within 0.25% for the first 12 cases, and
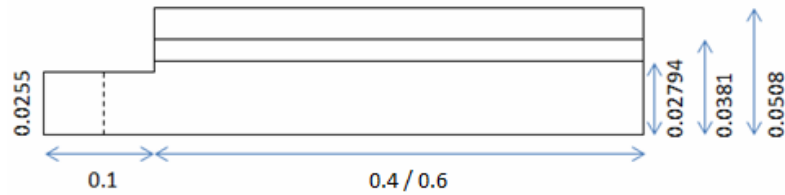

Figure 5. Domain Geometry for Simulations *(all dimensions in meters)*

to within 0.125% for the four long cases. The error in the transmitted shock location decreased over time (see Fig. 6). It can be safely declared that these studies are grid independent.

E. Numerical Verification and Validation

To further verify that the chosen methods and settings produce accurate results, the same numerical methods were applied to several studies from the literature. Selection criteria included a discontinuous area enlargement with a rectangular cross-section, preferably with comparisons of experimental and numerical results. The author was only able to find three sources that matched these criteria, of which two are presented here.
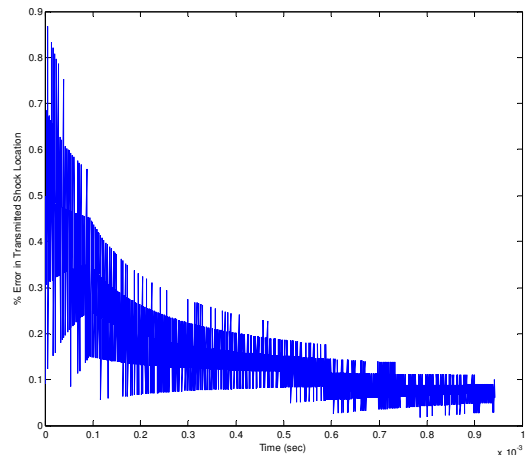
Shock Wave Interacting with a Square Cavity:

Figure 6. % Error in the transmitted shock location over time for case (1.50, 2.0). *Note: All case nomenclature defined as (M_S, A_2/A_1).*

Igra et al. (1996)[88] did an experimental and numerical study of a shock wave interacting with a square cavity at two different incident shock strengths, $M_S = 1.30$ and $M_S = 2.032$. The first part of the simulations before the shock wave interacts with the opposing cavity face are comparable here. In Fig. 7, the $M_S = 2.032$ case is shown for several isntants in time. The time step was not given in Igra et al. 1996[88], but was chosen here as 6.25E-7 sec. The initial conditions are $P_0 = 0.9$ bar and $T_0 = 22.6°C$, and the uniform grid size was ~ 0.0002m (or 0.2 mm). The results show excellent agreement, capturing all of the flow features. The minute differences are due to errors in the shock starting location and in specific data visualization techniques (number and spacing of density contours). The agreement with the previous numerical simulation serves to verify our numerical methods, and the agreement with experiment validates the chosen models.

Shock Wave Interacting with an Expansion Chamber:

Igra et al. (2001)[90] also performed an experimental and theoretical study of a shock wave interacting with double-bend ducts that included an extension of the middle leg (i.e. an expansion chamber). They studied four geometries, only two of which will be compared below. One had a shorter expansion chamber of length 80 mm, and the second had a larger expansion chamber of length 160 mm (see Fig. 8). The long expansion chamber was studied at an incident shock strength of $M_S = 1.53$ with ambient conditions: $P_0 = 0.982$ bar and $T_0 = 23.7°C$. The time step

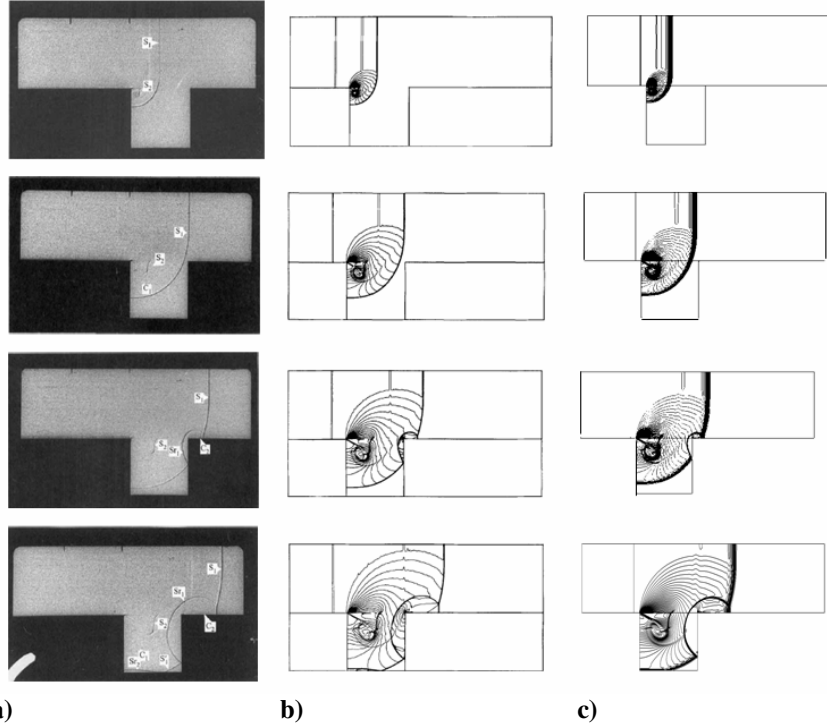a)   b)   c)

Figure 7. Shock Wave Interacting with a Square Cavity at $M_S = 2.032$.
Experimental schlieren/shadowgraphs taken from Igra et al. 1996[88]. b) Numerical isopynics taken from Igra et al. 1996[88] c) Numerical isopycnics produced from current numerical methods.

was chosen here (not reported in Ref. 90) to be Δt = 1e-06 sec. Again, the observed agreement verified and validated our methods.
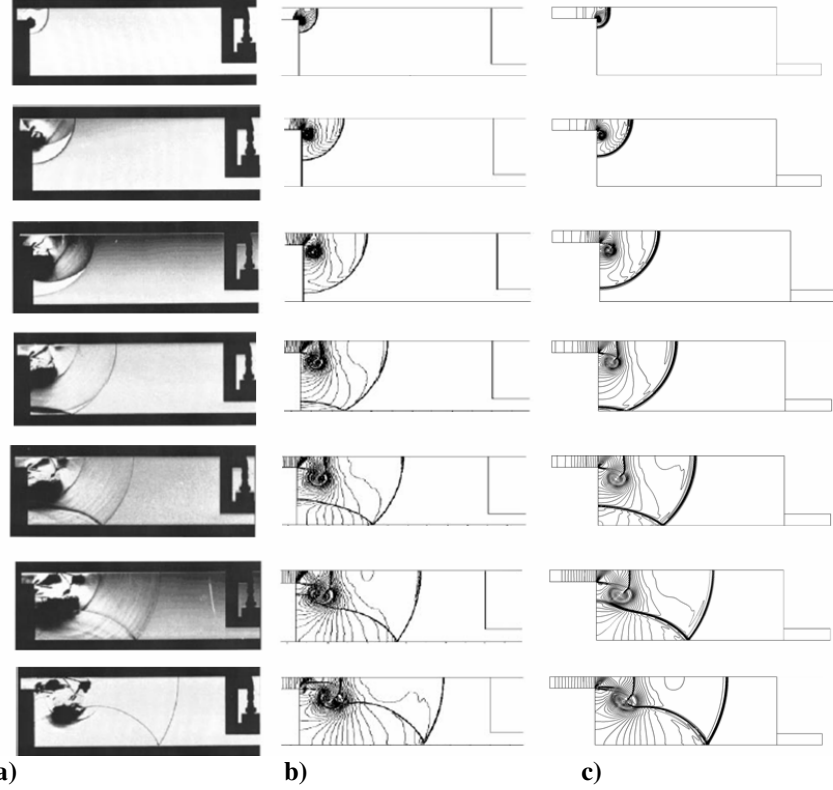
Figure 8. Shock Wave Interacting with a Long Expansion Chamber at M_S = 1.53. *a) Experimental schlieren/shadowgraphs taken from Igra et al 2001[90]. b) Numerical isopynics taken from Igra et al. 2001[90] c) Numerical isopycnics produced from current numerical methods.*

IV. Qualitative Results and Discussion

A. Common Flow Features

In order to thoroughly discuss the results, some nomenclature and fluid dynamic phenomena must first be defined and established. These known and new results will be discussed in the context of full-field pressure and vorticity scalar maps. This flow visualization will provide in-depth knowledge and insight into the intricate details and primary waves in these unsteady multidimensional flow fields. The pressure fields will reveal the flow structures and the vorticity fields will provide information about the inviscid slip lines that will become viscous shear layers. The properties of these shear layers is one of the drivers of this study.

As the discussion progresses, one will notice several common features in these flows (of which there are four): The first is that all flows with incident shock strengths of $M_S < 2.068$ (at least initially) have a vortex adjacent to the corner of the area change. This is the mechanism through which the flow expands. For all flows $M_S > 2.068$, the flow expands via an expansion fan centered at the corner, similar to that seen in supersonic nozzles. This mechanism is documented in Ref. 35.

The second is the presence of a highly two-dimensional semi-circular expansion (SCE) that originates at the corner and expands radially (see Fig. 9). To be more specific, the expansion propagates *downwards* from the corner, becoming curved and finally semi-circular. From there, two possibilities emerge: For all cases where $M_S < 2.068$, the left-running portions (and reflections) form the "reflected expansion" seen in cases 1, 2, 3, and 6. The expansion is still two-dimensional as it enters the small duct, but eventually becomes quasi-1D. *The author believes this is the origin of the reflected expansion present in the theoretical results.* For cases where $M_S > 2.068$, waves cannot propagate left by definition and the expansion becomes steady, centered on the corner (discussed above). For all cases, the right-running portions (highly 2D) proceed to oscillate in an oblique fashion between the top and bottom walls of the larger duct. These low pressure waves interact in an interdependent fashion with the oscillating shock wave, to be discussed next.
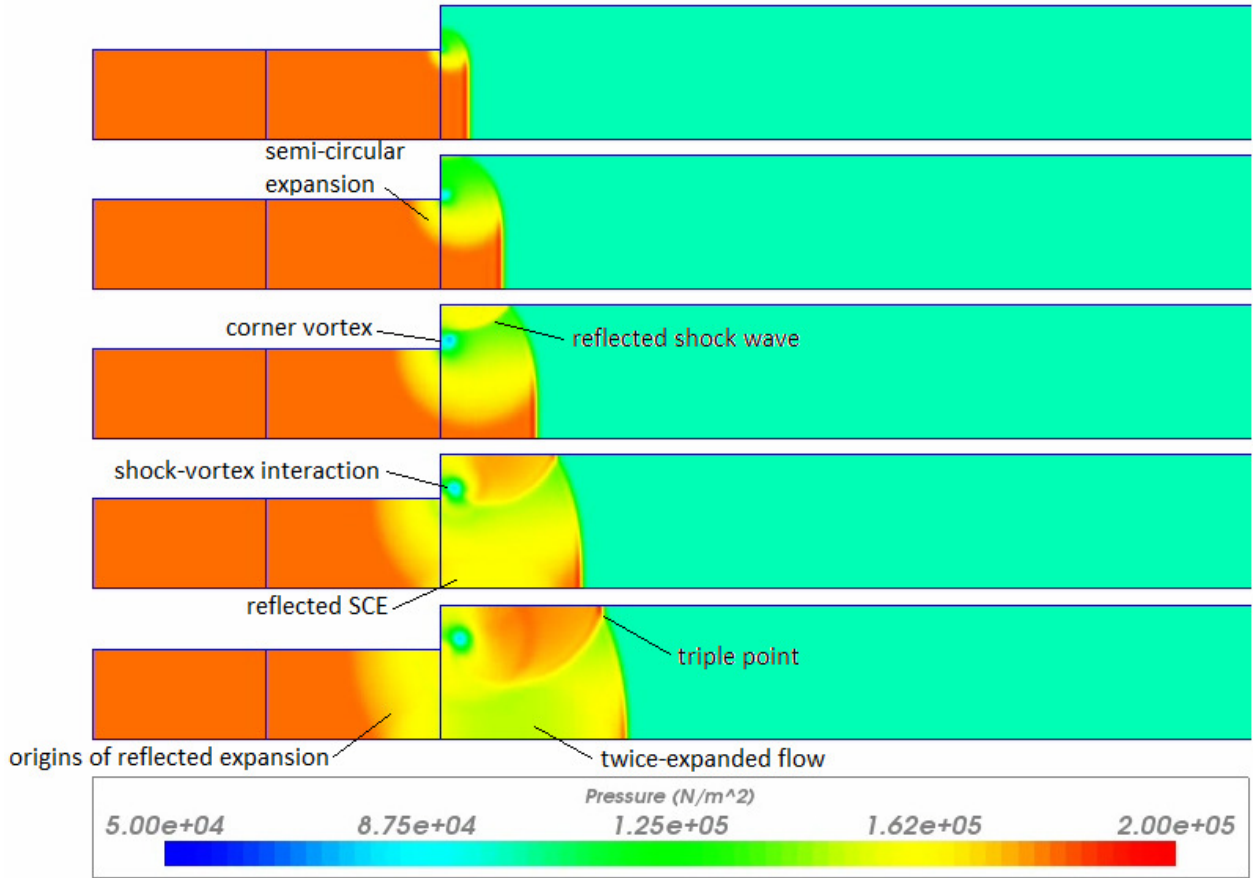
Figure 9. Full-Field Pressure Map for Case (1.30, 1.5), *illustrating the semi-circular expansion and the formation of the reflected expansion.*

The third is the presence of a shock (or compression) wave, hereafter termed the Oscillating Shock Wave (OSW). As the transmitted shock propagates through the area change, the top portion curves *upwards* to meet the duct top wall. As the curvature expands and the wall shock travels up the upper left wall, it eventually reaches the top wall and reflects off of it. Jiang et al 1997[76] term this reflected wave the "reflected shock wave". This wave passes (on its downward journey) through the corner vortex, interacting with it. The surviving portion continues to propagate downwards and reflect off of the bottom wall. After this (second) reflection, it continues to bounce between the top and bottom walls, giving it the name the oscillating shock wave. With each reflection, it sends oblique compressions or shock waves (depending on the gradients) both to the left and right, establishing other prominent flow features. The right-running oblique compressions travel faster than the transmitted shock, and thus eventually catch up to and merge with it. Each time this happens, the transmitted shock experiences a sudden jump in its strength. Each new reflection also brings a decay in the strength of the OSW, such that over a sufficient amount of time the OSW becomes indistinguishable. This shock has very interesting acoustic properties since it behaves like a plucked guitar string. The primary difference is that its length is a function of time, since the transmitted shock (corresponding to its right end) continues to propagate right, and its left endpoint also moves (though in a significantly less predictable manner). The frequency of its oscillations determines how often oblique shocks or compressions are sent upstream and downstream, and thus in turn, how often and to what degree the transmitted shock strength is modified. The oscillating shock wave has been seen by other researchers, where it is indicated by the red arrows in Fig. 10. An example of the oscillating shock wave in the current results is given below in Fig. 11.

The interplay between the semi-circular expansion and the OSW is what drives the majority of the flow features seen in these flows (see Fig. 13). The degree of the area change affects this interaction: Since the SCE initially propagates downwards and the shock wave initially propagates upwards, the degree of area change essentially controls the "phase difference" between the two waves. The smaller the area change, the more closely the OSW follows the SCE, and thus the smaller the phase difference. The larger the area change, the further apart the two

waves are in time and space, and thus the larger the phase difference. In fact, at an area ratio of 2, the waves are initially nearly opposite, i.e. the phase difference is approximately 180°. This can be seen in Fig. 13c), where the wall shock reaches the duct top wall and the leading wave of the SCE reaches the duct bottom wall at almost the same instant. However, both waves decay over time, and this leads to a time variance of the phase difference due to transient changes in the amplitude and period of both waves.
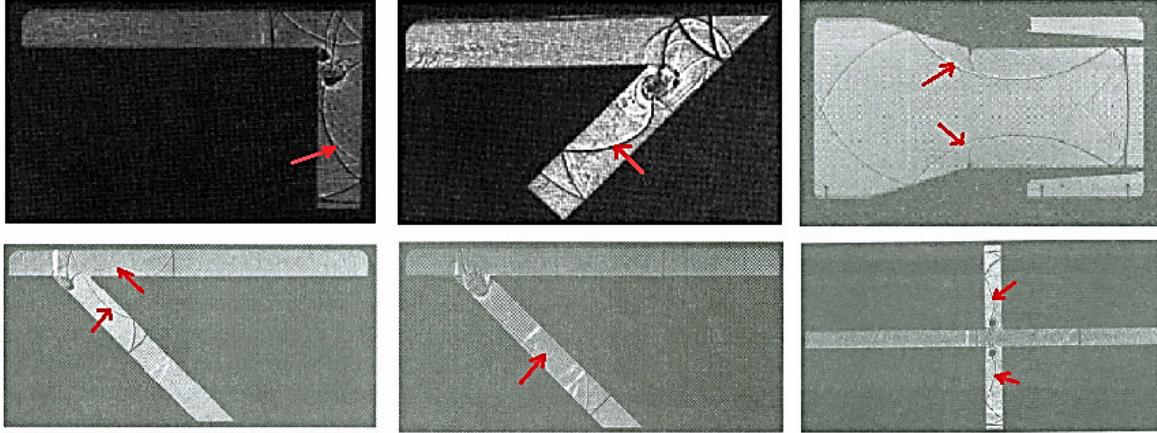
Figure 10. Examples of Oscillating Shock Wave. Red arrows indicate presence of OSW. All photos taken from <u>Handbook of Shock Waves</u>[35].
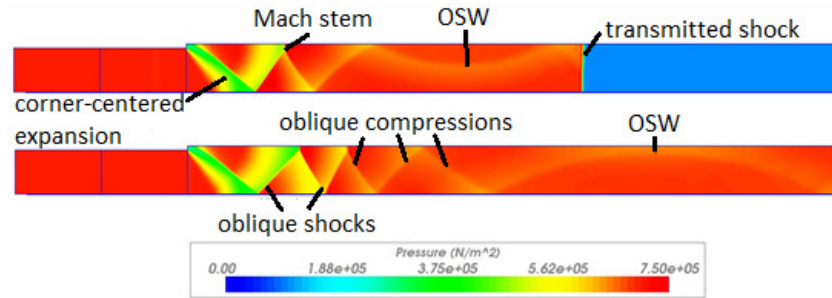
Figure 11. Example of oscillating shock wave. Case (2.48, 1.1)
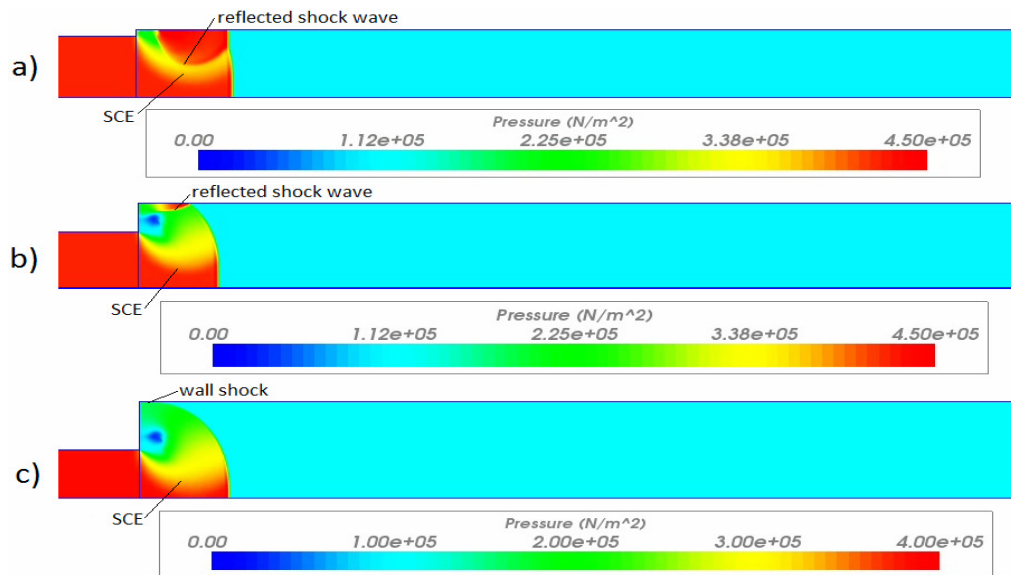
Figure 12. Illustration of phase difference between SCE and OSW. *a) Case (1.93, 1.1) b) Case (1.93, 1.5) c) Case (1.85, 2.0)*
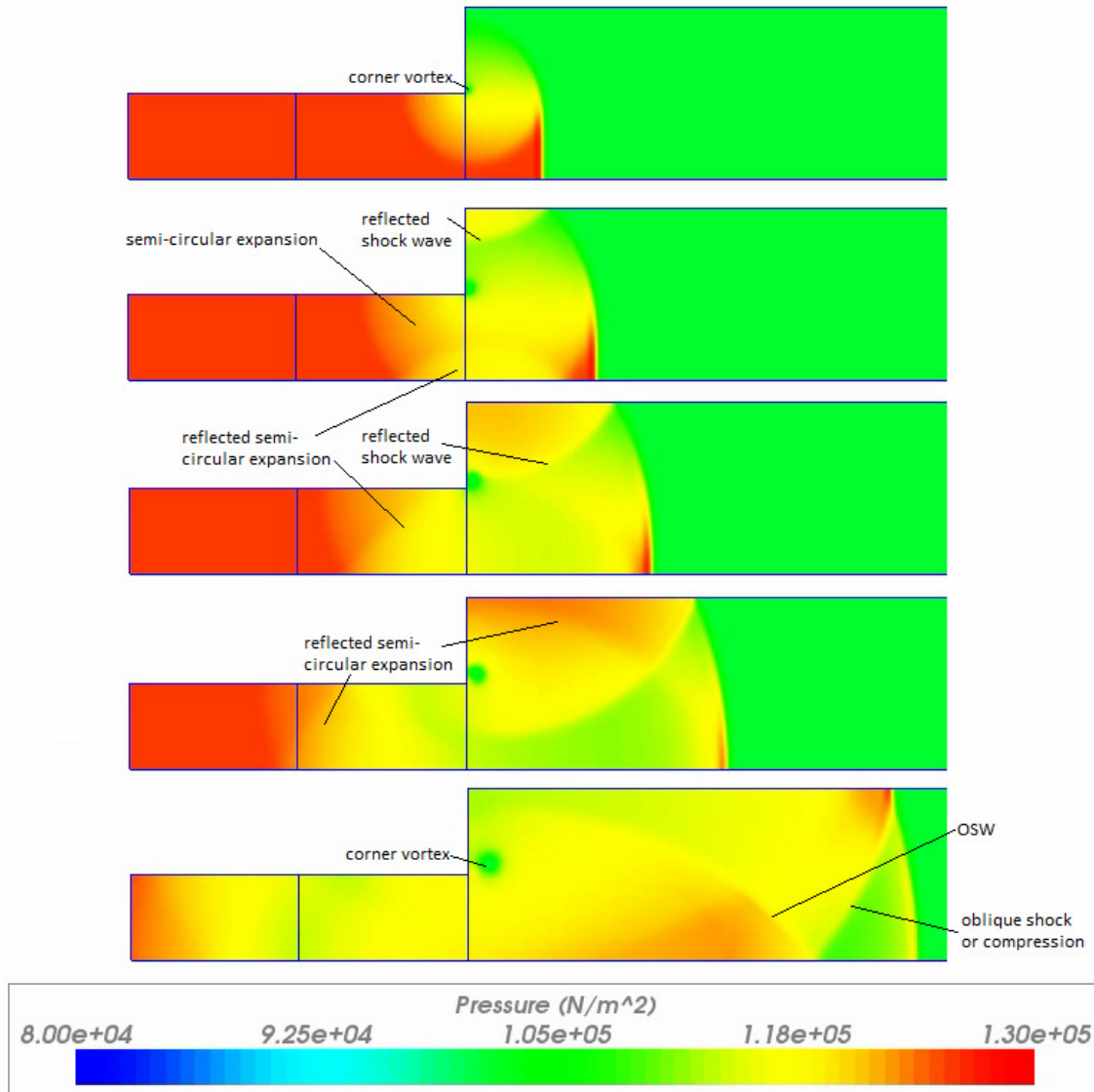
Figure 13. Illustration of the interplay between the OSW and the SCE. *Case (1.10, 2.0)*

The fourth is the presence of the transmitted shock. It must be there, since it is the continuation of the incident shock through the area change. A triple point propagates along its surface that provides an interface between low and high pressure regions behind the transmitted shock. The low pressure region is most likely caused by the right-running expansions (discussed above) that oscillate between the top and bottom walls, and it also causes a bulging (or curving) of the transmitted shock. The lower the pressure, the more the transmitted shock curves. The high pressure region is caused by the attachment of the oblique shocks (or compressions) generated by the OSW to the transmitted shock. The triple point always moves into the low pressure region and leaves the high pressure region behind it. The transmitted shock is straightened by the passage of the triple point and the creation of the high pressure region. *In other words, the low pressure region curves the transmitted shock and the high pressure region straightens it.* Over time, as the gradients between the two lessen, the curvature lessens, and each subsequent passage of the triple point results in a straighter transmitted shock, until the transmitted shock finally becomes planar.
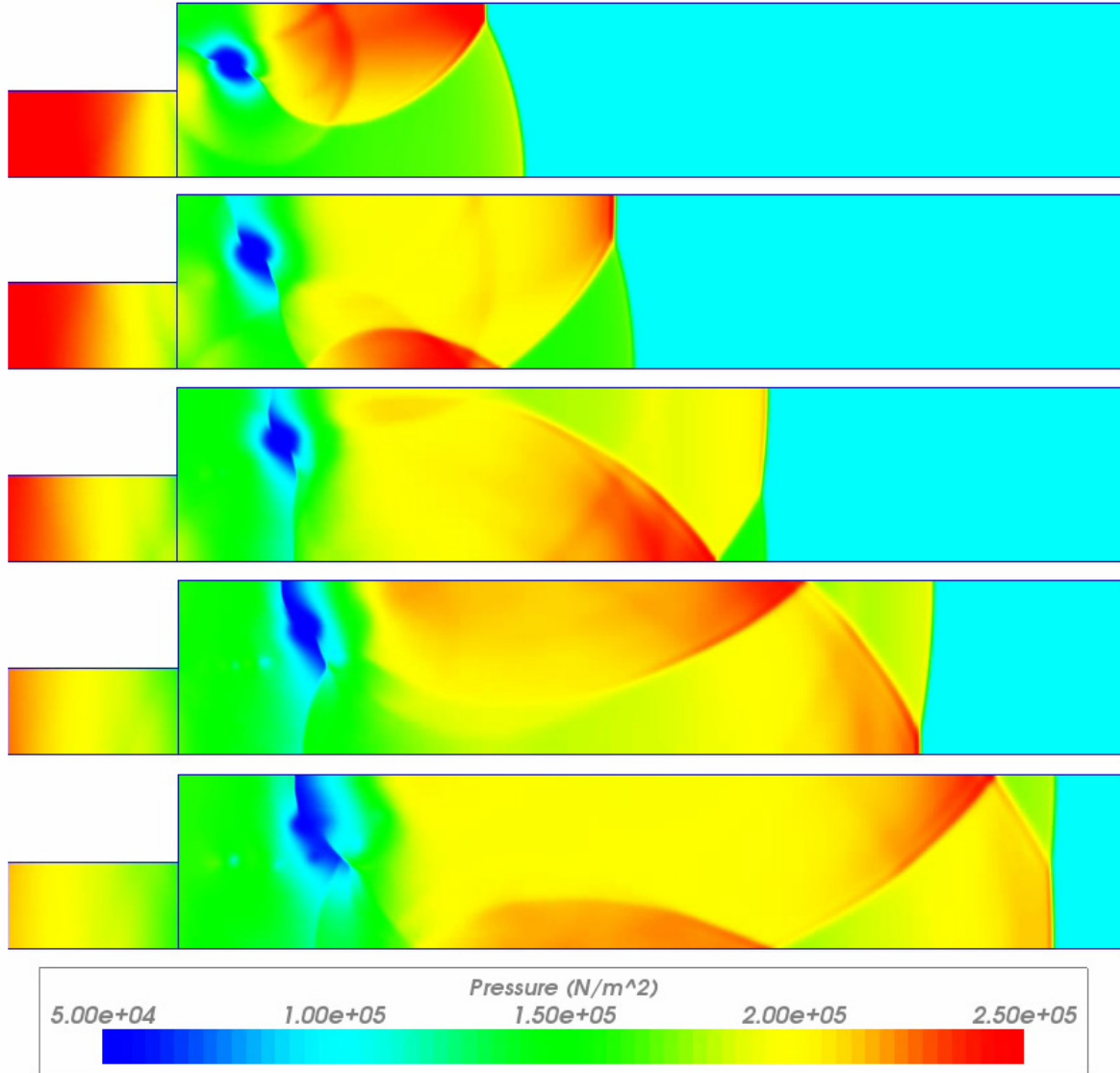
Figure. 14. Illustration of triple point motion along transmitted shock. *Case (1.50, 2.0)*

At this point, a new definition of the time it takes to reach quasi-1D flow can be offered. The theory assumes that "a long enough time has passed such that all transient effects have subsided and waves propagate with constant velocity." Knowing the detailed flow mechanisms, one can now say that this time – τ_{1D} – can be defined as:

    a) The time it takes for the oscillating shock wave (OSW) and the semi-circular expansion (SCE) to inviscidly decay out of existence. This implies that

    b) The left- and right-running oblique shocks/compressions also decay in strength, which implies that

    c) The transmitted shock strength ceases to change and/or the transmitted shock becomes planar (a 5% criteria on the shock wave strength was used here)

B. Other Salient Flow Features

In addition to these flow features common to all the cases, the individual cases exhibited peculiarities in the flow structure specific to each case. Due to the wealth of the information provided by the simulations and the limited space in this paper, a short discussion on each specific flow feature is included here. For the most part, the transmitted shock and the reflected expansion exhibit good agreement with the theory, despite having two-dimensional origins. However, the phenomena associated with the secondary shock differ dramatically from case to case. The purpose of the secondary shock is to compress the supersonically expanded flow exiting the area change

14

to the conditions behind the transmitted shock. The method through which the flow accomplishes this is a highly complex, multidimensional, and transient process that requires significant further investigation.

For the cases with secondary shocks (3-6), the flow most commonly accomplishes the purpose of the secondary shock through an oblique shock train. As mentioned before, these flows exhibit characteristics similar to nozzle flows, and the oblique shock train established is quite reminiscent of the Mach diamond pattern found in nozzle flows and scramjet isolators (should one mirror the flow about the bottom wall). These oblique shocks/compressions occasionally form Mach stems that sometimes disappear over time. Likewise, the number of oblique shocks/compressions in the train depends upon the case being studied. In all cases, the right-running compressions caught up to and merged with the transmitted shock.

For all of the $A_2/A_1 = 1.1$ cases, the corner vortex dissipated very quickly into a low pressure recirculation zone in the upper corner of the area change. This recirculation region "emitted" low pressure flow that began just after the area change and traveled upstream into the small duct. In addition, the OSW and SCE travelled together with a small phase difference for these cases. In case (1.50, 1.1), the OSW was a weak compression wave that became unnoticeable after 3-4 oscillations. The right-running compressions merged with the transmitted shock, and the left running waves simply traveled left. In case (1.67, 1.1), the gradients across the OSW were stronger, but the OSW was still a compression wave. The left-running compressions/expansions interacted with the low pressure region around the area change to produce a standing *normal* shock wave, as appropriate for case 3. In case (1.93, 1.1), the OSW and SCE were stronger, but the OSW was not yet a true shock wave. All of the left-running compressions merged with the secondary shock. This is the first instance of the secondary shock taking on a very distinctive Y-shape. The left branch was formed from the reflected shock wave and the right branch was formed from the coalescing of all of the left-running oblique compressions. The stem of the "Y" was a Mach stem off of the bottom wall, which disappeared over time, as illustrated below. There are now two shocks in the shock train, with the second finally becoming a curved normal shock wave. The train only moved incrementally, not consistent with the fast secondary shock as predicted by the theory. In case (2.48, 1.1), the flow established an unsteady shock train, again contrary to the single secondary shock in the theory. The main difference between this and the three previously discussed cases was that the left-running oblique shocks/compressions *did not* merge with the secondary shock. The shocks on the left of the train pushed to the right, and the incoming oblique compressions pushed left – the combination of which resulted in a "shuffling" of the oblique shocks until all were stationary. The leftmost shock was the reflected shock, and all of the shocks intersected the top and bottom walls (this will become important later). The interesting feature was the formation and subsequent disappearance of Mach stems along both the top and bottom walls; pay particular attention to the Mach stems in Fig. 18. Eleven shocks/compressions formed the train by the end of the simulation, with more to come.

For all of the $A_2/A_1 = 1.5$ cases, the movements of the SCE and OSW were more clear and distinct, due to the higher phase difference between them. Also, the OSW was no longer a set of compression waves, but a clearly defined shock wave (at least initially). In case (1.30, 1.5), the corner vortex managed to survive the reflected shock and persist throughout the simulation. The right end of the OSW was very clearly defined, but the left end and its oblique compressions were not quite visible. The corner vortex did shed low pressure flow downwards and upstream, as seen in the $A_2/A_1 = 1.1$ cases. In case (1.55, 1.5), the gradients across the OSW were higher than the previous case. This case seemed to be a transitional case between the major flow archetypes. The secondary shock took nearly the entire simulation to form, and when it did, it took on the Y-shape. Recall, the left branch is formed from the remnants of the reflected shock wave, and the right branch from the coalescing of the left-running oblique compressions. An important feature to note was that the secondary Y-shock *did not* reach to the duct top wall as before. Instead, it was rather "stunted" and the lower pressure flow from the area change region spilled over the top of it and continued downstream. This will be discussed in further detail later. The corner vortex did not survive the interaction with the reflected shock wave, and dissipated into a lower pressure region in the flow around the area change. Case (1.93, 1.5) was one of the most interesting and complex flow fields. The corner vortex was broken apart by the shock-vortex interaction, and the reflected shock quickly established the left branch of the secondary Y-shock, which crept downstream very slowly. Soon after, a local "hot spot" was created in the flow that dissipated through the emission of compression waves that oscillated with the OSW. Similar to the previous case, the secondary Y-shock was "stunted" and lower pressure flow flowed above and around it. This weakened the gradients across the right branch of the Y. The lower pressure flow pushed downstream, and the boundary between this lower pressure flow and the higher pressure flow behind the transmitted shock soon became a normal left-facing shock wave that was pushed downstream. This third shock was connected to the second via a weak oblique shock. The tertiary shock became a Y-shock over time as the gradients across it weakened and the lower pressure flow continued to press downstream over the top of it. At the very end of the simulation (5000 time steps), the secondary shock had a Y-shape and the tertiary shock had become a pair of oblique shocks (V-shock). If one were to draw

connected straight lines through the shock waves, this is roughly similar to an oblique shock train consisting of 4 shocks. Case (2.50, 1.5) was very similar to the previous case, with the following differences: The Mach stem on the secondary Y-shock disappeared, and a tertiary shock appeared in the train. This last shock wave was a left-facing curved normal shock that was pushed downstream by the flow at a nontrivial velocity. This shock could be compared to the secondary shock predicted by the theory, but its strength and speed are off. It can easily be seen in Fig. 20 that a shock train consisting of 5 oblique shocks was formed. Notice how none of the shocks in the train are "stunted", that is they all connect to the top and bottom duct walls.

The $A_2/A_1 = 2.0$ cases were characterized by the near-180° phase difference between the semi-circular expansion and the oscillating shock wave (initially). Over time as the waves slowed, the two wave motions became asynchronous. The OSW was a crisp shock wave, and the gradients across it increased with M_S. In case (1.10, 2.0), the corner vortex lasted as an entity through the entire simulation. The left end of the OSW and its compressions were hardly visible, and overall the wave speeds involved were much slower. The right-running compressions took a relatively long time to catch the transmitted shock. Case (1.50, 2.0) was another odd transitional case. The secondary shock took nearly the entire simulation (2500 time steps) to form into a weak Y-shape, and the corner vortex was destroyed by the reflected shock and became a low pressure region around the area change. The most noticeable feature was the corner slip line emitting vortices that could be seen on the pressure maps. These vortices traveled counterclockwise through the low pressure region just downstream and back towards the area change. Since the vortices pushed past (over) the secondary shock, the low pressure region did as well. However, the boundary between the lower pressure flow and the higher pressure flow did not solidify into a shock wave. Case (1.85, 2.0) was similar to case (1.93, 1.50) in overall flow structure over time, but was far more complicated. The corner did emit vortices, as seen in the previous case (1.50, 2.0), but as the vortices passed throught the low pressure region, they instead beame low pressure waves that pushed downstream over the top of the secondary and tertiary shocks. If one examines only the primary features, then it could be said that an oblique shock train with 4 shocks was formed in this case. The Mach stem on the secondary shock disappeared. The corner vortex was destroyed, becoming a low pressure region in the flow. Case (2.50, 2.0), by contrast, had a very clean flow field similar to that seen in Case (2.50, 1.5), but with fewer stronger shocks in the train (3 compared to 5). The gradients across these three shocks were quite high, and the left-facing tertiary shock was pushed downstream, but managed to extend the entire height of the large duct. It formed Mach stems on both the upper and lower duct walls. The lower pressure seen on its downstream side is due to the fact that the gradients across the tertiary shock were not high enough to compress the flow to the pressure behind the transmitted shock.

C. Vorticity

Additional information can be gained by analyzing the vorticity maps. Since the flows are two-dimensional, the z component of vorticity was chosen. This discussion will focus mainly on the corner vortex, recirculation regions, triple-point slip lines, and the vortex-ridden lower pressure region (hereafter called the vortex zone). While shock-vortex interactions are interesting and fundamental fluid dynamic phenomena, they are not the focus of this paper, and thus will be covered sparingly. The author recognizes that there is a specialized community dedicated to analyzing these interactions.

In all of the simulations, there was a very small region with a very high vorticity gradient at the corner itself. This is most likely due to numerics because there was no grid clustering in the region of the corner. However, it proved to be of negligible importance to the flow structure.

For all of the $A_2/A_1 = 1.1$ cases with a subsonic piston velocity (3), the small corner vortex was destroyed quickly due to the small degree of the area change, subsequently becoming a higher vorticity region. The proximity to the upper duct wall tended to elongate and smoothen this region into a small recirculation zone in the upper corner of the area change. This region was bounded on the top and left by the duct walls, and the lower boundary by the flow. The size (length) of this recirculation region and the length of its influence (measured in downstream distance) increased with increasing M_S. A representative example of this is given in Fig. 15. Of these cases, only the (1.93, 1.1) case stood out. Every time the shock structure (such as a Y-shock) involved a triple point, a slip line formed that was carried downstream. These triple-point slip lines almost always went immediately unstable and began curling into vortices, particularly as the distance downstream of the creating triple point increased. This case in particular was the only one in which the triple-point slip line off of the secondary shock stayed stable for the duration of the simulation. It also exhibited "vorticity ribbing" that is believed to be purely numerical in nature. The reason behind this particular case remaining stable needs further research.
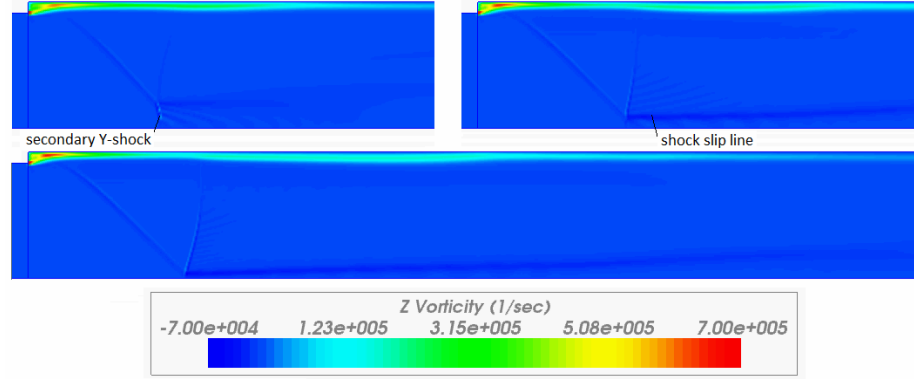
Figure 15. Case (1.93, 1.1)

The three cases with a supersonic piston velocity ($M_S \sim 2.5$) had an expansion originating at the corner instead of a corner vortex. The flow very quickly established a recirculating flow region in the upper corner of the area change. The flow boundary of this region formed a smooth nozzle-like contour. When this boundary met the duct top wall, a very thin vorticity layer propagated downstream along the top wall, influencing the flow downstream of the area change. The (2.48, 1.1) case however had a comparatively thick extension of this vorticity region, which was consistent with the other $A_2/A_1 = 1.1$ results. These vorticity "extensions" thickened upon interaction with the shocks in the oblique shock train, sometimes resulting in the formation of vortices downstream. As the secondary shock formed and the oblique shock train was established, triple points propagated along the shocks, merging at the middle of the Y. Their slip lines likewise moved and merged with them, the final merged slip line becoming unstable soon thereafter (rolled into vortices a short distance downstream). When the Mach stems on the oblique shock disappeared, the slip lines detached and were carried downstream, eventually dissolving into vortices. Slip lines from weaker triple points were just carried downstream, remaining stable (thin slip lines).

The remaining 6 cases had a very well-defined corner vortex and a corresponding shock-vortex interaction. The corner vortex was connected to the slip line emanating from the corner itself. The behavior of the two features was very interactive and interdependent. The important finding here is that the slip line behavior is *neither* similar to that of a splitter plate *nor* is it attached to any of the shock waves in the flow. Instead, it is deeply engrossed in the corner vortex; thus to understand the slip line (and eventual shear layer) behavior, one must understand the behavior of the vortex. Furthermore, in some of the cases, the slip line became "unstable." In this discussion, "stable" is defined as a slip line (of whatever origin) that does not oscillate in the vertical plane and contains no ripples or vortices. "Unstable" behavior is characterized by a vertical oscillation about the initial slip line angle, whereby it seems to be "flapping in a breeze" – an example of the Kelvin-Helmholtz instability. This nomenclature will be used throughout this discussion.
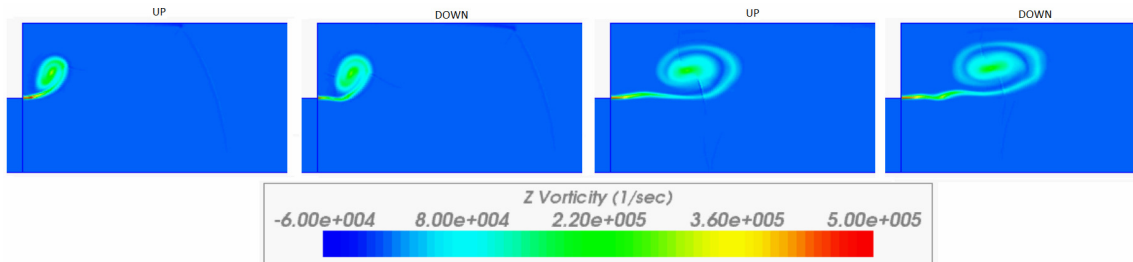

Figure 16. Illustration of unsteady "flapping" motion. *Case (1.50, 2.0)*

For the most part, the early interaction process between the slip line and the corner vortex was the same until the reflected shock wave interaction: The vortex unfurled from just above the corner, moving downstream from the area change. As it did, the slip line lengthened appropriately and curled around the corner vortex, the two highly intertwined. At the lower incident shock strengths, the vortex was circular, and as M_S increased, the vortex elongated. As the reflected shock wave passed through the corner vortex, one of several things happened:

a) The reflected shock wave passed through the corner vortex without any noticeable disturbance to the vortex

b) The reflected shock wave split in two upon interacting with the corner vortex (reflected shock wave and split shock wave)

17

c) The reflected shock wave split the corner vortex in half (itself splitting as well), causing its eventual dissolution

With these general flow features in mind, the discussion will proceed with a case-by-case analysis of the individual differences. Case (1.30, 1.5) exhibited a small amplitude oscillating behavior in the corner slip line, indicating the potential to become unstable. These oscillations simply caused the subsequent portions of the slip line to "pass the ripple" until the ripple arrived at the vortex. The vortex moved counterclockwise inside the recirculation region bounded by the slip line in the upper corner of the area change. As the vortex moved downwards, it "pushed" the slip line downwards, causing it to "bulge" into the flow path. The outer boundary of the slip line did not form a smooth flow contour. In case (1.55, 1.5), the corner vortex unfurled from the wall slightly elongated. The angle the slip line made with the horizontal was ~0°, and a small amplitude oscillation set in. The oscillations caused the slip line to "bunch up" into small "packets of vorticity" that propagated along it, and they interacted with the vorticity field created by the corner vortex. The small vortices, always moving counterclockwise, continuously pushed downstream, thereby growing the recirculating region. The final vertical thickness of the recirculation region was almost equal to the height difference between the two ducts. In case (1.93, 1.5), the corner vortex again began oval-shaped, but the passage of the reflected shock wave seemed to initiate the instability in the slip line. The slip line was angled upwards (~10°) and oscillated about this angle. The corner vortex quickly dissipated into the recirculation region, whose flow boundary formed a shape similar to that of a smoothly diverging nozzle. This region continuously pushed downstream, in contrast to the previous cases where it always recirculated back towards the area change. To be more correct, the rate at which this vorticity zone pushed downstream exceeded the rate at which it recirculated. In Fig. 26, notice how the oblique shocks in the shock train do *not* meet the top wall, but are instead *bounded* by this vorticity zone. *The author believes that is this the gas-dynamic mechanism through which the lower pressure flow can invade the higher pressure region.* This particular finding (this "gas-dynamic pathway") could be important for creating flow induction in the transient inlet concept.

Case (1.10, 2.0) began with a perfectly round corner vortex that was not affected by the passage of the reflected shock wave. The slip line, however, exhibited a *very slow* (long period) oscillation. The oscillation did not cause the slip line to "ripple", but it did warp and curve. The flow did *not* create a recirculation region; instead, the slip line simply curled around the corner vortex. Case (1.50, 2.0) is one of the most interesting cases because the full-solution pressure fields reveal that the corner emitted vortices. The corner vortex was initially highly elongated, curling upwards from the corner. It was obvious for this particular case that the reflected shock wave caused the instability in the slip line because it caused the initial downward stroke in the slip line oscillation. Almost immediately afterwards, the slip line rebounded and began emitting vorticity ripples that quickly evolved into vortices that propagated along the slip line towards the corner vortex. These vortices moved counterclockwise around the vortex and deformed it, as well as pushed further downstream, lengthening the recirculation region. Furthermore, these vortices demonstrated a strong interaction with the secondary shock wave: each new vortex caused a "crease" in the left branch of the secondary shock, which in turn created a triple point and attached slip line. The triple point slip lines curled around the vortices moving downstream (dark blue in Fig. 28). This was the second case in which these downstream-moving vortices restricted the secondary shock and allowed the lower pressure flow to move over it. Case (1.85, 2.0) was very similar to that of (1.50, 2.0), having similar developments over time. It was noticed that the interaction with the reflected shock wave is what caused the instability in the slip line. The corner vortex elongated and deformed, forming the recirculation region. The slip line was sharply angled upwards (~25-30°) and emitted vortices that behaved as described above. These vortices interacted with the secondary and tertiary shocks in a similar manner. As these vortices moved downstream, they invaded the flow beneath them, demonstrating the third and final occurrence of the gas-dynamic pathway.

A short summary of the pertinent observations from the discussion on vorticity follows:

a) Cases (1.30, 1.5) and (1.10, 2.0) were the only cases in which the corner vortex survived the entire simulation.
b) Cases (1.93, 1.5), (1.50, 2.0), and (1.85, 2.0) were the only cases in which the vorticity region along the duct upper wall seemed to provide a gas-dynamic pathway for the lower pressure flow surrounding the area change region to overflow the oblique shock train and move downstream into the higher pressure flow behind the transmitted shock wave.
c) In Cases (1.50, 2.0) and (1.85, 2.0), the corner emitted individual and distinct vortices that were visible in both the pressure and vorticity maps.
d) The present simulations suggest that the passage of the reflected shock wave is the cause of the instability in the corner slip line for all 6 cases, rather than being naturally unstable. [HYPOTHESIS NEEDS MORE SUPPORT]
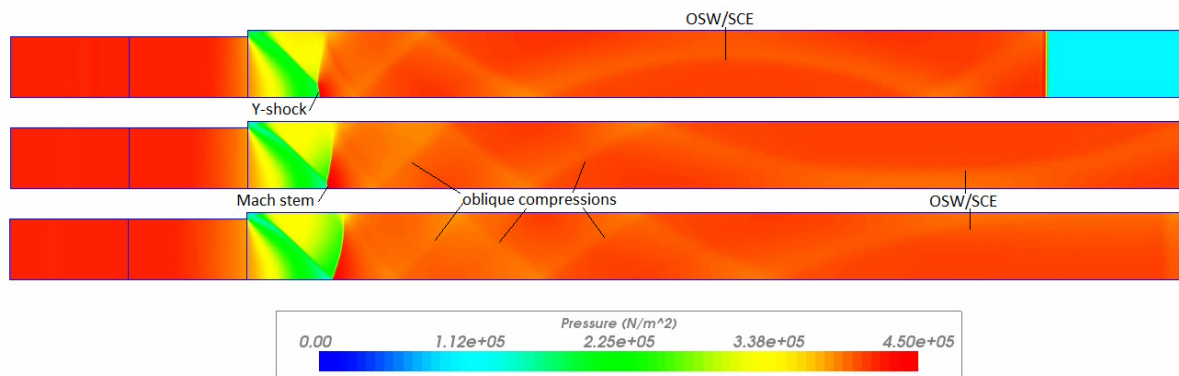
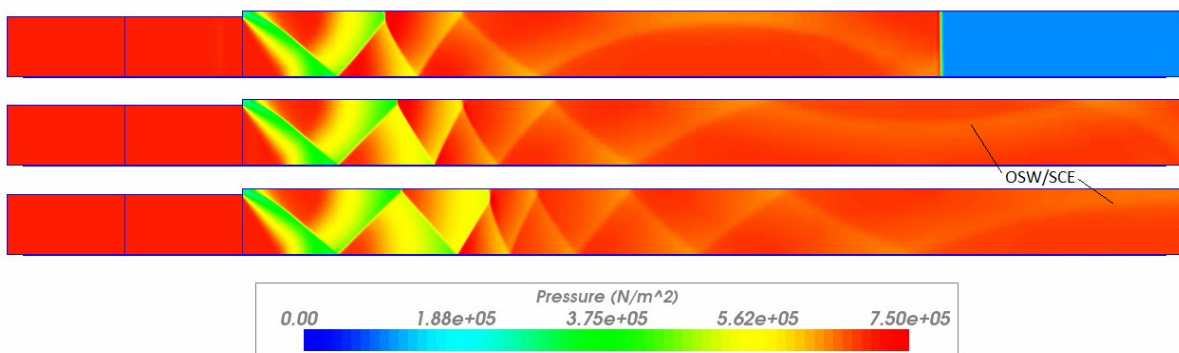**Figure 17. Full-Solution Pressure Map for Case (1.93, 1.1)**

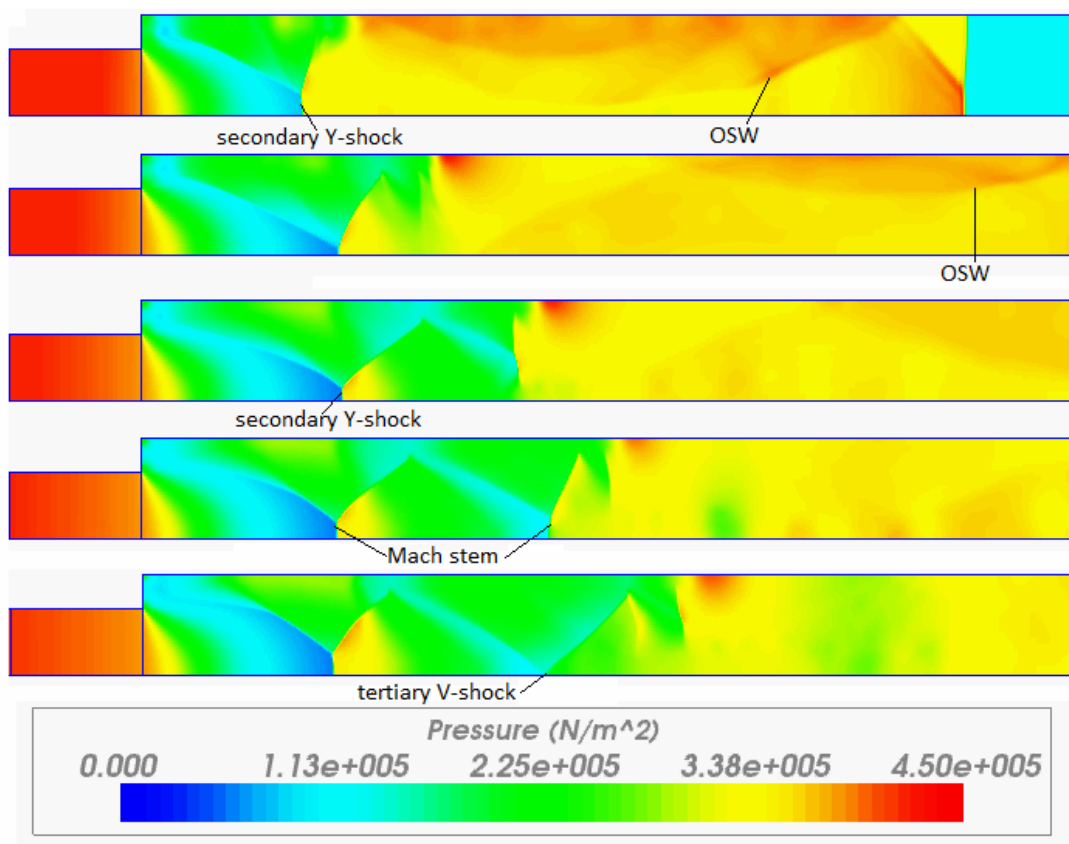**Figure 18. Full-Solution Pressure Map for Case (2.48, 1.1)**
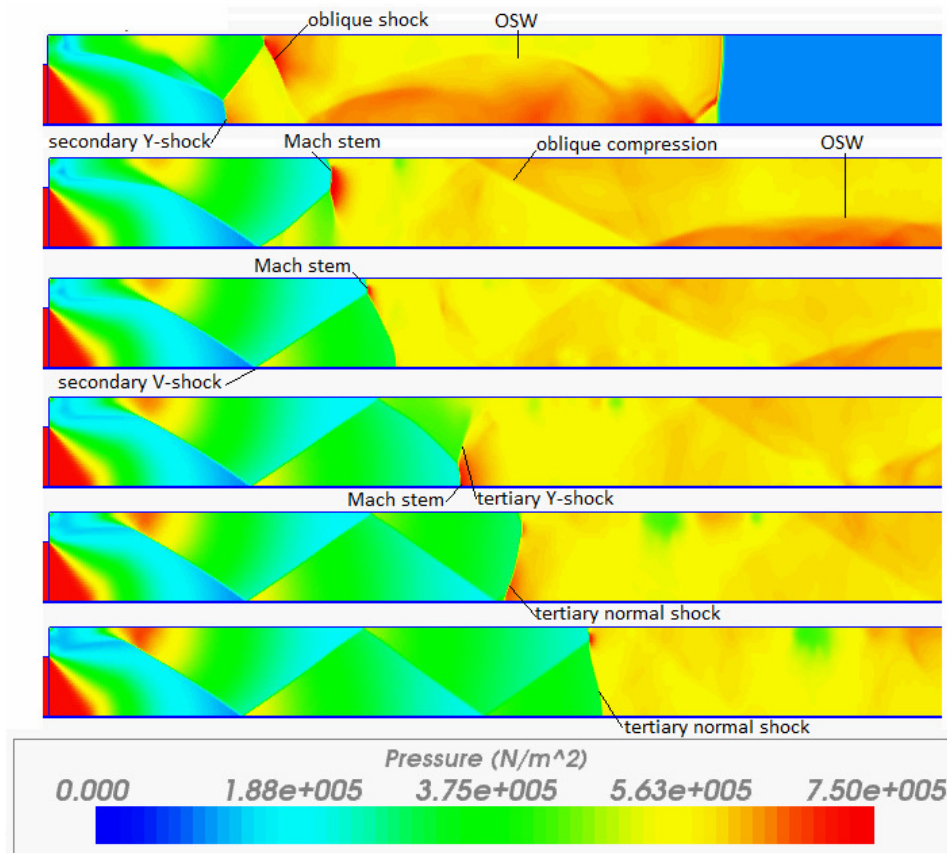

Figure 19. Full-Solution Pressure Map for Case (1.93, 1.5)

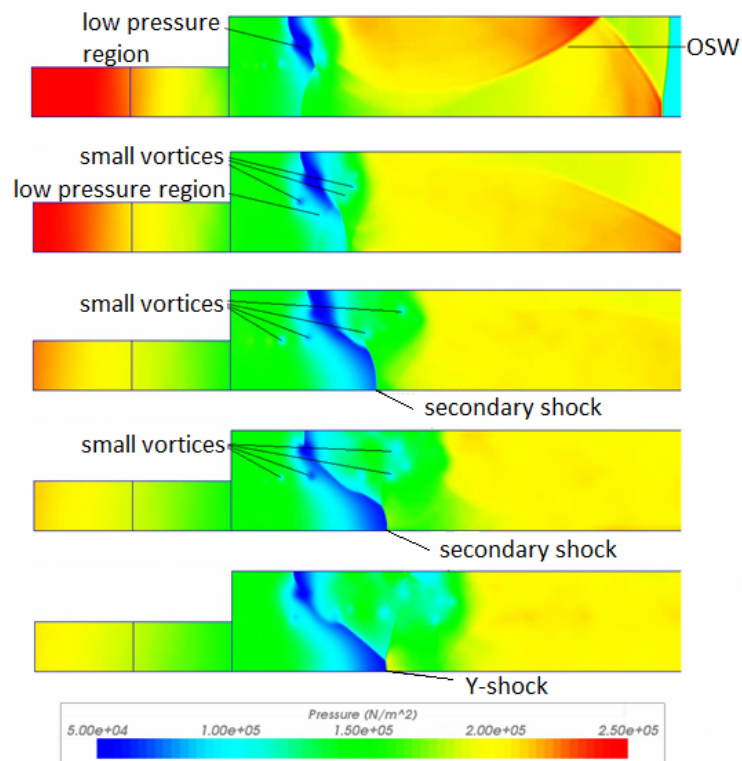**Figure 20. Full-Solution Pressure Map for Case (2.50, 1.5)**

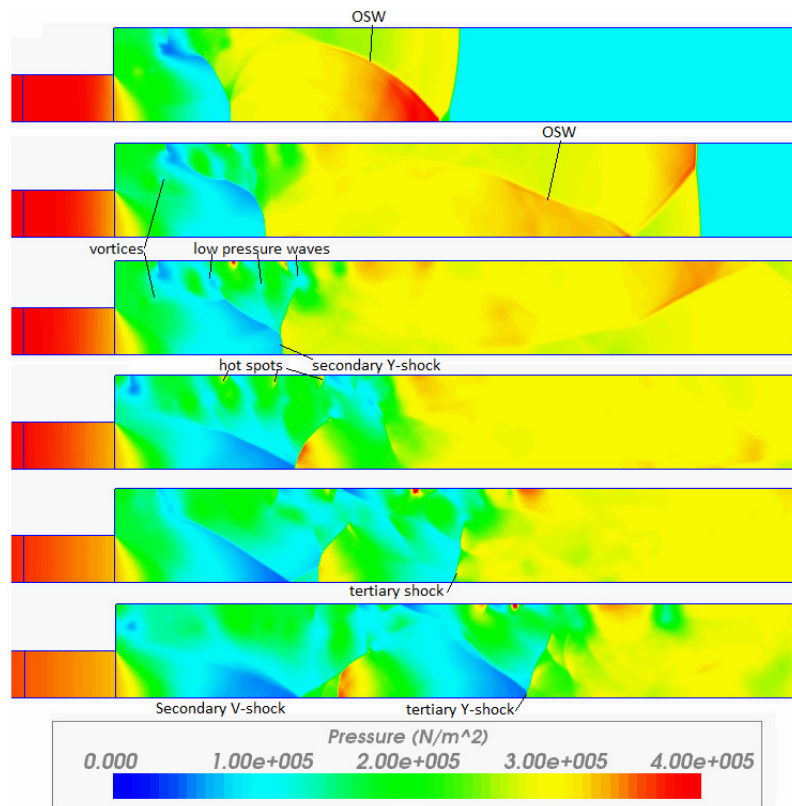**Figure 21. Full-Solution Pressure Map for Case (1.50, 2.0)**

20

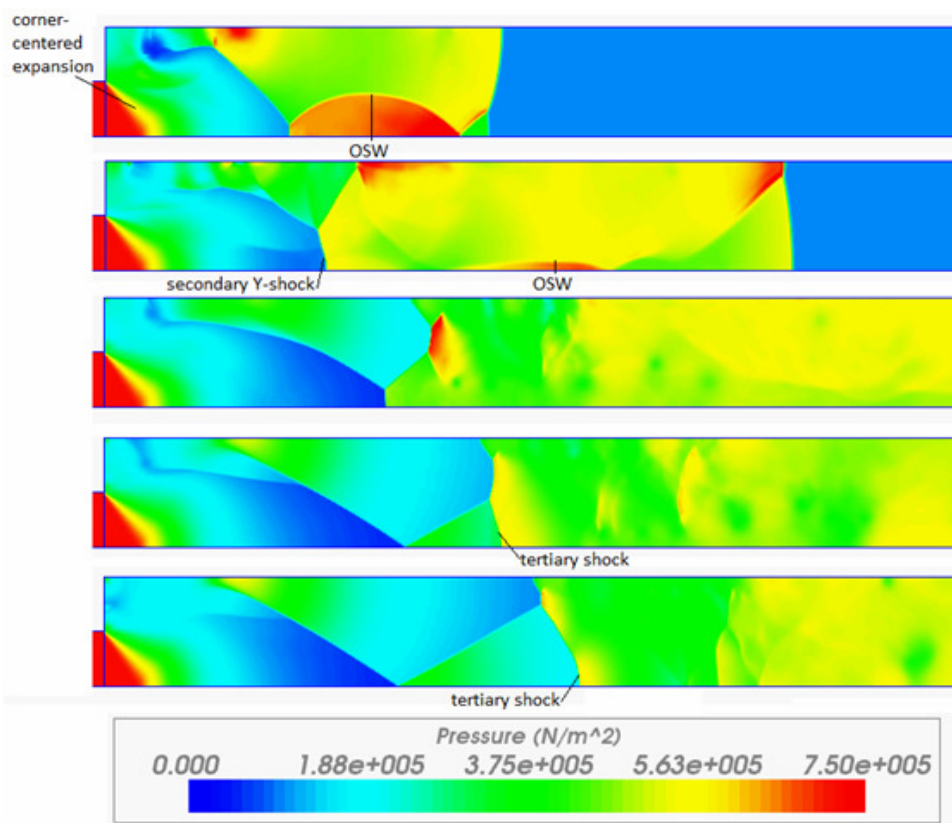**Figure 22. Full-Solution Pressure Map for Case (1.85, 2.0)**

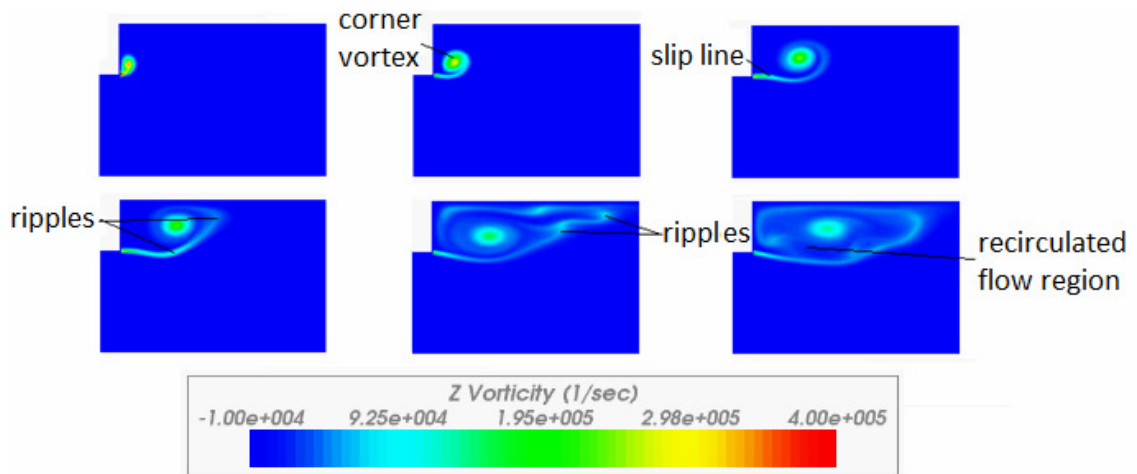**Figure 23. Full-Solution Pressure Map for Case (2.50, 2.0)**
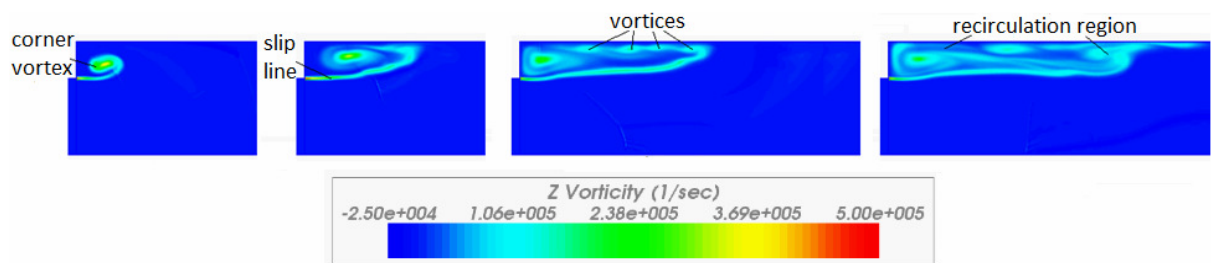
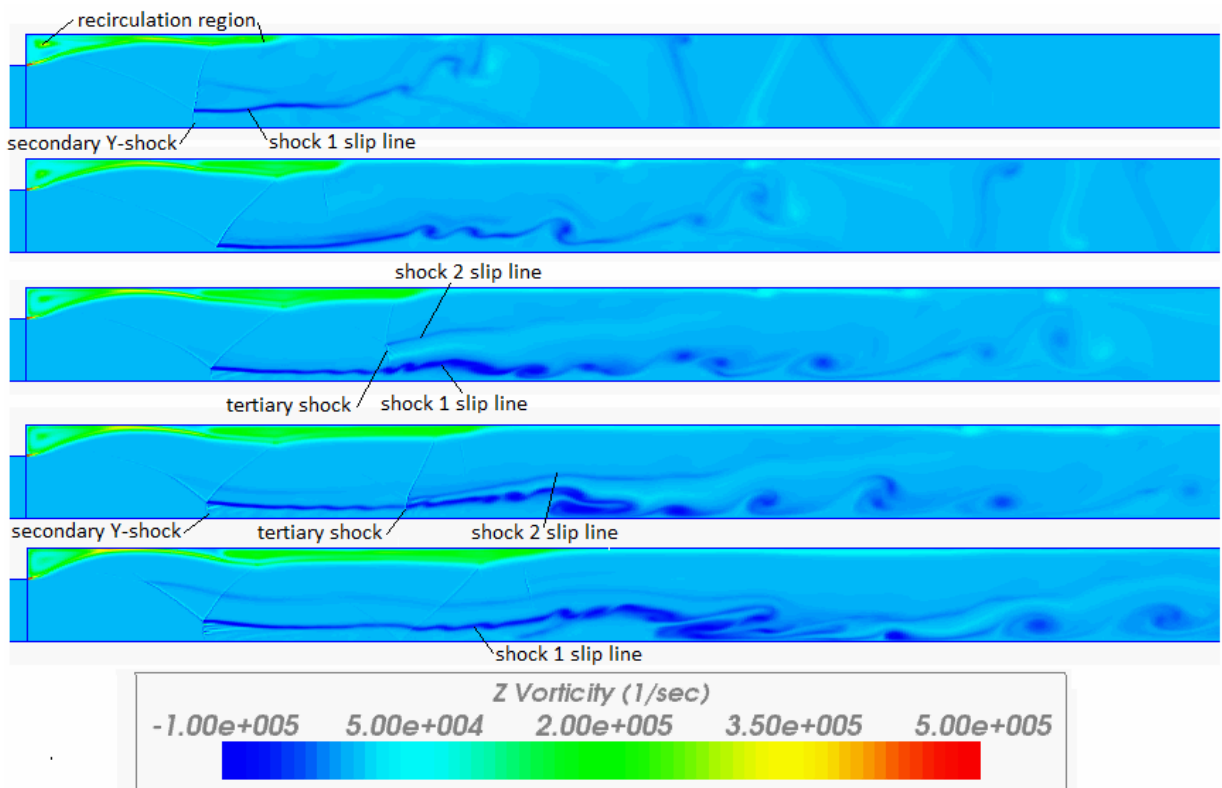**Figure 24. Case (1.30, 1.5)**

Figure 25. Case (1.55, 1.5)

Figure 26. Case (1.93, 1.5)

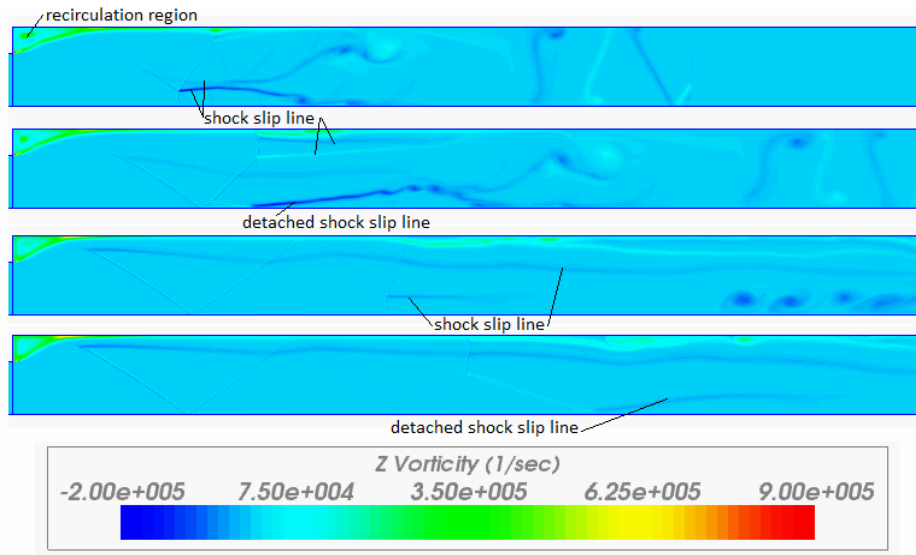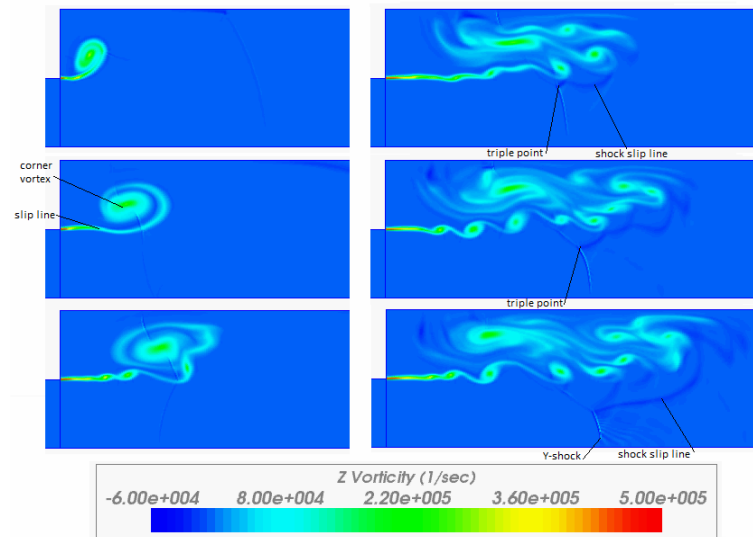**Figure 27. Case (2.50, 1.5)**

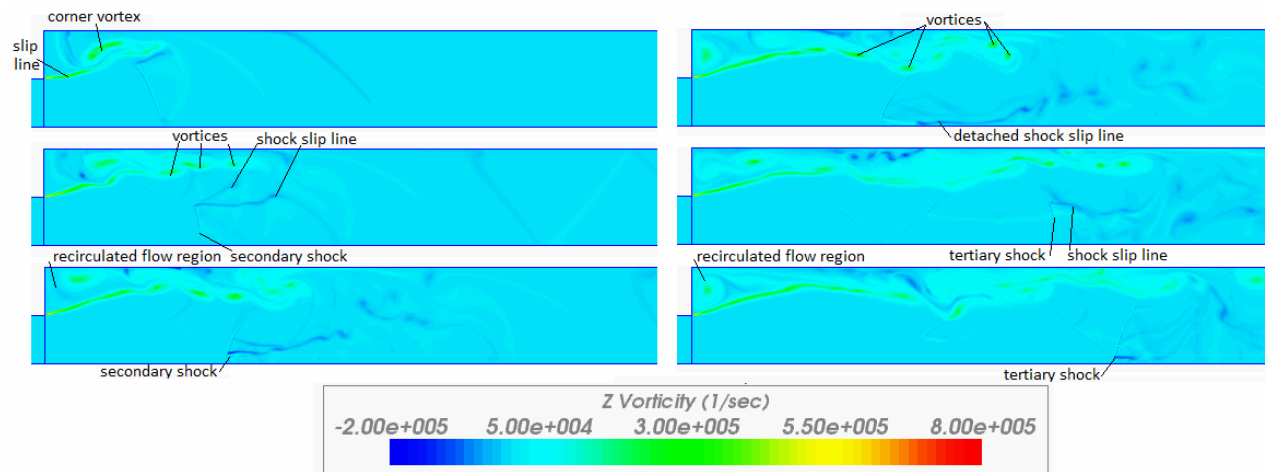
Figure 28. Case (1.50, 2.0)
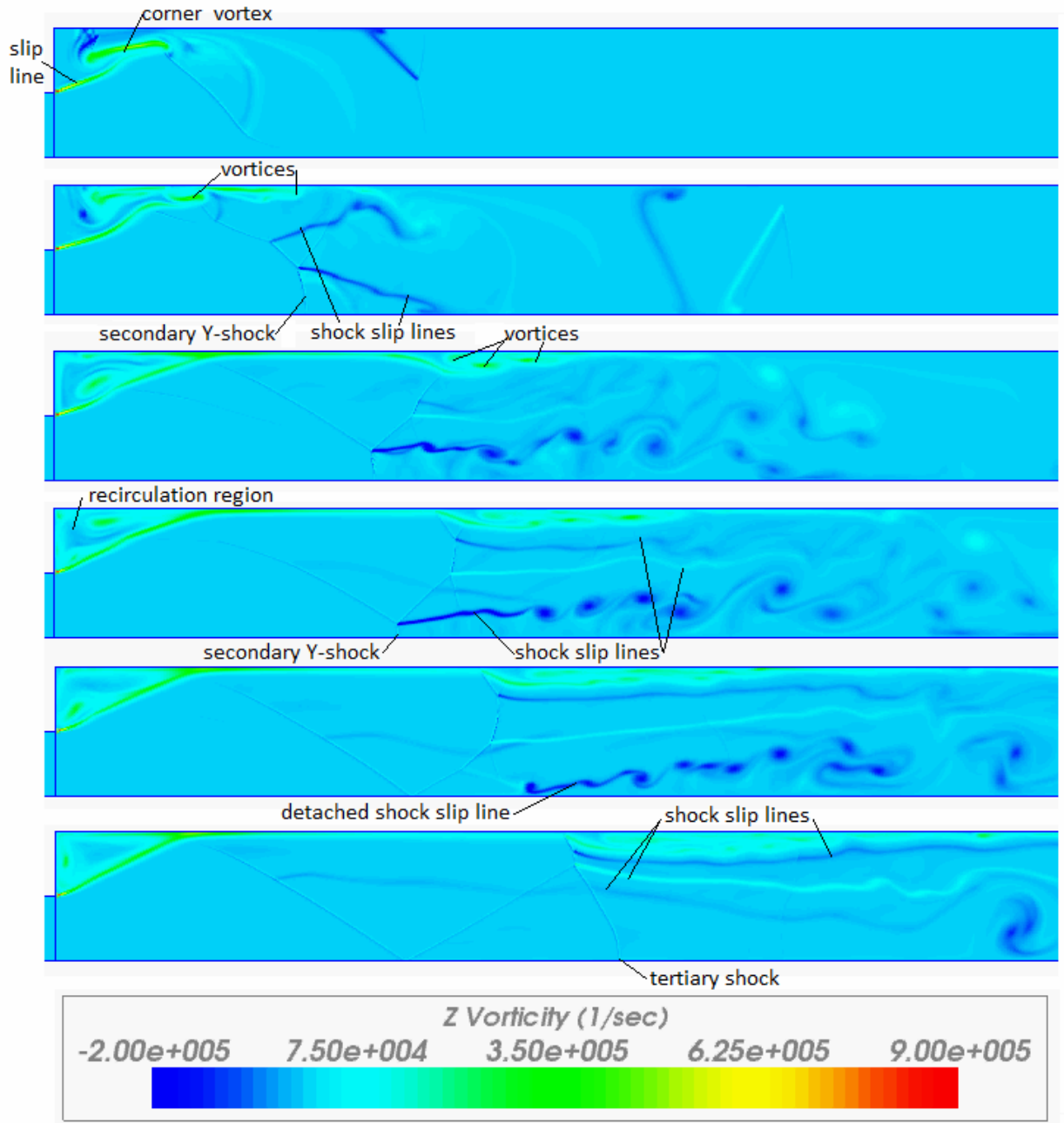

Figure 29. Case (1.85, 2.0)

Figure 30. Case (2.50, 2.0)

V. Quantitative Results and Discussion

First the theoretical results will be discussed quantitatively in terms of the three primary wave strengths. Then, these will be compared to the appropriate numerical results. Finally, some key paramters from the literature will be computed and discussed, such as the critical shock location and the decay profile of the transmitted shock wave.

A. Theoretical

The main results from the theoretical analyses are the primary wave strengths: transmitted shock, reflected expansion, and secondary shock. The transmitted shock is the shock that propagates from the injector duct into the main engine duct, so predicting its strength is relevant to the application. The same holds true for the secondary shock. Figs. 31-33 below show how these wave strengths are functions of incident shock strength and area ratio for the given parameter space.
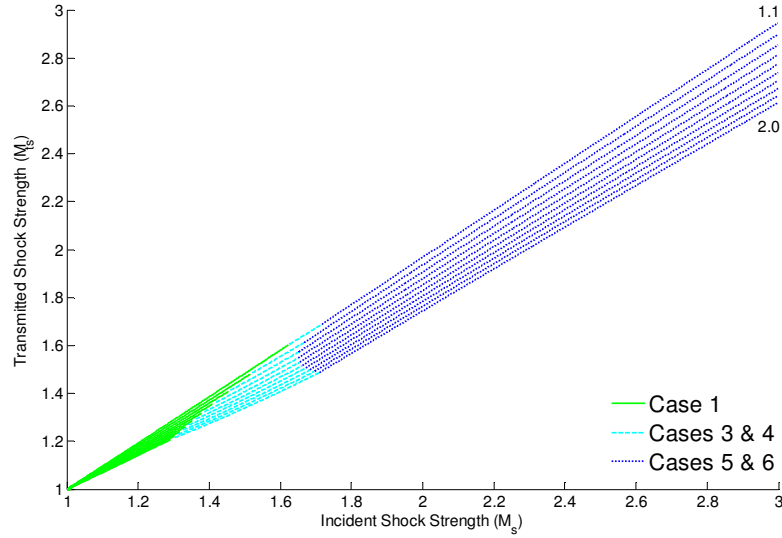
Figure 31. Transmitted Shock Strength as $f(M_S, A_2/A_1)$.

For the smallest area ratio, the transmitted shock strength is linearly proportional to the incident shock strength and strengths (magnitudes) of the two waves are very close. As expected, as the area ratio increases, the transmitted shock strength falls further and further from the corresponding incident shock strength. The transmitted shock strength for cases 1, 5, and 6 are linear, connected smoothly by the case 3 and 4 curves. The curvature of cases 3 and 4 becomes more "full" as the area ratio increases. Note that the shape of the curves separating these cases is remarkably similar to curves a) and b) in Fig. 4a.
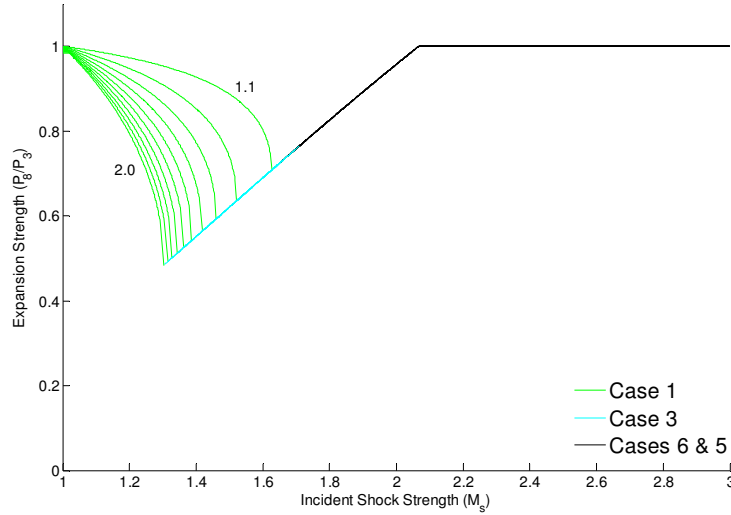

Figure 32. Reflected Expansion Strength as $f(M_S, A_2/A_1)$.

The strength of the reflected expansion exhibits a rather unique behavior. For case 1 values of M_S, the reflected expansion grows in strength nonlinearly. Notice that the case 1 curves tend to move closer together as the area ratio increases. Thus suggests that a theoretical limit might be reached as the area ratio goes to infinity. As the case 1 values asymptote to the case 2 value, they intersect the diagonal line, which is cases 3 and 6. For cases 3 and 6, the strength of the reflected expansion decreases with increasing incident shock strength. This is because the difference in flow velocity (u) behind the incident shock and the sonic velocity at the "throat" (area change) is shrinking, which means a weaker expansion is needed to accelerate the flow. *Notice how the reflected expansion strength for cases 3 and 6 is independent of the area ratio*. This interesting result will be verified later when compared with the simulation results. The horizontal line for $M_S > 2.068$ simply means that the reflected expansion does not exist since the flow velocity is supersonic.
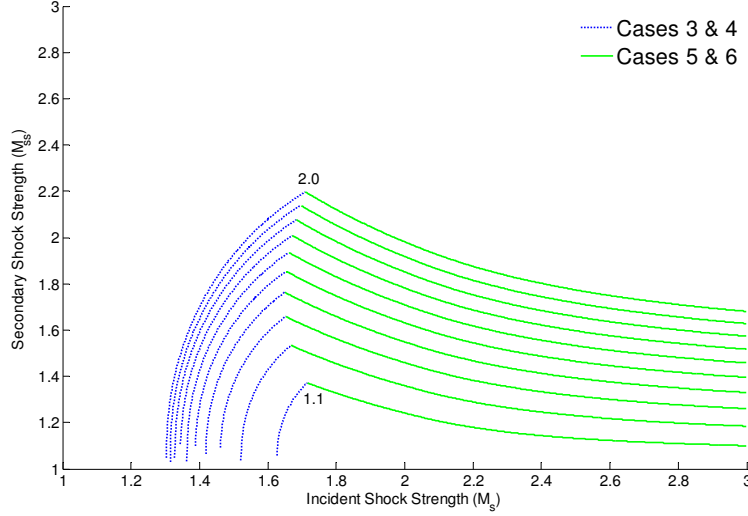
Figure 33. Secondary Shock Strength as $f(M_S, A_2/A_1)$.

The left-facing secondary shock only exists for cases 3-6, where it is stationary for cases 3 and 4, and pushed downstream for cases 5 and 6. Its purpose is to compress the expanded flow leaving the area change to the post-transmitted-shock conditions. For cases 3 & 4, its strength increases with increasing M_S due to the higher amount of energy in the flow. Notice that is possible for the secondary shock to be stronger than the incident shock for the larger area ratios. For cases 5 & 6, its strength decreases with increasing M_S.

B. Comparison to Theory

The primary wave strengths can be extracted from the simulations with some finesse, and they are compared to the appropriate theoretical results. In general, the transmitted shock and the reflected expansion exhibit pretty good agreement with the theory, but the results differ dramatically concerning the secondary shock wave. This, as will be shown later, is due to the multidimensional nature of these flows.
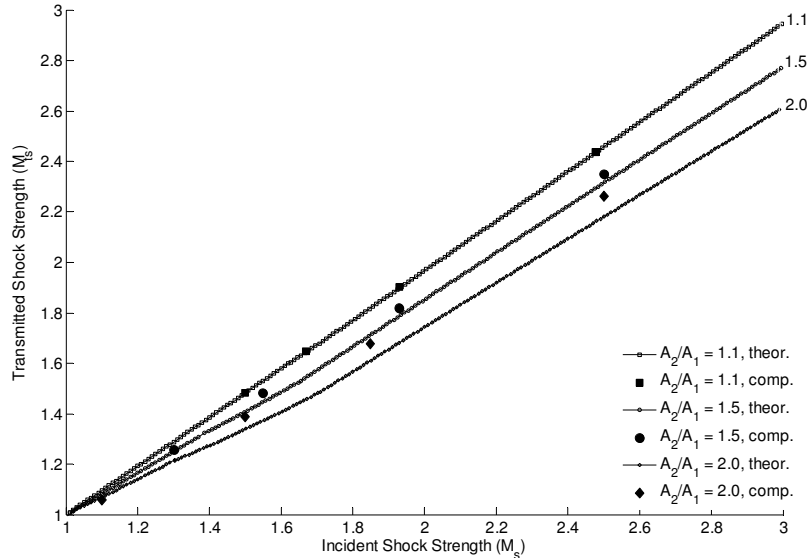
Figure 34. Transmitted Shock Strength – Comparison of Numerical and Theoretical Results

First consider the strength of the transmitted shock. The computational results (12 total) for the transmitted shock strength were obtained in the following manner: The data was sampled along the bottom wall at every 12th time step. The bottom wall was chosen because this would be the "axis of symmetry" in a symmetric geometry (for the purpose of comparison to the literature). At each time step for a given case, the location of the transmitted shock

was found, as determined by the sharp rise in pressure. The transmitted shock strength was calculated from the pressure ratio across it. These two values were recorded for each time step, and a plot of shock pressure ratio (P_6/P_1) versus position along the large duct was made. From this plot, an average of the transmitted shock strength values was computed for each case. These are the values shown in Fig. 34.

As expected, the data for the $A_2/A_1 = 1.1$ case exhibit very good agreement with the theoretical results, because this case is only a small perturbation on the theory (this was the primary reason for choosing this small area ratio). As the area ratio increases, the transmitted shock strength diverges further from the theory. The interesting feature is that the computational values for the two larger area ratios are larger than their theoretical counterparts. Usually, the "actual" values fall below the "theoretical" values. Nonetheless, this finding is consistent with the observation that the flow tended to "overexpand" through the area change, resulting in higher strength compression waves that travelled downstream to merge with the transmitted shock, which resulted in a higher average transmitted shock strength.

Consider case (1.93, 1.1) as a representative to further explain this "finding". Fig. 35 is an instantaneous snapshot of the static pressure along the bottom wall over the domain. The speed of the transmitted shock and the profile through the reflected expansion are predicted quite well, but most of the discrepancy between the theoretical and computational values centers around the secondary shock, which will be discussed in depth in a later section. After passing through the reflected expansion, the flow further supersonically expands through the area change. Note that the theory predicts an expansion to point a in Fig. 35, and the simulations show that the flow actually supersonically expands to point b, where $b < a$. Thus, the flow "overexpands" through the area change.

Second, let us examine the strength of the reflected expansion. The computational data (9 total) was relatively hard to acquire due to both spatial and temporal restrictions. The time stamp chosen to extract the data from reflects an educated choice based on a combination of factors:

a) Must wait until the reflected expansion is fully formed
b) Must wait until the majority of the oscillations present in the bounding flow regions had reduced to small amplitudes
c) Must ensure that the entirety of the reflected expansion was still inside the domain (head and tail) for proper measurement and extraction of data

The spatial restrictions depended on the case. For all case 1 scenarios, the reflected expansion was bounded on both sides by regions of "uniform flow": on the left by the flow shocked by the incident shock (region 3) and on the right by the flow after its tail (region 8). Then an average of the pressure in both regions was computed, and these two values determined the strength of the reflected expansion. For all case 3 and 6 scenarios, the average pressure in region 3 (on the left) was computed to give the high pressure value. Since the tail of the expansion (for these cases) is caught at the area change section (x = 0.1 m), the pressure at this point was used as the low pressure value. The ratio of the two then provided the strength of the reflected expansion for these cases.
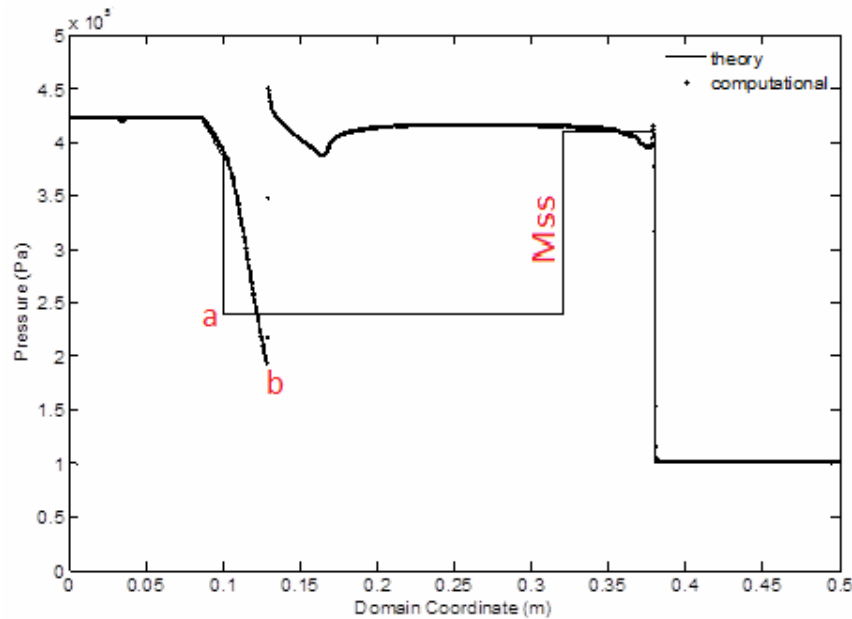

Figure 35. Instantaneous Pressure Trace for Case (1.93, 1.1) at *t = 0.0004992 sec*

27

The computational results show rather good agreement with the theoretical results, as shown in Fig. 36. The strength of the reflected expansion first increases then decreases in strength as the incident shock strength increases. They validate the conclusion that for cases 3 and 6, the strength of the reflected expansion is independent of the area ratio.

Third, the secondary shock strength is the largest difference between the theoretical predictions and the computational results. Recall that the secondary shock only exists for cases 3-6 (case 4 does not exist for the area ratios under consideration here), where case 3 has a standing shock and cases 5 and 6 have moving secondary shocks. The data (9 total) was taken along the bottom wall at the end of each simulation. This was done to allow oscillations to dampen out and all primary flow features to establish their "constant" speeds and strengths.

Theoretically, the case 3 algorithm assumes a "continuous" area change accomplished via a short nozzle and that the secondary shock stands somewhere in the area change section. Furthermore, the flow partially expands before and after the secondary shock. Realistically, in a discontinuous area change, this means that the secondary shock will stand somewhere just downstream of the area change. But the flow still partially expands before and partially expands after the secondary shock. This makes extracting its strength quite diffucult without a large degree of error. The computational data was taken across the shock *only*, meaning that the pressures at points on either side of the numerical shock were used in the calculation of its strength.

For cases 5 and 6, the measurement is made difficult by the fact that the flow usually involves more than one shock to accomplish the compression process, the oblique nature of the shocks, the presence of Mach stems and shock trains, and other 2D phenomena (discussed above). Thus, the only way to extract a measurement is to return to the purpose of the secondary shock: to shock the supersonically expanded flow from the area change to the pressure behind the transmitted shock. The low pressure value was taken from the supersonically expanding flow just to the left of the secondary shock. This point is the "left boundary" of the flow entering the "secondary shock". The high pressure value was computed as an average of the flow pressure between the transmitted shock (having already left the domain) and the last shock in the train (regions 6 and 7 from theory). This flow region is the "right boundary" of the flow leaving the "secondary shock". From the ratio of these two values, the Mach Number of the secondary shock is computed. The results are summarized in Fig. 37.
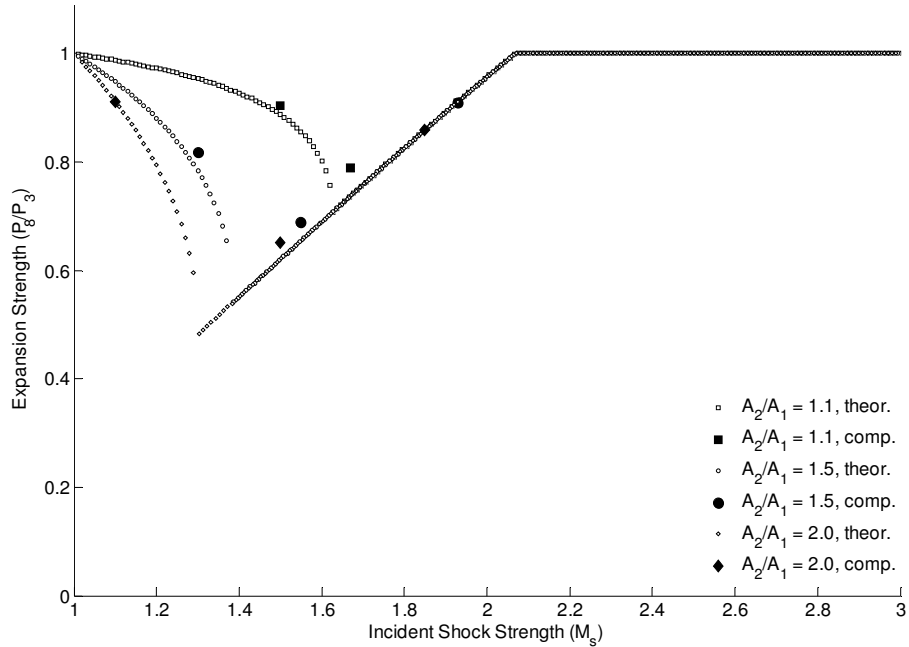
Figure 36. Reflected Expansion Strength: *Comparison of Numerical and Theoretical Results*

Due to the methods used to calculate M_{SS}, the results are not unexpected. The results for case 3 are lower than their theoretical values because only the numerical shock was measured. The results for cases 5 and 6 are far larger than their theoretical values due to a combination of factors: First, because the flow overexpanded through the area change, the first oblique shock in the train was of much higher strength than predicted. Hence the "low pressure" boundary was lower than expected. Second, the pressure behind the transmitted shock was higher than predicted, which means that the "high pressure" boundary was higher than expected.

Looking at Fig. 37, even though the magnitudes of the results differ greatly, the trends are mostly present. That is, the computational data first increase then decrease with increasing M_S. This holds except for the (2.50, 2.0) case, which does not decrease. This is due to the fact that the flow expanded too low before the first oblique shock in the train.

Generally speaking, the secondary shock tended to be of much higher strength and yet of much slower speed than the theory predicted. This is counterintuitive but can be explained via the multidimensionality. The flow essentially traded a single, fast-moving normal shock for a (more-or-less) stationary oblique shock train. [NEED TO FINISH THIS DISCUSSION OF RESULTS]
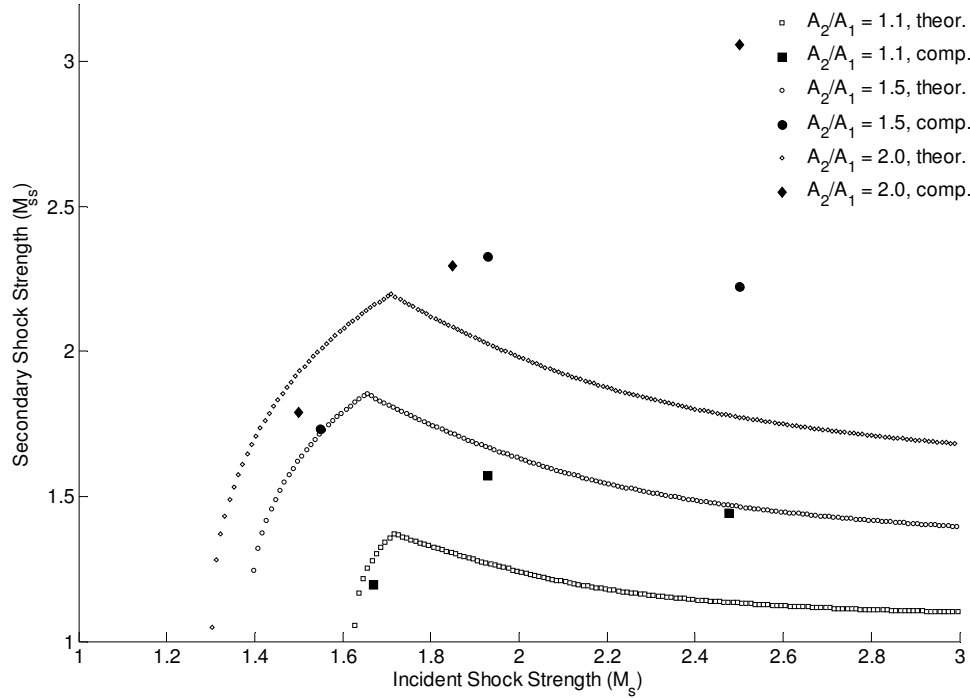

Figure 37. Secondary Shock Strength: *Comparison of Numerical and Theoretical Results*

C. Identified Key Parameters

This section considers parameters that have been identified by previous work to be important measures of these flows. Data on these parameters is extracted from the current simulations to increase the body of work on these topics. The two parameters analyzed here are the location of the critical shock and the decay of the transmitted (axial) shock wave.

Critical Shock Location:

Sloan and Nettleton 1975 did a theoretical and experimental study on 2 DOF (planar) and 3 DOF (cylindrical) shocks entering a sudden area change. Most importantly, their results are for symmetrically expanding shock waves. They establish the definition of the critical shock: "the critical shock is defined as the configuration when the decaying shock wave at the axis [of symmetry] first becomes curved." This is equivalent to the point at which an originally planar shock becomes a spherically expanding shock. If the current geometry is mirrored about the bottom wall, one finds that the two studies have comparable geometries. Hence, the "axis of symmetry" is the bottom wall in these studies, and thus the data was taken along it (from the short simulations) only at every 12th time step. An important note for the data in this section and the next is that taking the data along the bottom wall only records every other oscillation of the OSW.

The location of the critical shock is defined as the distance (in meters) downstream of the area change (here, located at 0.1m from the left end of the domain) at which the decaying shock wave (the transmitted shock wave) first becomes curved. The curvature will be noted by a decrease in the strength of the shock wave as indicated by the ratio between the post-shock pressure and the initial pressure. These two definitions allowed for the location of the critical shock to be determined.

At every 12th time step, the location of the transmitted shock was found via the peak pressure behind the transmitted shock. The location and magnitude (strength) of this peak were recorded for each time step, and these values were plotted over the domain. The first portion of this plot (plateau and decay) was used for these calculations. An average value for the post-shock pressure (the "plateau") was computed, and a 5th order polynomial was curve-fit to the "decay" portion. The x-coordinate of the intersection of these two lines is the critical shock location. This method is similar to the method used in Sloan and Nettles 1975: they used the intersection between the two linear curve fits to determine the critical shock location. An example of the current methodology is presented in Fig. 38. Using the stated methods, the data from the original set of 12 simulations (taken along the bottom wall) produced the results in Fig 39.

There are a few noticeable trends: the critical shock location moves further downstream as the area ratio increases, and that it seems to first decrease then increase with M_S. The current understanding of the transmitted shock decay is that rays (single rarefaction waves) originate at a point and propagate towards the moving shock, and upon contact, curve it. Using the hypothesis that the decay is due to interactions with an expansion, one can provide justification to these trends.

Decay Profile of the Transmitted Shock:

The second key parameter is the decay profile of the transmitted shock. This parameter describes how the transmitted shock decays as it passes through the area change. Recall that this is the shock wave that will enter the main engine duct and propagate downstream, so understanding its behavior is of practical importance. These results will be presented in two parts: First, the initial decay of the transmitted shock will be compared to the literature. Then it will be shown that the transmitted shock undergoes a series of boosts to its strength until its final strength is reached. This final strength is higher than that seen when only considering the shock decay. The authors have not observed this phenomenon documented in the literature.

First consider the initial decay profile of the transmitted shock as it moves downstream. As seen before in the critical shock location results, there are two parts to this curve: the initial plateau as the shock propagates through the area change (without diffracting at the axis), and the subsequent decay as the shock curves and the flow behind it expands. Nettleton 1973 and Sloan and Nettleton 1975 discuss the decay of the "axial shock". Nettleton 1973 examined a "gradual" (continuous) area change over a range of divergent angles of 5° to 90°, and found that the results for the 90° angle diverged significantly from the theoretical results, as well as that a curved corner did not significantly affect the strength of the transmitted shock. Sloan and Nettleton 1975 examined a discontinuous symmetric 90° area change for both planar (2 DOF) and cylindrical (3 DOF) incident shocks. Their results are presented below for comparison.

In order to examine the initial decay profile, the data was taken along the bottom wall for each case at every 12th time step (recall, this records every other oscillation of the OSW). All four long cases (5000 time steps) were used in place of their short counterparts (2500 time steps) to enhance the quality of the data. The data was taken from the area change (at x = 0.1m) to the first compression wave that interacted with the transmitted shock.

Now consider the results over the entire simulation time, instead of just the first portions. After the transmitted shock undergoes the initial decay due to the area change, it experiences a series of subsequent boosts to its strength. This process takes place as a series of initial compression waves followed by expansions. This lends further credence to the hypothesis that the semi-circular expansion and OSW bounce between the upper and lower duct walls, interacting with each other to create alternating regions of lower and higher pressure flow. To visualize this, see Fig. 44. Each jump is due to a right-running oblique compression wave or oblique shock merging with the transmitted shock. Each decay is due to the two-dimensional pieces of the semi-circular expansion. As the gradients across the OSW grow, the compression waves steepen into shock waves. Over time, as the OSW and SCE lose strength, so do the compressions and expansions sent upstream and downstream. Thus, each subsequent jump and decay have smaller amplitudes than the previous set, until eventually the pressure magnitude settles out to a roughly constant value. This behavior is very similar to an overdamped system. This is the value used to calculate the transmitted shock strength to compare to the theoretical results. It be noted, however, that in most cases, a sufficiently long enough time was not reached to obtain this constant value.
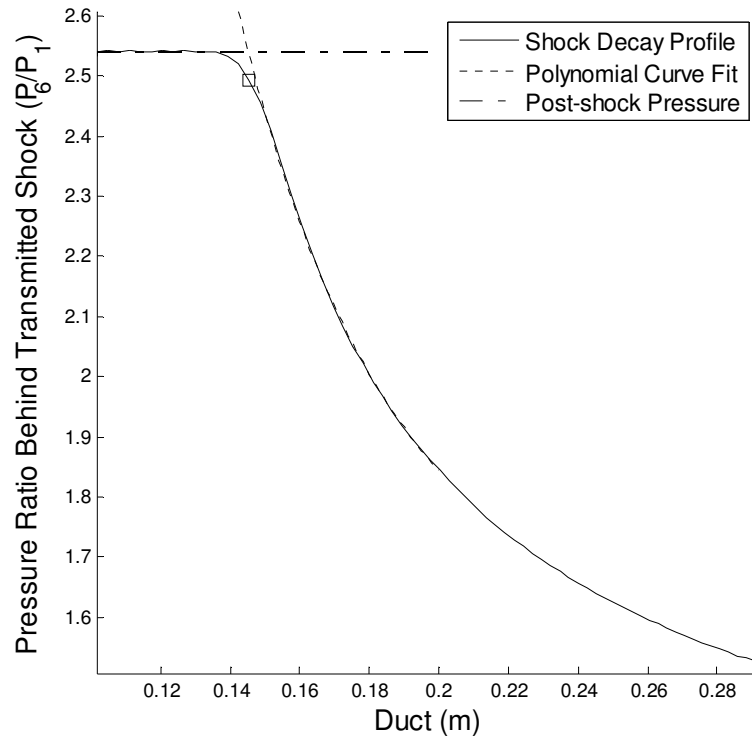
Figure 38. Transmitted shock strength for Case $A_2/A_1 = 2.0$ and $M_S = 1.50$
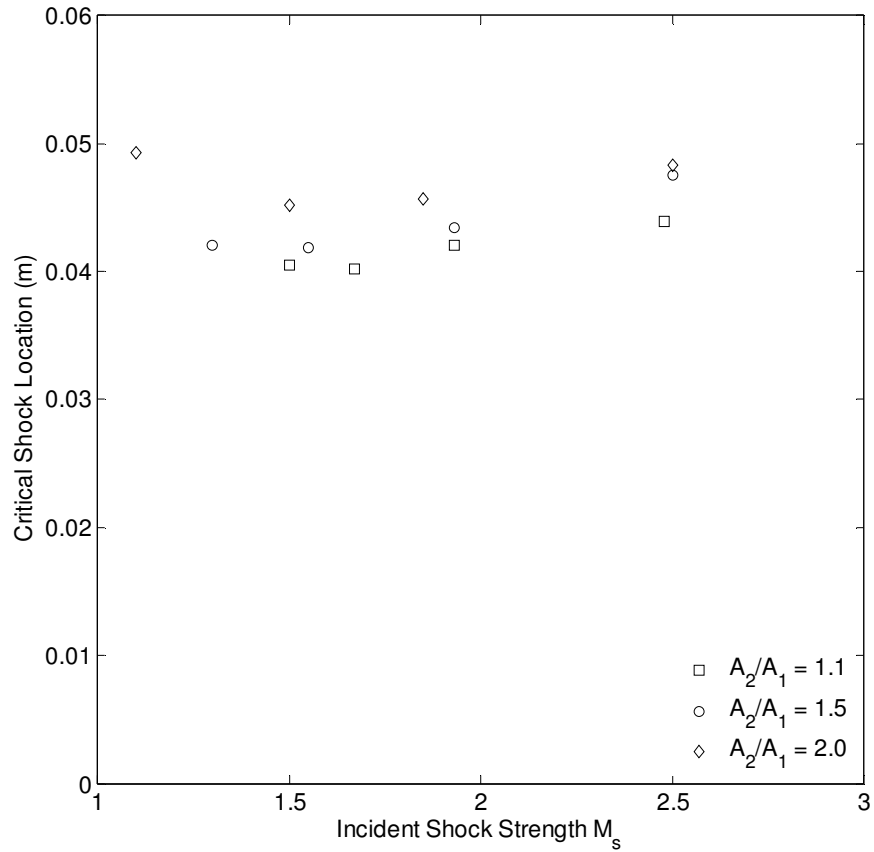

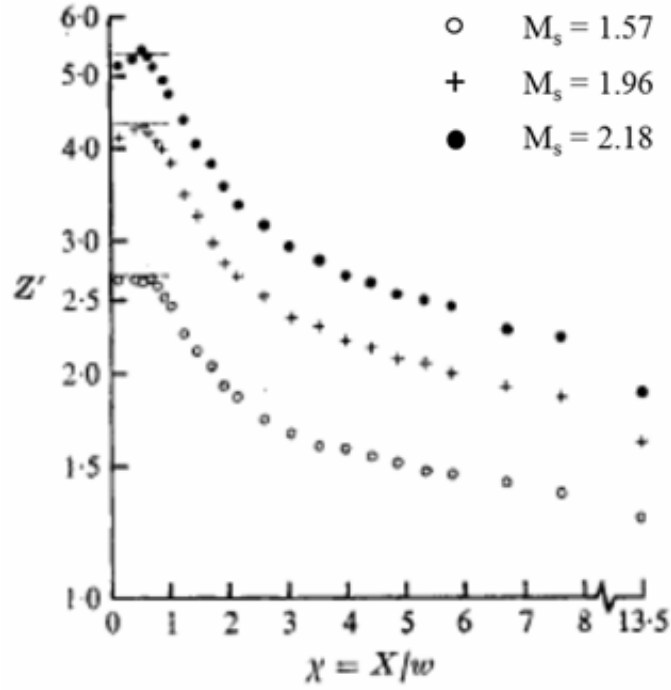**Figure 39. Critical Shock Location as f (M_S, A_2/A_1)**

Figure 40. Axial Shock Strength of Expanding Incident Shocks. *2 DOF (Sloan and Nettleton 1975)*
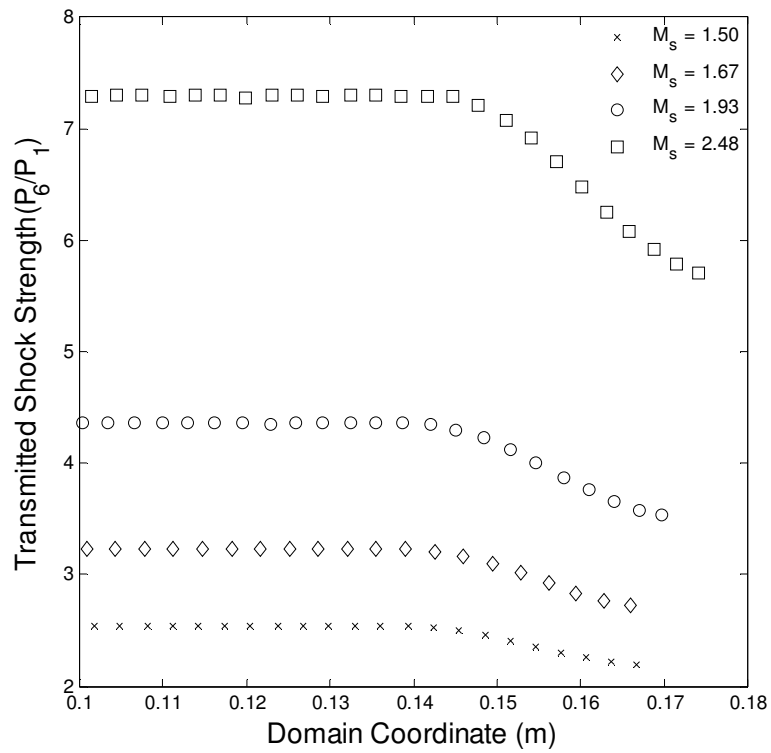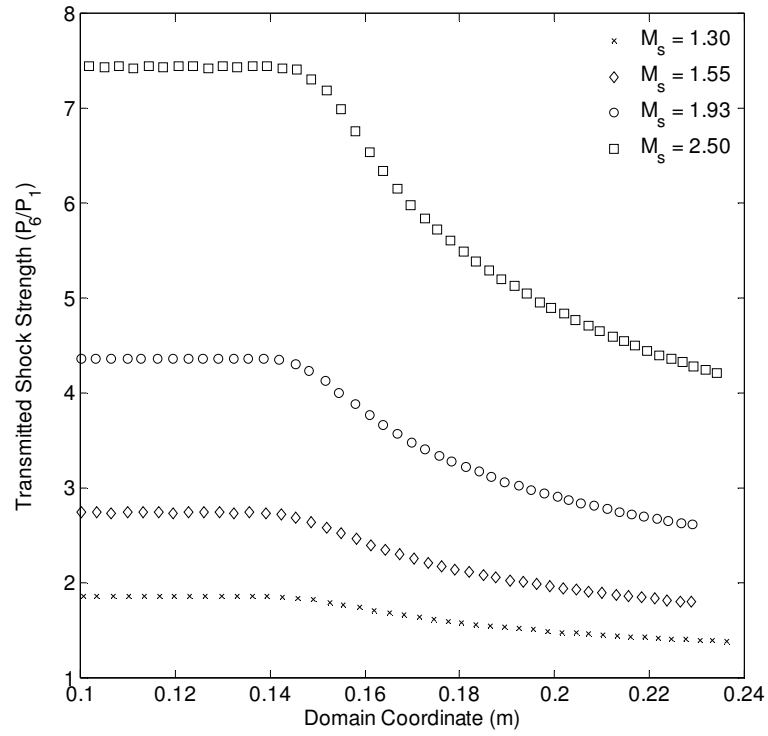

Figure 41. Transmitted Shock Decay for A$_2$/A$_1$ = 1.1

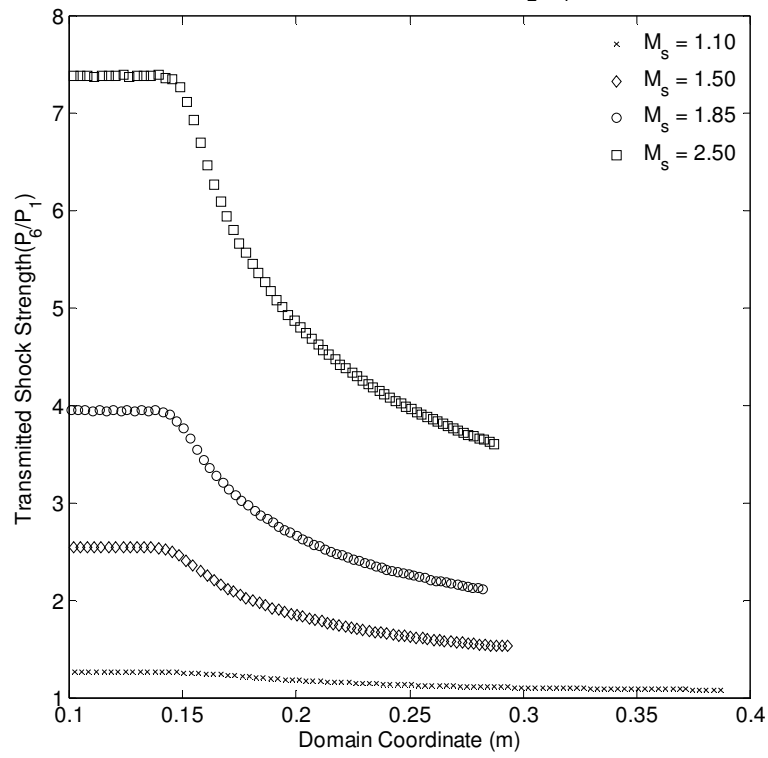**Figure 42. Transmitted Shock Decay for $A_2/A_1 = 1.5$**

Figure 43. Transmitted Shock Decay for $A_2/A_1 = 2.0$

a)   **b)**   **c)**

Figure 44. Transmitted Shock Decay Profile over Domain. *a) (2.48, 1.1) b) (2.50, 1.5) c) (2.50, 2.0)*

VI.   Conclusion

In summary, this study analyzed the interaction between a shock wave and a discontinuous area enlargement using theoretical and numerical techniques. For the given parameter space (M_S, A_2/A_1), there are 6 possible wave patterns primarily involving a transmitted shock wave, an expansion reflected from the interaction, and a secondary shock wave. The 1-D theory provided a framework to analyze the numerical simulations. The primary wave strengths are computed both theoretically and numerically, and these results are compared. In addition, the simulations provided insight into the two-dimensional nature of these flows via pressure and vorticity scalar maps that revealed interesting features such as shock structure, shock-vortex interactions, vorticies, and expansions.

Some conclusions that can be drawn from this study are: First, the theory predicts the transmitted shock and reflected expansion strengths rather well, but fails to predict the secondary shock strength. Second, the transmitted shock wave does not just decay as the literature suggests, but also experiences modifications that serve to increase its strength until a final (higher) strength is reached. This final strength is comparable to the theoretical values. Third, that geometries with discontinuous area changes cannot be accurately modeled by quasi-1D methods due to the highly two-dimensional nature of these flows.

This parametric study contributed the following findings to the scientific knowledgebase: First, the presence of the oscillating shock wave (OSW), its behavior, and how it affects the shock structure. Second, the prescence of the semi-circular expansion and its role as the origin of the reflected expansion. Third, how the multidimensional interaction between these two features creates the prominent flow features present in these flows. Fourth, a new definition of the time to reach quasi-1D flow is offered, based on the behavior of the oscillating shock wave. Finally, a vorticity layer containing vortices that pushed downstream was discovered. This vorticity layer can provide a fluid-dynamic pathway for lower pressure flow to encroach into higher pressure flow, which could be important to the application by providing a means for flow induction into the engine.

Further research is needed to determine under what conditions the following occur: when the reflected shock will not destroy the corner vortex, when the slip lines generated by the triple points in the shock structures are inviscidly stable, and when the corner will begin emitting vortices. The results could lead to some interesting applications of active flow control.

Appendix

As mentioned above, a summary of the numerical settings used for the 16 simulations is presented here:

Table 2. Reference Conditions

Quantity	Value
T_{REF}	*300 K*
P_{REF}	*101325 Pa*
V_{REF}	*347.128 m/s*
L_{REF}	*0.5 m / *0.7 m*

Table 3. Numerical Settings (* denotes a long case)

A_2/A_1	M_S	Case	Run time	Time step	Total # grid pts
1.1	1.50	1	06 hr 15 min	5e-07 sec	152,274
1.1	1.67	3	06 hr 21 min	5e-07 sec	152,274
1.1	1.93	6	06 hr 36 min	4e-07 sec	152,274
1.1	2.48	5	06 hr 19 min	3e-07 sec	152,274
1.5	1.30	1	08 hr 41 min	6e-07 sec	197,596
1.5	1.55	3	09 hr 02 min	5e-07 sec	197,596
1.5	1.93	6	09 hr 25 min	4e-07 sec	197,596
*1.5	1.93	6	16 hr 34 min	4e-07 sec	282,178
1.5	2.50	5	09 hr 04 min	3e-07 sec	197,596
*1.5	2.50	5	16 hr 49 min	3e-07 sec	282,178
2.0	1.10	1	09 hr 42 min	7e-07 sec	253,582
2.0	1.50	3	10 hr 30 min	5e-07 sec	253,582
2.0	1.85	6	10 hr 47 min	4e-07 sec	253,582
*2.0	1.85	6	21 hr 29 min	4e-07 sec	366,136
2.0	2.50	5	10 hr 24 min	3e-07 sec	253,582
*2.0	2.50	5	21 hr 57 min	3e-07 sec	366,136

References

CURVING/TURNING DUCTS:

[1]Igra, O., Falcovitz, J., Meguro, T., Takayama, K., and Heilig, W. (1999) Shock Wave Propagation through a double bend duct. Proc. Of the 22nd Int. Symposium of Shock Waves, Imperial College, London.

[2]Liang, S. M., Weng, K. C., and Takayama, K. Numerical Study of Blast-wave propagation in a double-bent duct. AIAA vol 40 no 9 2002.

[3]Edwards, D. H., Fearnley, P., and Nettleton, M. A. Shock Diffraction in channels with 90° bends. J. Fluid Mech. (1983) vol 132, pg. 257-270.

[4]Takayama, K., Honda, M., Onodera, O. Shock Propagation along 90 degree bends. Instn. High Speed Mech. Report 1976 vol 35 pg. 83-111

[5]Sommerfeld, M., Nishida, M., and Takayama, K. (1985) Shock propagation in a curved duct. Instn. High Speed Mech. Report, Tohoku University, Sendai, Japan.

[6]Kage, K., Shiroyama, M., and Ishimatsu, K. Numerical study of shock waves propagating through right angled multiple elbows. J. Thermal Science, vol 14 no 3

LARGE ANGLES/CORNERS:

[7]Skews, B. W. The Perturbed Region behind a diffracting shock wave. J. Fluid Mech (1967), vol. 29 part 4, pgs. 705-719.

[8]Skews, B. W. The Shape of a Diffracting Shock Wave. J. Fluid Mech. (1967) vol. 29 part 2, pgs. 297-304.

[9]Sun, M. and Takayama, K. Vorticity Production in Shock Diffraction. J. Fluid Mech. (2003) vol 478, pgs. 237-256.

[10]Bazhenova, T. V., Gvozdeva, L. G., and Zhilin, Yu. V. Change in the Shape of the Diffracting Shock Wave at a Convex Corner. Acta Astronautica, Vol. 6, pgs. 401-412

[11]Dumitrescu, L. Z. and Preda, S. Some New Results Concerning the Diffraction of a Shock Wave Around a Convex Corner. Modern Developments in Shock Tube Research: Proceedings of the 10th International Shock Tube Symposium 1975, pgs. 369-377. Editor: G. Kamimoto

BRANCHED DUCTS:

[12]Heilig, W. (1975) Propagation of shock waves in various branched ducts. Proc. of the 10th Int. Shock Tube Symposium, Kyoto Japan.

[13]Hammitt, A. G., and Carpenter, H. J. (1964) Unsteady flow past junctures in ducts. AIAA 2, 2224

[14]Igra, O., Wang, L., Falcovitz, J., and Heilig, W. (1998c) Shock Wave propagation in a branched duct. Shock Waves, 8, 375-381.

[15]Deckker, B. E. L., and Male, D. H. Unsteady Flow in a Branched Duct. Proc. Instn Mech. Engrs. 1968 Vol 182 Paper 10

[16]Deckker, B. E. L., and Male, D. H. Fluid Dynamic Aspects of Unsteady Flow in Branched Ducts. Proc. Instn Mech. Engrs. 1968 Vol 182 Paper 18

[17]Zimmerman, A. W., Peterson, J. B., and Carpenter, H. J. Nonsteady flow past duct junctures. AIAA vol 7 no 3

BAFFLES/OBSTACLES:

[18]Reichenbach, H., and Kuhl, A. L. (1993) Shock-induced turbulent flow in baffle systems. Proc. Of 16th Int. Symposium on Shock Tubes and Waves, Aachen, 847-853.

[19]Kuhl, A. L. and Reichenbach, H. Flow visualization of shock propagation in baffle systems. Ernst-Mach-Institute.

[20]Berger, S., Sadot, O., and Ben-Dor, G. Experimental investigation on the shock-wave load attenuation by geometrical means. Shock Waves (2010) 20: 29-40.

[21]Graham, J. M. R. and Hillier, R. Shock wave diffraction at a sharp edge and the effect of baffles in a shock tube. proc. of the 13th Int. Symp. on Shock Tubes and Waves, pg. 402-410

[22]Ohtomo, F., Ohtani, K., and Takayama, K. Attenuation of shock waves propagating over arrayed baffle plates. Shock Waves (2005) Vol 14 no 5-6, pg. 379-390.

[23]Klapovskii, V. E., Mineev, V. N., Grigor'ev, G. S., Vershinin, V. Yu., Logvenov, A. Yu. Attenuation of an air shock wave by perforated baffles. Combustion, Explosion, and Shock Waves, 1983, Volume 19, Number 5, Pages 638-639

[24]Gel'fand, B. E., Medvedev, S. P., Polenov, A. N., Tsyganov, S. A. Interaction of Unsteady pressure waves and perforated baffles. Fluid Dynamics, 1987, Volume 22, Number 6, Pages 969-972

[25]Grin, V. T., Kraiko, A. N., and Miller, L. G. Decay of a shock wave at a perforated baffle. Journal of Applied Mechanics and Technical Physics, 1981, Volume 22, Number 3, Pages 372-378

[26]Schultz-Grunow, F. Production and Inhibition of Mach Stems. Modern Developments in Shock Tube Research: Proceedings of the 10th international Shock Tube Symposium, Kyoto, Japan, 1975. Kamimoto, G. pgs. 356-362

SHOCK WAVE FOCUSING:

[27]Inoue, O., Takahashi, N., and Takayama, K. Shock Wave focusing in a log-spiral duct. AIAA vol 31, no 6 1993

[28]Bond, C., Hill, D. J., Meiron, D. I., and Dimotakis, P. E. Shock focusing in a planar convergent geometry: experiment and simulation. J. Fluid Mech. (2009) vol 641, pg. 297-333

[29]Setchell, R. E., Storm, E., and Sturtevant, B. An investigation of shock strengthening in a conical convergent channel. J. Fluid Mech (1972) vol 56 part 3, pg. 505-522.

[30]Taieb, D., Ribert, G., Hadjadj, A. Numerical Simulations of shock focusing over concave surfaces. AIAA 2010 vol 48 no 8.

[31]Takayama, K. and Jiang, Z. Reflection and focusing of toroidal shock waves from co-axial annular shock tubes. AIAA-1997-523

[32]Cramer, M. S. Focusing of a weak three-dimensional shock wave. AIAA 1981 vol 19 no 10

[33]Milton, B. E. and Archer, R. D. Generation of implosions by area change in a shock tube. AIAA 1969 vol 7 no 4.

[34]Hosseini, S. H. R. and Takayama, K. Experimental study of toroidal shock wave focusing in a compact vertical annular diaphragmless shock tube. Shock Waves (2010) 20:1-7

MISCELLANEOUS:

[35]Ben-Dor, G., Igra, O., and Elperin, T. Handbook of Shock Waves. Academic Press: 2001 Vol 1-3

[36]Chester, W. The propagation of shock waves in a channel of non-uniform width. Quart. J. Mech. Appl. Math., 1953, 6, 440-452

[37]Chester, W. The propagation of shock waves along ducts of varying cross-section. Adv. Appl. Mech. 1960, 6, 119-152

[38]Chisnell, R. F. The motion of a shock wave in a channel, with applications to cylindrical and spherical shock waves. J. Fluid Mech. 1957, 2, 286-298.

[39]Whitham, G. B. A new approach to problems of shock dynamics: Part I Two-dimensional problems. J. Fluid Mech. 1957, 2, 146-171.

[40]Whitham, G. B. On the propagation of shock waves through regions of non-uniform area or flow. J. Fluid Mech. 1958, 4, 337-360.

[41]Whitham, G. B. A new approach to problems of shock dynamics: Part II three-dimensional problems. J. Fluid Mech. 1959, 5, 369-386.

SHOCK WAVES IN ALL OF THE BELOW:

[42]Schardin, H. and Reichenbach, H. The behavior of shock waves in ducts and when entering entrance structures. Proc. Symposium on Protective Structures for Civilian Populations pg. 193-206

[43]Kahane, A., Warren, W. R., Griffith, W. C., and Marino, A. A. A Theoretical and Experimental Study of Finite Amplitude Wave Interactions with Channels of Varying Area. J. Aeron. Sci. 1954 vol 21, no 8.

[44]Andrianov, N. and Warnecke, G. On the Solution to the Riemann Problem for the Compressible Duct Flow. SIAM J. Appl. Mathem, vol 64, no 3, pg. 878-901.

[45]Yu, F. M. and Wang, C. Z. Study on the shock interference in a wedged convergent-divergent channel. Proc. of the 24th Int. Symposium on Shock Waves, Beijing, China. Springer 2004.

[46]Hawken, D. F. and Gottlieb, J. J., Prediction of Two-Dimensional Time-Dependent Gasdynamic Flows for Hypersonic Studies. UTIAS Report No. 335, March 1990

[47]Bazhenova, T. V., Gvozdeva, L. G., and Nettleton, M. A. Unsteady Interactions of Shock Waves. Prog. Aerospace Sci. 1984 Vol. 21 pgs. 249-331.

[48]Oshima, K. Some Flow Patterns Observed in Shock Tubes and the Comparison with Results by Numerical Simulation. Modern Developments in Shock Tube Research: Proceedings of the 10th International Shock Tube Symposium 1975, pgs. 480-487. Editor: G. Kamimoto

BOTH AREA ENLARGEMENTS AND REDUCTIONS (NOZZLE FLOWS):

[49]Amann, H. O., and Reichenbach, H. (1973) Unsteady flow phenomena in shock-tube nozzles. Proc. Of the 9th Int. Shock Tube Symposium, Stanford, CA.

[50]Igra, O., Wang, L., Falcovitz, J., and Amann, H. O. (1998b) Simulation of the starting flow in a wedge-like nozzle. Shock waves, 8, 235-242.

[51]Han, Z. and Yin, X. Shock Dynamics. Beijing Science Press 1993

[52]Rudinger, George. Wave Diagrams for Nonsteady Flow in Ducts. D. Van Nostrand Company: 1955

[53]Needham, C. E. and Crepeau, J. E. SHAMRC, Second-order Hydrodynamic Automatic Mesh Refinement Code. Rep. Applied Research Associates (ARA) Inc., Albuquerque, NM, 1998 Vol. 2, User's Manual.

[54]Falcovitz, J. and Ben-Artzi, M. Recent Developments of the GRP Method. Japan Soc. Mech. Engrs. Internat. J., Series B, Vol. 38, No. 4, 1995, pgs. 497-517.

BOTH CONTINUOUS AREA ENLARGEMENTS AND REDUCTIONS:

[55]Igra, O., Elperin, T., Falcovitz, J., Zmiri, B. Shock Wave Interaction with Area Changes in Ducts. Shock Waves (1994) 3:233-238. (RCM)

[56]Greatrix, D. R. and Gottlieb, J. J., An Analytical and Numerical Study of a Shock Wave Interaction with an Area Change. UTIAS Report No. 268, Nov. 1982

CONTINUOUS AREA ENLARGEMENT:

[57]Igra, O. and Falcovitz, J. Numerical solution to rarefaction or shock wave/duct area-change interaction. AIAA vol 24, no 8

[58]Nettleton, M. A. Shock Attenuation in a 'Gradual' Area Expansion. J. Fluid Mech. (1973), vol 60 part 2, pgs. 209-223.

CONTINUOUS AREA REDUCTIONS:

[59]Igra, O., Wang, L., and Falcovitz, J. (1998a) Nonstationary compressible flow in ducts with varying cross-section. Proc. Instn. Mech. Engrs., 212, 225-243.

[60]Asano, N. Shock waves and non-stationary flow in a duct of varying cross-section. J. Fluid Mech. (1971) vol 46 part 1, pg. 111-128.

[61]Bird, G. A. The effect of wall shape on the degree of reinforcement of a shock wave moving into a converging channel. J. Fluid Mech. Vol 5 part 1 pg. 60-66

[62]Russell, D. A. Shock-wave strengthening by area convergence. J. Fluid Mech. (1967), vol 27 part 2, pgs. 305-314.

[63]Ben-Dor,Gabi. Shock Wave Reflection Phenomena – 2nd Ed. Springer-Verlag 2010.

BOTH DISCONTINUOUS AREA ENLARGEMENTS AND REDUCTIONS:

[64]Menina, R., Saurel, R., Zereg, M., Houas, L. *Modelling Gas Dynamics in 1D Ducts with Abrupt Area Change.* Shock Waves (2011), Volume 21, Number 5, Pages 451-466.

[65]Salas, Manuel. Shock Wave Interaction with an Abrupt Area Change. NASA Technical Report 3113. 1991

DISCONTINUOUS AREA REDUCTIONS:

[66]Falcovitz, J. and Igra, O. Model for shock interaction with sharp area reduction. Proc. of the 26th Int. Symposium on Shock Waves, Vol. 1. Springer. Pg. 647-652.

[67]Rudinger, G. Passage of Shock Waves Through Ducts of Variable Cross Section. Physics of Fluids 1960, Vol 3 no 3. Pg. 449-455.

[68]Itoh, S., Kitamura, A., and Itaya, M. On the Profile of Reflected Shock and its Attenuation Process. Modern Developments in Shock Tube Research: Proceedings of the 10th International Shock Tube Symposium 1975, pgs. 392-399. Editor: G. Kamimoto

[69]Zallen, D. and Truax, P. P. Capture area ratio effect on a propagating shock. AIAA 1972 vol 10, no 3. Pg. 341-343

DISCONTINUOUS AREA ENLARGEMENT (BOTH CIRCULAR AND RECTANGULAR)

[70]Maeno, K., Kaneta, T., Morioka, T., and Honma, H. Pseudo-schlieren CT Measurement of Three-Dimensional Flow Phenomena on Shock Waves and Vortices Discharged from Open Ends. Shock Waves (2005) 14(4): 239-249.

[71]Bazhenova, T. V., Bormotova, T. A., Golub, V. V., Novikov, S. A., Shcherbak, S. B. Flow Expansion Behind a Shock Wave Discharged from a Channel. High Temperature, 2001 Vol. 39 No 1 pgs. 119-123.

[72]Abate, G. and Shyy, W. Dynamic Structure of Confined Shocks Undergoing Sudden Expansion. Progress in Aero. Sci. 38 (2002) 23-42.

[73]Sloan, S. A. and Nettleton, M. A. A Model for the Axial Decay of a Shock Wave in a Large Abrupt Area Change. J. Fluid Mech. (1975), Vol 71 part 4, pg. 769-784.

DISCONTINUOUS CIRCULAR AREA ENLARGEMENTS:

[74]Liang, S. M. and Liao, C. Y. Blast-wave dynamics in a circular duct with a sudden expansion. AIAA vol 45 no 9 2007.

[75]Liang, S. M. and Chen, H. Flow Visulaization of numerically simulated blast waves discharging from open-ended duct. AIAA vol 41 no 12 2003.

[76]Sloan, S. A. and Nettleton, M. A. A Model for the Decay of a Wall Shock in a Large Abrupt Area Change. J. Fluid Mech. (1978) vol 88 part 2, pgs. 259-272.

[77]Chang, K. S. and Kim, J. K. Numerical Investigation of inviscid shock wave dynamics in an expansion tube. Shock Waves (1995) 5:33-45.

[78]Jiang, Z. L., Babinsky, H., Meguro, T., Takayama, K. Numerical Study on Transient Shock Wave Flows in a Tube with a Sudden Change in its Cross Section. AIAA-96-0291.

[79]Jiang, Z., Takayama, K., Babinsky, H., and Meguro, T. Transient Shock Wave Flows in Tubes with a Sudden Change in Cross Section. Shock Waves (1997) 7: 151-162

OPEN ENDS OF SHOCK TUBES:

[80]Kim, H. D., Lee, D. H., Kashimura, H., and Setoguchi, T. Propagation Characteristics of Compression Waves Reflected from the Open End of a Duct. KSME Int. J., 2003 Vol 17 No 5, pgs. 718-725.

[81]Abe, A. and Takayama, K. Numerical Simulation and Density Measurement of a Shock Wave Discharged from the Open End of a Shock Tube. JSME Int. J. 1990 Series II, Vol 33, No 2.

[82]Kashimura, H., Yasunobu, T., Nakayama, H., Setoguchi, T., and Matsuo, K. Discharge of a Shock Wave from an Open End of a Tube. J. Thermal Sci. Vol 9 No 1, pgs. 30-36.

[83]Yasunobu, T., Kuchii, S., Kashimura, H., and Setoguchi, T. Characteristics of Compression Wave Caused by Reflection of Expansion Wave at Open End of Tube. J. of Thermal Sci., 2002 Vol 11 No 2 pgs. 97-103

[84]Brouillette, M., Tardif, J., and Gauthier, E. Experimental Study of Shock-Generated Vortex Rings. Shock Waves at Marseille: Shock structure and kinematics, blast waves, and detonations : proceedings of the 19th International Symposium on Shock Waves, Marseille, France, 1993. Berlin : Springer-Verlag, 1995

DISCONTINUOUS RECTANGULAR AREA ENLARGEMENTS:

[85](duplicate)Igra, O., Falcovitz, J., Meguro, T., Takayama, K., and Heilig, W. (1999) Shock Wave Propagation through a double bend duct. Proc. Of the 22nd Int. Symposium of Shock Waves, Imperial College, London.

[86]Heilig, W. (1993) About the attenuation effect of expansion chambers in channels. Proc. of the 13th Int. Symposium on Military Application of Blast Simulation, the Hague, The Netherlands.

[87]Toro, E.F., Heilig, W., and Jochims, M. Numerical and Experimental Study of Some Shock Wave Phenomena. Shock Waves at Marseille: Shock structure and kinematics, blast waves, and detonations : proceedings of the 19th International Symposium on Shock Waves, Marseille, France, 1993. Berlin : Springer-Verlag, 1995

[88]Igra, O., Falcovitz, J., Reichenbach, H., and Heilig, W. Experimental and numerical study of the interaction between a planar shock wave and a square cavity. J. Fluid Mech. 1996 vol 313, pg. 105-130

[89]Falcovitz, J., Igra, O., Heilig, W., and Reichenbach, H. The Interaction of a Normal Shock Wave with a Square Trench. Shock Waves at Marseille: Shock structure and kinematics, blast waves, and detonations : proceedings of the 19th International Symposium on Shock Waves, Marseille, France, 1993. Berlin : Springer-Verlag, 1995

[90]Igra, O., Wu, X., Falcovitz, J., Meguro, T., Takayama, K., Heilig, W. Experimental and theoretical study of shock wave propagation through double-Bend Ducts. J. Fluid Mech. (2001), vol. 437, pp. 255-282

[91]Abate, G. et al. An experimental and numerical investigation of fast transient gas dynamics. AIAA 2000-0556

[92]Abate, G., Shyy, W., Segal, C., Anderson, C. Gas dynamic Structure of a Shock Wave Undergoing Sudden Expansion. AIAA-98-2508

[93]Abate, G., Shyy, W., Mikolaitis, D., Segal, C., Anderson, C. Gas Dynamic Structure of Expanding Shock Flows. AIAA-99-0820.

[94]Abate, G. L. Experimental Investigations of Shock Waves Undergoing Sudden Expansion in a Confined Chamber. Dissertation 1999, University of Florida.

[95]Jiang, Z., Onodera, O., and Takayama, K. Evolution of shock waves and the primary vortex loop discharged from a square cross-sectional tube. Shock Waves (1999) 9:1-10.

[96]Bazhenova, T. V., Bormotova, T. A., Golub, V. V., Shul'meister, A. M., Shcherbak, C. B. Type of reflection of a near-wall Shock Wave in the Process of Diffraction from a Square Channel. Fluid Dynamics 2000 Vol 35 No 1.

[97]Lee, Y. K., Kweon, Y. H., Kim, H. D., and Setoguchi, T. Three-Dimensional Computations of the Impulsive Wave Discharged from a Duct. J. Mech. Sci. Tech. 2005 Vol 19 No 2 pgs. 605-617.

[98]Deckker, B. E. L. and Gururaja, J. An investigation of shock wave behavior in ducts with a gradual or sudden enlargement in cross-sectional area. Proc. Instn Mech. Engrs. 1969-1970 Paper 4

[99]Anderson, John D. Modern Compressible Flow 3rd Edition. McGraw Hill: 2003 International Edition

[100]Aerosoft, Inc. General Aerodynamic Simulation Program (GASP) Version 5.0 Reference Guide. http://www.aerosft.com

[101]Pointwise, Inc. Pointwise User Manual 2010. http://www.pointwise.com

SHOCK-VORTEX INTERACTIONS:

Liang, S. M., Chung, W. T., Chen, H., Shyu, S. H. Numerical Investigation of reflected shock/vortex interaction near an open-ended duct. AIAA vol 43 no 2 2005.